Radiator modeling and design for MRI safety assessment

by

Shuo Song

A dissertation submitted to the Department of Electrical and Computer Engineering,
Cullen College of Engineering
in partial fulfillment of the requirements for the degree of

Doctor of Philosophy

in Electrical Engineering

Committee Chair: Dr. Ji Chen

Committee Member: Dr. David Jackson

Committee Member: Dr. Jiefu Chen

Committee Member: Dr. Benhaddou Driss

Committee Member: Dr. Wolfgang Kainz

University of Houston

May 2021

ACKNOWLEDGMENTS

I would like to give my special appreciation to my advisor Dr. Ji Chen who has been generously providing help and supervision to my research. As a bachelor-to-PhD student I was lost in the many choices of research area of interest when I first came to the USA, without the support of guidance of Dr. Ji Chen I would not even know 'MRI safety', and finally it turns out I like this area and I would like to continue the research in the future.

I would also like to show my sincere appreciation to the other committee members. Dr. David Jackson, from the same department of ECE, is always willing to help when I meet troubles in the theoretical EM analysis; and Dr. Jiefu Chen, on his class I got to know the idea of using machine learning to solve complicate EM problems and he offered help on my first project using such an idea. Dr. Driss Benhaddou, although we are from different apartments, his suggestions from another aspect of view really helped to notice some problems that always ignored by us. And Dr. Wolfgang Kainz, as a researcher from FDA, he helped me to properly following the standard and solved many detailed problems.

At the end of the acknowledgments, I would also like to thank my friends with great gratification, Dr. Jianfeng Zheng, Dr. Ran Guo, Dr. Qi Zeng, Dr. Jinshen Liu, Dr. Rui Yang, Dr. Dagang Wu, Mr. Yu Wang, Mr. Qianlong Lan, Mr. Wei Hu, Mr. Jiajun, Ms. Meiqi Xia, and my family member, without your cooperation and company, I would not finish the long PhD program with so much pleasure and happiness.

ABSTRACT

Magnetic resonance imaging (MRI) has become a widely used diagnostic method due to its unparalleled ability for soft tissue imagine. Although 1.5T MRI is still the most performed procedure in clinic, higher fields such as 3 T and 7 T are gaining more popularity because of their increased sensitivity and spatial resolution. However, the increased frequency caused the degradation of the field uniformity. To compensate the field distortion, a so-called RF shimming method is proposed.

The tricky part of RF-shimming is that once the arbitrary excitation is applied, the induced special absorption rate (SAR) will be hard to predict, the most dangerous point, which has the highest SAR, will move around the whole-body area and SAR level will change quiet a lot, in Chapter 1, we studied the SAR and temperature level in different human bodies, under different exposure conditions; in Chapter 2, we applied the machine learning method to help us to predict the induced SAR location and level.

And nowadays, there are increasing populations who has implantable medical devices (IMDs) who need to go under MRI scanning, especially for some patients, the treatment will need IMDs and MRI together, to investigate the interaction of the IMDs and the EM field, we designed a new test system, the design, the validation of the novel field generator and its application for passive IMDS is introduced in Chapter 3, the application on active IMDs, which has quite different methods, is included in Chapter 4.

Table of Contents

LIST OF TABLES

LIST OF FIGURES

Chapter 1. TRADITIONAL RADIATORS FOR MRI SAFETY EVALUATION OF HUMAN BODY

1.1. **Introduction**

In vivo heating due to radiofrequency (RF) power deposition from transmit coils is a safety concern during magnetic resonance imaging (MRI). MRI requires depositing RF power in the body to produce images. The deposited RF power is absorbed non-uniformly and together with the non-uniform blood flow that redistributes this energy, non-uniform tissue heating is induced, which may result in one or more local regions of clinically harmful temperature rise.

To mitigate the concern of undesirable thermal hazards, the International Electro-Technical Commission (IEC) recommends safe absolute temperature and temperature change thresholds that should not be exceeded during MRI (maximum core and local temperature $\leq 39\ ^0$C, maximum core temperature change of $\leq 0.5\ ^0$C in the Normal mode; maximum core and local temperature $\leq 40\ ^0$C, maximum core temperature change of $\leq 1\ ^0$C in the First Level mode) [1]. However, since it is difficult to determine local temperature change deep inside the body non-invasively with sufficient accuracy and precision, and unpleasant/time-consuming to measure core temperature using temperature probes in every patient undergoing MRI, values of relatively easy to implement net, maximum, forward RF power (or RF power per unit mass or specific absorption rate or SAR) were determined instead, that could be deposited in the body to comply with the temperature guidelines. The values for the RF power (or specific absorption rates (SAR)) were computed using simple thermal

models (e.g., two-node model of Drs Adair and Berglund, Pennes bioheat transfer equation) [1]-[5]. Unfortunately, the models employ such simplifying assumptions that make them invalid and/or result in underestimated local and/or systemic tissue heating for a given SAR. For more on the applicability and limitations of these models, please refer to [6][7].

The IEC recommends the maximum whole-body average SAR of 2 W/kg in the Normal mode and 4 W/kg in the First Level mode for transmit, volume body coils to comply with the temperature guidelines. Maximum SAR limit for the whole-head exposure is 3.2 W/kg in the Normal and First Level modes. The maximum allowable RF energy deposition is recommended as 4 W/kg X 60 min = 240 W·min/kg. No limits are recommended for the local SAR values for volume coils.

In this chapter, we re-evaluate the magnitude and distribution of the MRI induced heating using the new, state-of-the-art, validated, two-compartment Generic Bioheat Transfer Model (GBHTM) for various human body models (adult male, adult female, 9-month pregnant woman) placed inside a 1.5T, 3T and 7T whole body volume coil, in various landmark positions. The results of the GBHTM are compared to those of the conventional, 'simplified', empirical Pennes bioheat transfer equation (BHTE) [7][8]. Since thermal hazards are a function of the temperature-time history – and not just the temperature – corresponding thermal dose (TD) values are computed, as well, per two frequently employed methods, the Cumulative Equivalent Minutes at 43 ^{0}C (CEM43) and Arrhenius equation.

1.2. **Methodology**

A basic description of AIMD induced heating and voltage estimation is introduced in this chapter.

1.2.1. **Anatomical models**

Three whole-body human models are used: an adult male (Duke), and adult female (Ella), and a 9-month pregnant woman. These body models belong to virtual population (IT'IS Foundation, Switzerland). Duke is ~1.77 m tall and weighs ~70.2 kg. Ella is ~1.63 m tall and weighs ~57.3 kg. The pregnant woman is ~1.58 m tall and weighs ~68.5 kg. The pregnant woman model includes a detailed 9-month-old fetus model and amniotic fluid.

1.2.2. **Coils and simulation setup**

Three whole-body coils are considered. The 1.5T whole-body volume coil is modeled as a birdcage, resonates at 64 MHz, and has two excitation ports I and Q. The coil has 16 rungs and the diameter and length of 313.2 mm and 600 mm, respectively. The coil has two sets of capacitors of 50 pF to connect the gaps between the adjacent sections of the end rings and tune the coil to appropriate frequency. Two other capacitors of 75 pF each are used parallel to the two ports for impedance matching. The shielding of the coil has the diameter and length of 350 mm and 1200 mm, respectively.

The 3T whole-body coil is modeled as a birdcage, resonates at 128.23 MHz, and has two excitation ports I and Q, as well. The coil has 16 rungs, and the diameter and

length of 310 mm and 550 mm, respectively. The coil has two sets of capacitors of 13.5 pF each for tuning and matching. The shielding has the diameter of 334 mm and length of 1454 mm, respectively.

The 7T whole-body volume coil is modeled as a transverse electromagnetic (TEM) mode coil, resonates at ~300 MHz, and has 16 independent elements. The coils are modeled as a TEM coil because at ultra-high frequencies (> 3T or 128.23 MHz), TEM structure provides better efficiency and field homogeneity compared to the birdcage structure, when loaded with the human body. The 16 independent elements of the coil connect to the same grounded shielding. Each copper microstrip line propagates TEM mode and is excited by the source between one end of the microstrip line and the outer shielding. Two sets of shunt capacitors are connected between the microstrip lines and shielding to adjust the electrical length to tune each element to resonate at the appropriate 7T Larmor frequency of ~300MHz. The coil has the microstrip line resonant elements with the diameter of 313 mm and length of 450 mm. The shielding has the diameter of 317 mm and length of 950 mm.

The coil and human model alignments are shown in Fig. 1-1. Notice that pregnant woman model is rotated 90° compared to Ella. This is because in practice, typically, normal patients lie on the back while full-term or near full term pregnant women are more likely to lie on the side.

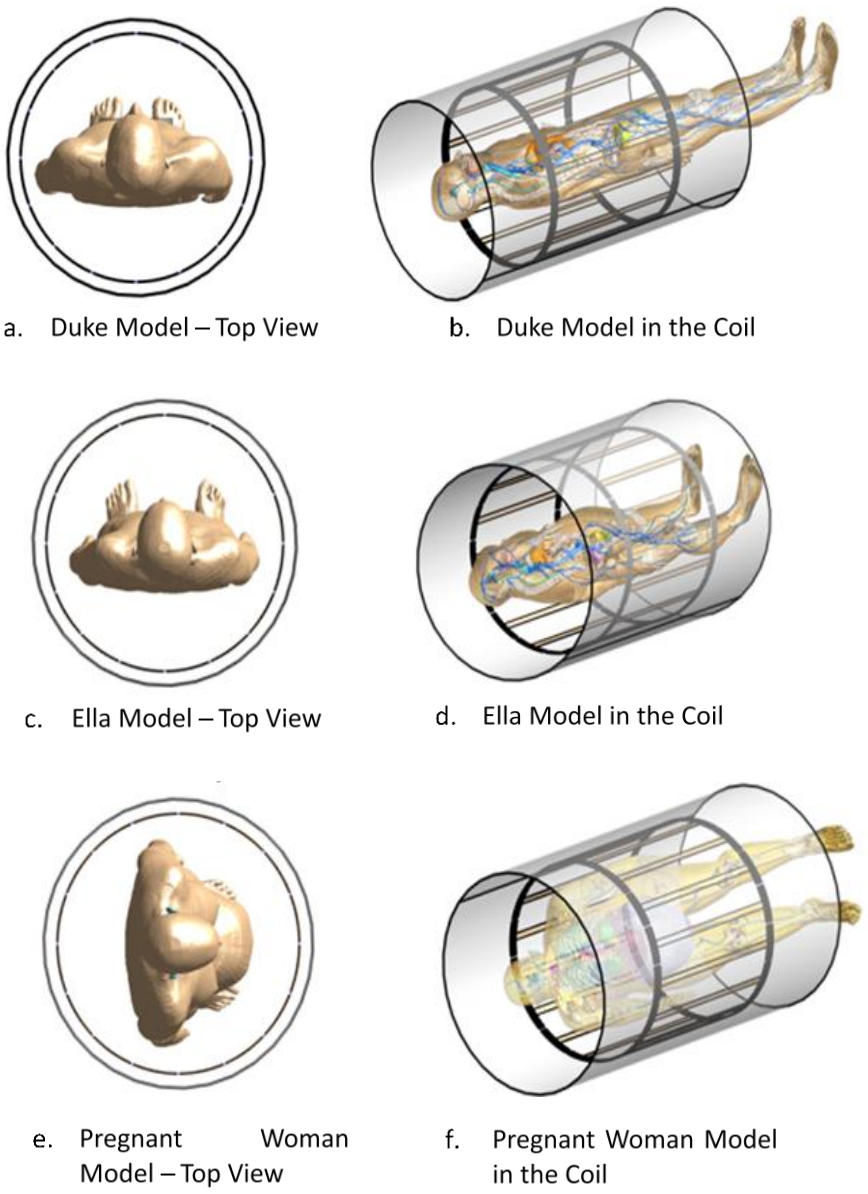

Figure 1-1. (a). Top view of Duke inside in the coil; (b). Duke orientation in coil, lying on the back; (c). Top view of Ella inside in the coil; (d). Ella orientation in coil, lying on the back; (e). Top view of Pregnant Woman inside in the coil; (f). Pregnant Woman orientation in coil, lying on the side.

Four landmark positions are studied – head, heart, trunk, and pelvis. The head landmark is chosen such that the center of the human brain overlaps with the isocenter of the coil. For other landmark positions, the human models are moved along the coil. Landmark positions are presented in Fig. 1-2.

The electromagnetic simulations are performed using commercial FDTD software Sim4Life (ZMT, Zurich, Switzerland) with the grid resolution of ~2.5 mm in the

whole-body models. Broadband simulations are performed for I and Q channel separately to tune the 1.5 T and 3 T birdcage coils. For the 7T TEM coil, broadband simulations are performed with only one source on. All S11 values for the broadband simulations were below -20 db. Single frequency harmonic simulations are then performed for circularly polarized (CP) mode to verify that uniform rotating magnetic field (B1) field is generated.

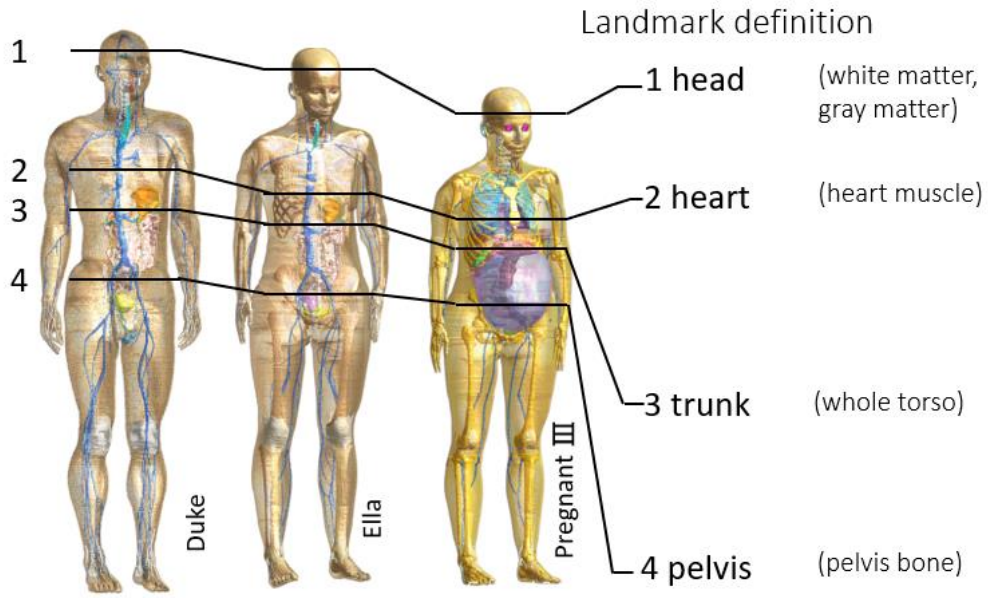

Figure 1-2. Landmark positions.

1.2.3. **SAR modelling and normalization**

RF power deposition per unit volume or Specific Absorption Rate (SAR) is computed per Equation 1-1. Necessary electric field (E) distribution is computed by solving Maxwell equations in the body models by

$$\mathrm{SAR} = \frac{1}{2}\frac{\sigma E^2}{\rho}, \tag{1-1}$$

where E is the electrical field, σ is the electrical conductivity, and ρ is the density. Local SAR is computed in each voxel. 1gm and 10 gm average SAR are calculated by integrating local SAR in nearby 1gm and 10 gm mass by

$$\mathrm{SAR}_{\mathrm{mass}} = \frac{\int_{mass}^{volume\ interation}\left(\frac{1}{2}\sigma E^2\right)dV}{mass}, \qquad (1\text{-}2)$$

where mass is 1 gram or 10 grams.

1.2.4. **Thermal simulation setup**

RF heating is simulated, by solving the two-compartment GBHTM and conventional, 'simplified' Pennes BHTE (In Vivo Temperatures, LLC, Burnsville, MN, USA) [7]. The thermal models take RF power distribution (obtained by solving the Maxwell equations) as one of the inputs. The heating is simulated for the whole-body average SAR of 4 W/kg deposited continuously for 60 minutes (total energy = 4 W/kg X 60 min = 240 W·min). The GBHTM is used since 1) the model is a first principles based, rigorously derived bioheat transfer model with minimum number of assumptions; 2) the model has been validated using ~50-120 kg swine to predict tissue heating for MRI applications; and 3) has been shown to predict, relatively more accurate, in vivo tissue heating compared to the Pennes BHTE [7]-[10]. The conventional, 'simplified', empirical Pennes BHTE is used since the predictions of the 'simplified' BHTE has been used, traditionally, to develop SAR exposure thresholds to limit local in vivo heating. It should be noted, however, that the Pennes BHTE has never been validated for MRI application; violates conservation

of energy; and underestimates tissue heating deep under the skin due to the overestimation the blood-tissue heat transfer rate. For simplicity, thermal simulations were performed by considering that the body models are made up of only seven types of materials: air, skin, fat, bone, lungs, and muscle. This thermal simulation approach is consistent with the one used for the validation of the GBHTM [9][10]. For more on the origin, assumptions, and applicability of different bioheat models, interested readers are encouraged to refer to the material presented in reference [7].

1.2.5. **Thermal dose calculation**

Thermal hazards and tissue effects are a function of the temperature-time history – and not just the temperature. Therefore, the simulated heating results are used to compute thermal dose per two frequently employed methods, the Cumulative Equivalent Minutes at 43 ^{0}C (CEM43) and Arrhenius equation. The CEM43 based thermal dose (TD) is computed by

$$\mathrm{CEM43} = \int_0^{\tau} R^{43-T} dt, \tag{1-3}$$

where T is temperature (^{o}C), t is time (minutes), τ is total time (minutes), and the weighting factor R is equal to 0.5 for $T \geq 43\ ^0$C, and 0.25 for $T < 43\ ^0$C. R is independent of the tissue type [11].

Arrhenius equation based non-dimensional thermal dose (Ω) is computed using by

$$\Omega = \int_0^{\tau} A e^{\frac{-E_a}{RT(t)}} dt, \tag{1-4}$$

where T is absolute temperature (K), t is time (s), τ is total time (s), A is the frequency factor (s^{-1}), E_a is an activation energy barrier (J mol^{-1}), and R is the universal gas

constant (8.3143 J $mole^{-1}$ K^{-1}). The value of the frequency factor *A* and activation energy barrier E_a is chosen as 3.1 x 10^{98} s^{-1} and 6.28 x 10^5 J mol^{-1}, respectively. These values were proposed originally in 1947 by Henriques and Moritz in their seminal papers investigating the effect temperature and time on the induced thermal damage. [12]-[14]. Since then, several values of *A* and E_a have been published for various tissue types and with significant variation. To explain these variations, it has been shown that *A* and E_a are, in fact, dependent on each other and not independent [7]. Thermal dose is computed only for the duration of the heating and thus, presents the minimum total thermal dose that might be accumulated due to the heating as well as cooling of tissue. The baseline temperature is assumed to be 37 ^oC. For more on the origin, assumptions, and applicability of different ways to compute thermal dose, interested readers are encouraged to refer to the material presented in reference [7].

1.3. **Results**

1.3.1. **RF heating and thermal dose of an adult male**

Table 1-1 presents the peak 10 gm and 1 gm average SAR, maximum temperature change (*dT*) in the plane of peak 10 gm and 1 gm average SAR, and peak thermal dose at the end of the heating in the plane of 10 gm average SAR, for an adult male as a function of the field strength (i.e., 1.5 T, 3 T, and 7 T) and landmark positions (i.e., head, heart, trunk, and pelvis).

The heating is simulated for the whole-body average SAR of 4 W/kg deposited continuously for 60 minutes (total energy = 4 W/kg X 60 min = 240 W·min).

Table 1-I. SAR and thermal simulation results for the adult male whole-body mode

Landmark Position		Peak 10 gm SAR (W/kg)	Peak 1 gm SAR (W/kg)	*dT* in peak 10 gm SAR plane (°C) GBHTM/Pennes	*dT* in peak 1 gm SAR plane (°C) GBHTM/Pennes	*CEM43* in peak 10 gm SAR plane (min) GBHTM/Pennes	*Ω* in peak 10 gm SAR plane GBHTM/Pennes
1.5T	Head	116.2	138.5	16.6/12.1	16.2/11.7	>500.0/ >500.0	12.42/1.33
	Heart	42.9	50.7	8.6/4.3	8.5/4.2	106.04/4.53	0.03/0.01
	Trunk	39.2	52.5	8.0/3.8	8.0/3.8	69.45/2.30	0.02/0.01
	Pelvis	44.1	86.3	12.7/8.5	14.4/10.1	> 500.0/298.56	0.75/0.10
3T	Head	67.7	85.9	11.1/6.9	11.1/6.9	> 500.00/91.88	0.23/0.03
	Heart	41.2	76.8	9.1/4.9	9.3/5.1	159.07/10.33	0.05/0.01
	Trunk	56.8	103.6	10.6/6.2	11.4/7.0	437.36/57.01	0.15/0.02
	Pelvis	46.4	78.5	9.6/5.5	9.8/5.6	224.84/25.05	0.07/0.01
7T	Head	109.8	330.6	12.2/8.1	11.1/7.0	> 500.00/222.15	0.52/0.07
	Heart	114.0	123.7	16.1/11.3	16.1/11.3	> 500.00/> 500.00	8.07/0.67
	Trunk	160.1	203.7	21.7/16.7	21.7/16.7	>500.00/>500.00	424.12/33.25
	Pelvis	167.9	209.9	22.3/17.1	22.4/17.2	>500.00/>500.00	>500.00/42.74

For 7T simulations, the data presented in the table is found to be true for most of the tissue. Small regions of excessive heating (i.e., ≥ 50 0C) are found in regions with low cross-sectional area for current flow. These numbers are not reported since it is not clear if such high temperature change is induced due to the coil and/or numerical artifact in the body model.

Fig. 1-3. (a) shows the 10-g average SAR distribution and associated temperature rise in a coronal plane near the center of the adult male model as a function of the field strength and landmark locations. Fig. 1-3. (b) shows the corresponding CEM43 and *Ω* values, at the end of heating. The temperature change is computed based on the GBHTM and 'simplified', traditional Pennes BHTE. Thermal dose is computed at the end of the RF power deposition using the temperatures predicted by the GBHTM and 'simplified', traditional Pennes BHTE. Columns 1-6 present thermal dose calculated per CEM43 approach (1.5T - columns 1-2, 3 T – columns 3-4, 7 T – columns 5-6).

Columns 7-12 present thermal dose calculated per Arrhenius equation-based approach (1.5 T - columns 7-8, 3 T – columns 9-10, 7 T – columns 11-12). Thermal dose is presented as a function of the landmark position (Head – row 1, Heart – row 2, Trunk – row 3, and Pelvis – row 4). The same format is used for all the models following.

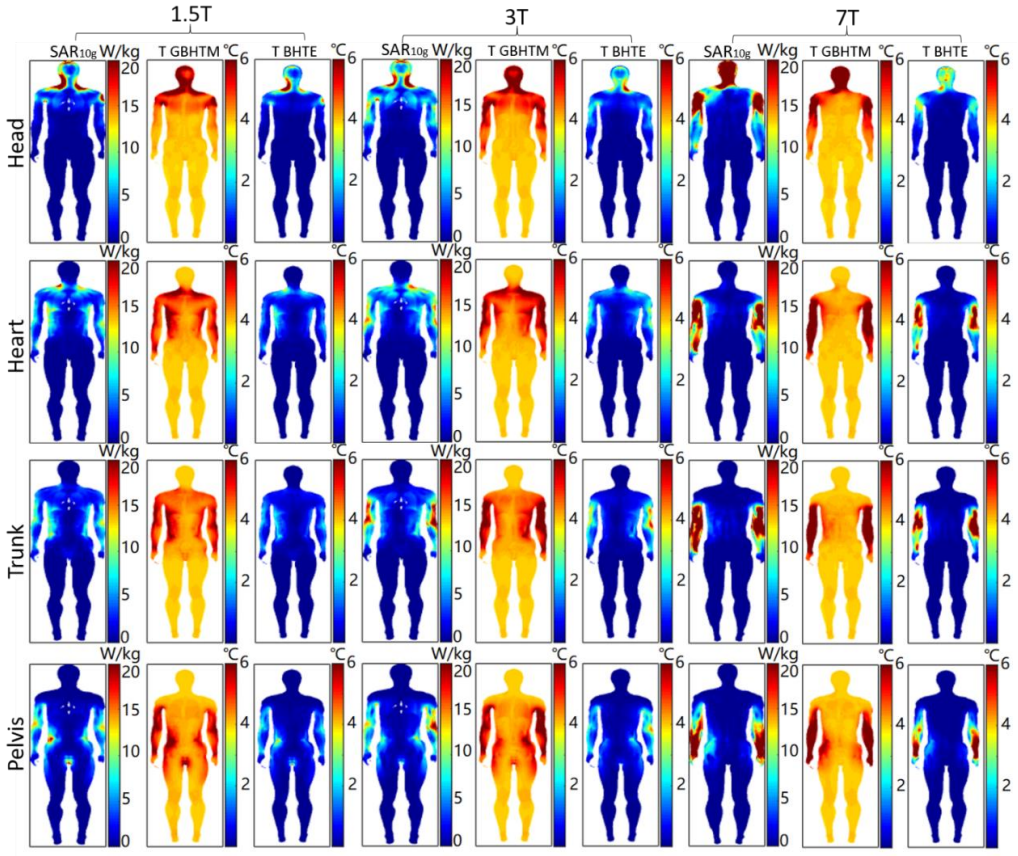

(a)

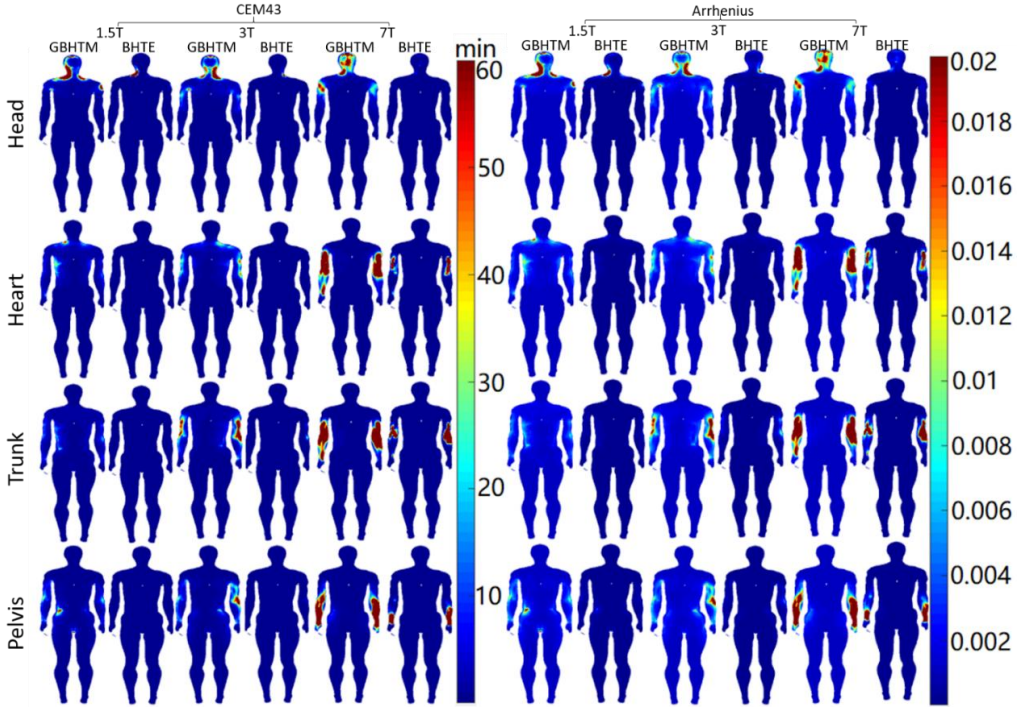

(b)

Figure 1-3. (a) Shows 10 gm average SAR and associated temperature change in a coronal plane near the center of the body of the adult male model in 1.5T, 3T, and 7T as a function of landmark positions. (b) shows the thermal dose distribution.

1.3.2. **RF heating and thermal dose of an adult female**

Table 1-2 presents the peak 10 gm and 1 gm average SAR, maximum temperature change (*dT*) in the plane of peak 10 gm and 1 gm average SAR, and peak thermal dose at the end of the heating in the plane of 10 gm average SAR, for an adult female as a function of the field strength (i.e., 1.5 T, 3 T, and 7 T) and landmark positions (i.e., head, heart, trunk, and pelvis).

Table 1-II. SAR and thermal simulation results for the adult female whole-body model

Landmark Position		Peak 10 g SAR (W/kg)	Peak 1 g SAR (W/kg)	*dT* in peak 10 g SAR plane (°C) GBHTM /Pennes	*dT* in peak 1 g SAR plane (°C) GBHTM/Pennes	*CEM43* in peak 10 gm SAR plane (min) GBHTM/Pennes	*Ω* in peak 10 g SAR plane GBHTM/Pennes
1.5T	Head	101.0	156.2	15.5/10.7	15.5/10.7	>500.00/>500.00	5.18/0.45
	Heart	65.2	106.7	11.2/6.8	12.0/7.5	>500.00/84.08	0.24/0.03
	Trunk	59.5	95.2	10.8/6.4	11.4/6.9	>500.00/62.68	0.18/0.02
	Pelvis	46.1	73.0	10.7/6.4	11.6/7.4	479.56/70.56	0.17/0.02
3T	Head	76.6	112.1	12.9/8.5	13.1/8.6	>500.00/273.03	0.84/0.09
	Heart	49.9	68.1	9.4/4.9	9.2/4.7	180.26/10.40	0.06/0.01
	Trunk	46.6	68.3	10.1/5.8	9.6/5.2	313.29/36.91	0.11/0.01
	Pelvis	40.1	64.8	9.1/4.9	17.1/13.0	156.16/10.18	0.05/0.01
7T	Head	155.1	518.0	16.7/11.8	16.5/11.6	>500.00/>500.00	12.25/1.00
	Heart	106.7	351.5	13.5/8.8	13.4/8.7	>500.00/339.06	1.25/0.11
	Trunk	66.7	113.1	11.5/7.3	17.4/13.2	>500.00/130.48	0.30/0.04
	Pelvis	201.5	627.8	27.3/22.0	21.4/16.2	>500.00/>500.00	>500.00/>500.00

The heating is simulated for the whole-body average SAR of 4 W/kg deposited continuously for 60 minutes (total energy = 4 W/kg X 60 min = 240 W·min). For 7T simulations, the data presented in the table is found to be true for most of the tissue. Small regions of excessive heating (i.e., ≥ 50 0C) are found in regions with low cross-sectional area for current flow. These numbers are not reported since it is not

clear if such high temperature change is induced due to the coil and/or numerical artifact in the body model.

Fig. 1-4. (a) shows the 10-g average SAR distribution and associated temperature rise in a coronal plane near the centre of the adult female model as a function of the field strength and landmark locations. Fig. 1-4. (b) shows the corresponding CEM43 and Ω values, at the end of heating.

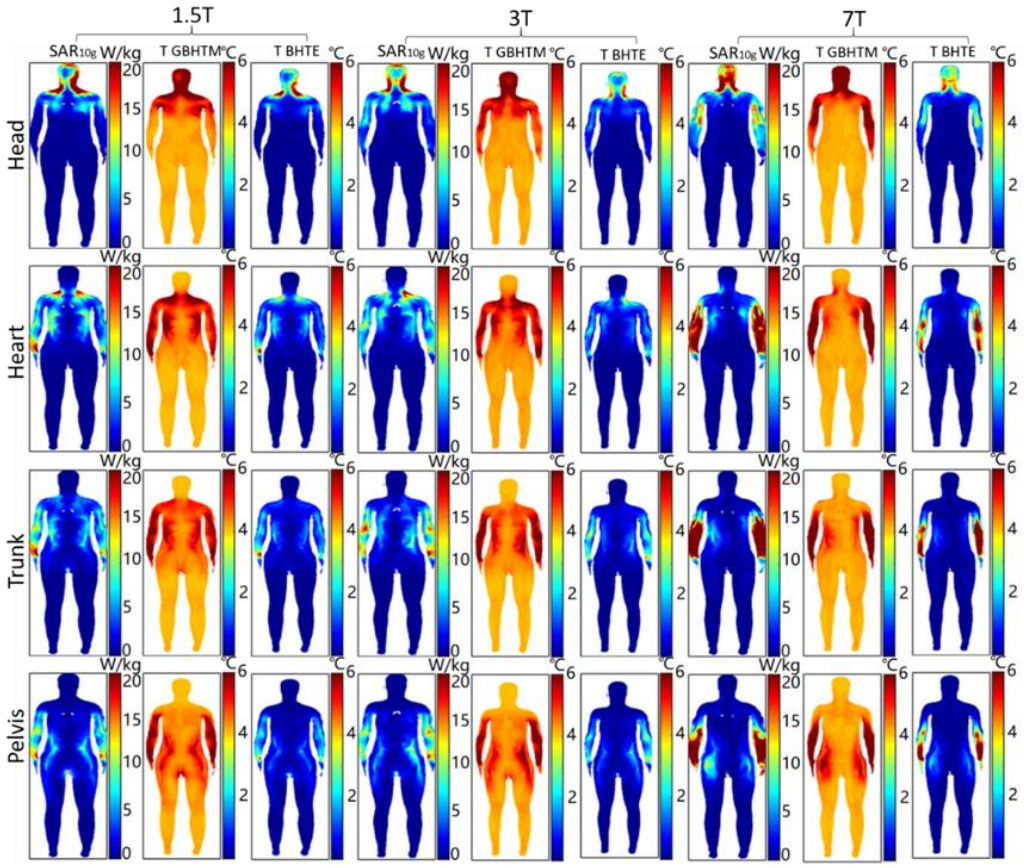

(a)

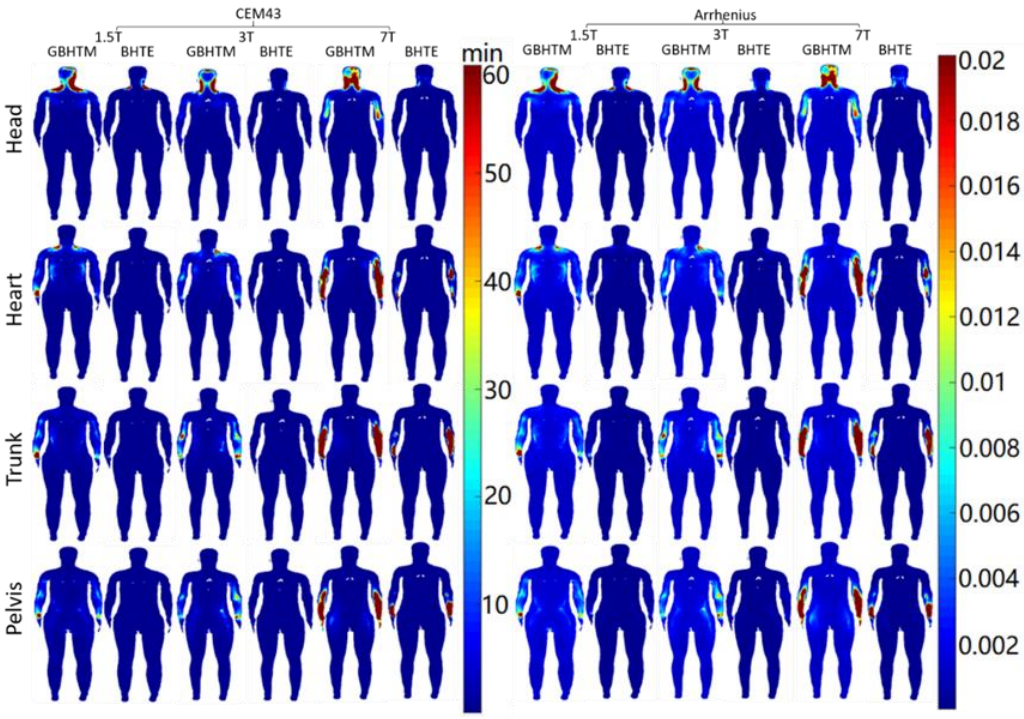

(b)

Figure 1-4. (a) Shows 10 gm average SAR and associated temperature change in a coronal plane near the center of the body of the adult female model in 1.5T, 3T, and 7T as a function of landmark positions. (b) shows the thermal dose distribution.

1.3.3. **RF heating and thermal dose of a pregnant female**

Table 1-3 presents the peak 10 gm and 1 gm average SAR, maximum temperature change (*dT*) in the plane of peak 10 gm and 1 gm average SAR, and peak thermal dose at the end of the heating in the plane of 10 gm average SAR for a 9-month pregnant woman as a function of the field strength (i.e., 1.5 T, 3 T, and 7 T) and landmark positions (i.e., head, heart, trunk, and pelvis).

Table 1-III. SAR and thermal simulation results for the pregnant woman whole-body model

Landmark Position		Peak 10 gm SAR (W/kg)	Peak 1 gm SAR (W/kg)	*dT* in peak 10 gm SAR plane (°C) GBHTM/Pennes	*dT* in peak 1 gm SAR plane (°C) GBHTM/Pennes	*CEM43* in peak 10 gm SAR plane (min) GBHTM/Pennes	*Ω* in peak 10 gm SAR plane GBHTM/Pennes
1.5T	Head	113.8	165.1	17.4/12.8	22.6/18.5	>500.00/>500.00	21.41/2.05
	Heart	57.0	123.1	12.1/7.7	12.5/8.1	>500.00/169.76	0.46/0.05
	Trunk	45.2	89.7	9.2/4.9	10.9/6.6	167.83/10.90	0.06/0.01
	Pelvis	41.5	71.0	8.8/4.5	9.5/5.2	125.21/6.42	0.04/0.01
3T	Head	92.7	124.9	14.4/9.8	15.1/10.6	>500.00/>500.00	2.48/0.24
	Heart	51.6	67.8	9.5/5.4	9.6/5.3	215.36/19.73	0.07/0.01
	Trunk	45.8	62.6	8.8/4.5	8.9/4.7	119.74/5.96	0.04/0.01
	Pelvis	47.9	103.4	14.5/10.4	13.9/9.8	>500.00/>500.00	2.76/0.39
7T	Head	72.5	130.4	12.8/8.7	19.2/15.0	>500.00/341.34	0.83/0.11
	Heart*	129.9	360.6	13.1/8.5	12.3/7.8	>500.00/250.63	0.83/0.08
	Trunk*	157.3	413.1	12.6/8.0	13.3/9.2	>500.00/191.05	0.64/0.06
	Pelvis*	192.9	330.8	15.7/11.0	18.1/13.1	>500.00/>500.00	6.51/0.57

The heating is simulated for the whole-body average SAR of 4 W/kg deposited continuously for 60 minutes (total energy = 4 W/kg X 60 min = 240 W·min). For 7T simulations, the data presented in the table is found to be true for most of the tissue. Small regions of excessive heating (i.e., ≥ 50 0C) are found in regions with low cross-sectional area for current flow. These numbers are not reported since it is not clear if such high temperature change is induced due to the coil and/or numerical artifact in the body model.

Fig. 1-5. (a) shows the 10-g average SAR distribution and associated temperature rise in a coronal plane near the center of the pregnant woman model as a function of the field strength and landmark locations. Fig. 1-5. (b) shows the corresponding CEM43 and Ω values, at the end of heating.

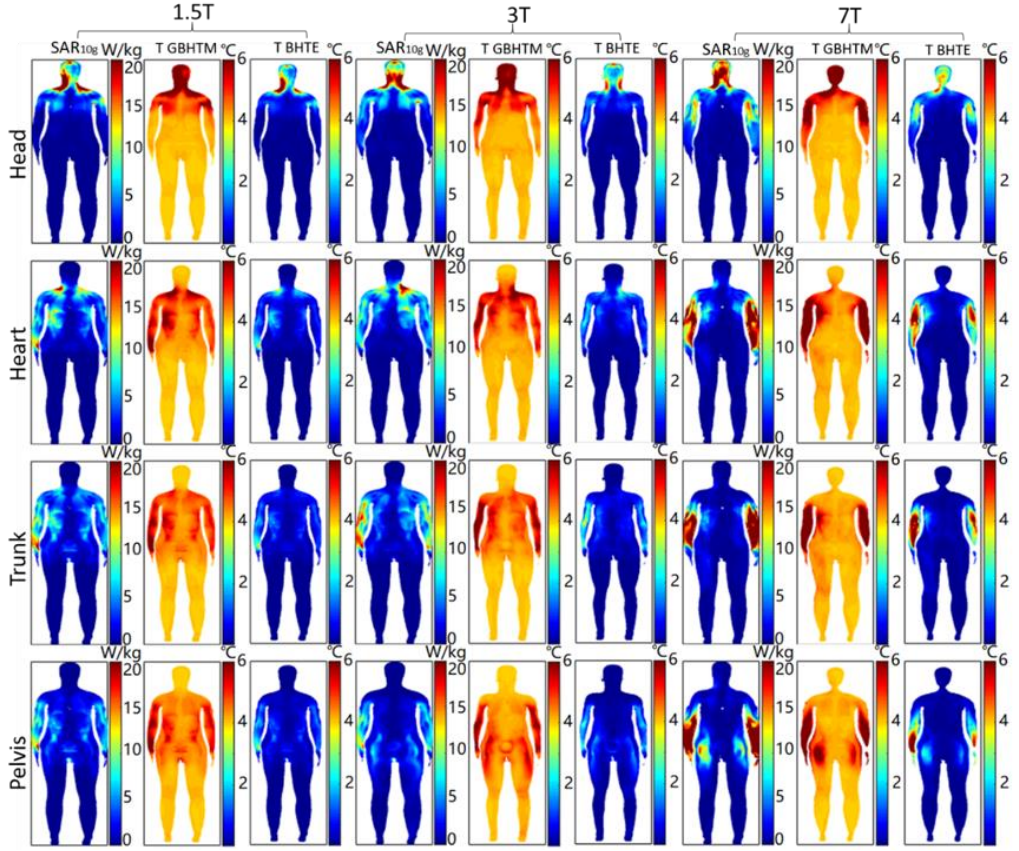

(a)

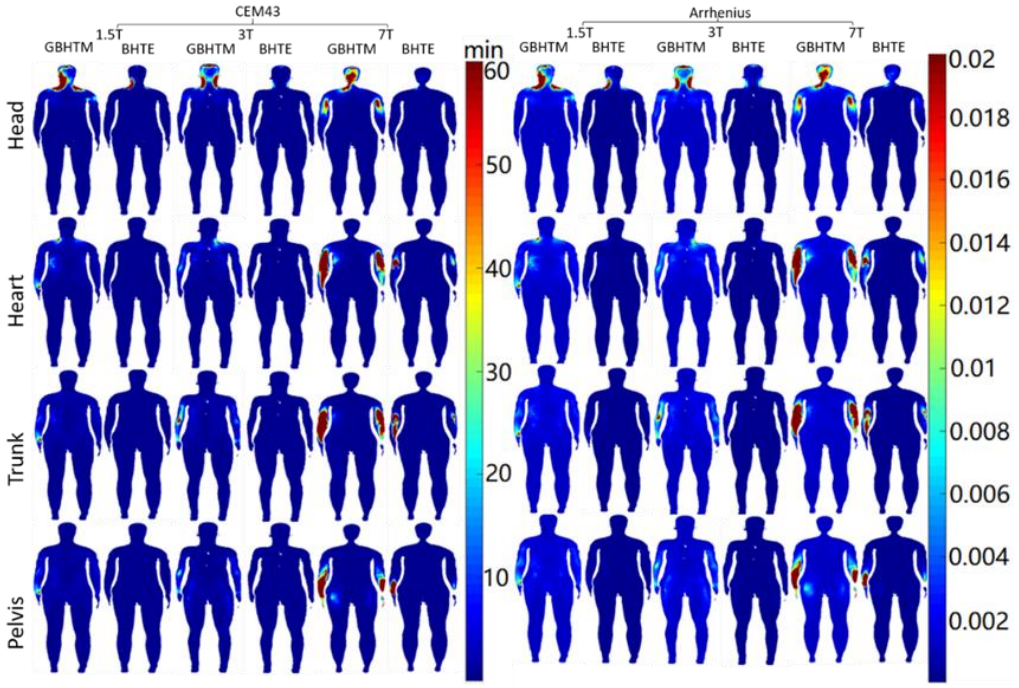

(b)

Figure 1-5. (a) Shows 10 gm average SAR and associated temperature change in a coronal plane near the center of the body of the pregnant women model in 1.5T, 3T, and 7T as a function of landmark positions. (b) shows the thermal dose distribution.

1.4. **Discussion**

Several important observations are made regarding the in vivo tissue heating induced due to the RF power deposition during MRI. First, the induced heating is non-uniform (Fig. 1-3. (a), Fig. 1-4. (a), Fig. 1-5. (a)). This is so because electromagnetic (EM) as well as thermal properties of the body are non-uniform resulting in non-uniform RF power deposition and heating. The observation suggests that the rectal or core temperature change measurement alone may have limited applicability in helping determine if an MRI study produced local temperatures that exceeded recommended safe temperature thresholds. Local heating must be determined with sufficient accuracy to ensure compliance with the IEC recommended safe temperature thresholds and improve patient safety.

Second, the new validated, mechanistic GBHTM predicts greater in vivo heating compared to the conventional, simplified Pennes BHTE. (Fig. 1-3. (a), Fig. 1-4. (a), Fig. 1-5. (a)). This is because the GBHTM allows for the blood temperature to vary per conservation of energy. However, the Pennes BHTE does not allow for the blood temperature to vary. Keeping the blood temperature artificially and non-physiologically constant at the baseline core temperature and using blood perfusion values with non-equilibration constant of zero to compute blood-tissue heat transfer rate makes the Pennes BHTE violate conservation of energy and overestimate the blood-tissue heat transfer rate consequently underestimating the tissue temperature rise compared to the predictions of the GBHTM.

Third, recommended safe in vivo temperature change thresholds are exceeded with allowable whole-body average SAR values, when heart, trunk, or pelvis (Fig. 1-3. (a), Fig. 1-4. (a), Fig. 1-5. (a)) is in the isocenter. This is expected because the maximum allowable whole-body average SAR exposure values were determined using the two-node model of Drs Adair and Berglund, which is unable to account for the non-homogeneous distribution of RF power, and the conventional, simplified Pennes BHTE, which overestimates the thermal interaction between the blood and tissue.

Fourth, temperature in the brain and most of the core is not expected to exceed ~1.5^{0}C during a properly conducted head exam. However, local temperatures in limited regions may still exceed this value. This is so since RF power during a head exam is limited by the whole-head average SAR of 3.2 W/kg – instead of the whole-body average SAR. Since temperature change scales linearly with power, appropriate scaling for a realistic head exam will suggest that the brain and most of the core temperature is not likely to exceed 1.5 ^{0}C due to the whole-head average SAR deposition of 3.2 W/kg for an hour. It should be added however, that in case an MR system assumes that the whole-body average SAR of 3.2 W/kg is equivalent to the whole-head average SAR of 3.2 W/kg, temperature changes are expected to exceed 1.5 ^{0}C, as can be seen from Fig. 1-3. (a), Fig. 1-4. (a), Fig. 1-5. (a) by scaling the temperature change results by 80%.

Fifth, thermal hot regions may be produced deep inside the body away from the skin and its thermal receptors. Therefore, the absence of patient thermal sensation may not be interpreted as the absence of local in vivo heating exceeding the recommended safe temperature thresholds. Excessive, local in vivo heating away from the skin and its

thermal receptors cannot be consciously 'felt' by a person, which could prevent a patient/technician/clinician from responding until it is too late to avoid redness, burning, etc. Computational tools, like the GBHTM, may help accurately determine in vivo RF heating to keep temperatures below desired thresholds during MRI. CEM43 value of ≥ 60 minutes and Arrhenius equation based non-dimensional thermal does value of ≥ 0.02 are computed for various locations inside the body for maximum allowable whole-body average SAR (i.e., 4 W/kg) and energy (i.e., 240 W·min/kg) (Fig. 1-3. (b), Fig. 1-4. (b), Fig. 1-5. (b)). The CEM43 of ≥ 60 minutes (and equivalent Arrhenius equation based non-dimensional thermal does value of ≥ 0.02) has been shown to reduce cell viability by 90% in in vitro experiments [7], [11].

Comparing the present study with previous studies, Shuman et al. measured an average deep tissue in vivo temperature change of 4.2 ^{0}C/hr in dogs exposed to the whole-body average SAR of 4 W/kg in 1.5 T. The temperature increase in deeper tissue was found to be greater than the temperature increases in superficial tissue [15]. Barber et al. measured the core temperature change of 1.26-1.80 ^{0}C/hr and the subcutaneous skin temperature change of up to ~6.3 ^{0}C/hr in sheep exposed to the whole-body average SAR of 4 W/kg in 1.5 T [16]. Kido et al. measured a mean temperature change of 0.5 ^{0}C in the axilla due to the whole-body average SAR exposure of 0.8 W/kg for 17 min. in 1.5 T (i.e., mean temperature change rate of 8.82 ^{0}C/hr at the whole-body average SAR of 4 W/kg) [17]. Shellock et al. measured a scrotal skin temperature change of 0.2-3.2 ^{0}C due to the whole-body average SAR exposure of 0.56-0.84 W/kg for 23 min in 1.5 T [18]. Shellock et al. measured an insignificant change in the rectal

temperature and a change of up to 7.5 ^{0}C in the skin temperature due to the whole-body average SAR exposure of 2.7-4.0 W/kg for 30 min in 1.5 T [19]. Shellock et al. measured a mean tympanic membrane temperature change of 0.4 ^{0}C and a mean skin temperature change of -0.5-3.6 ^{0}C due to the whole-body average SAR of 6 W/kg for 16 min in 1.5 T [20]. Boss et al. measured skin temperature changes of 0.88 ^{0}C in human volunteers due to the whole-body average SAR exposure of 1.60 W/kg for ~6.75 min and 2.85 W/kg for an additional 4.25 min (i.e., total exposure of ~10 min) [21]. Shrivastava et al. measured and simulated the core, brain, and hot region temperature of 1.5 ^{0}C, 2.5 ^{0}C, and 3.8 ^{0}C, respectively, in swine when the swine head was placed in the isocenter of a 3 T coil due to the whole-body average SAR of 2.7 W/kg deposited for an hour. Further, they measured and simulated the core, brain, and hot region temperature of 1.6 ^{0}C, 1.8 ^{0}C, and 5.2 ^{0}C, respectively, in swine when the swine trunk was placed in the isocenter of a 3 T coil due to the whole-body average SAR of 2.8 W/kg deposited for an hour [9]. All of these previously published values are comparable to the data presented here for the temperature change.

Regarding the limitations of this study, the heating depends on the human geometry, tissue composition and relative distribution, coil configuration, placement of human body inside the coil, electromagnetic and thermal properties of the body, skin surface conditions (e.g., clothing, sweating, etc.), and ambient conditions. Thus, the results presented herein are limited to the cases studied. Readers are encouraged to solve the GBHTM using additional body models, coils, placement of body models inside coils, and skin surface and ambient conditions to develop deeper understanding

of the magnitude and distribution of the MRI induced tissue heating in humans to improve safety as well as performance.

1.5. **Summary**

A computational study is performed to systematically analyse the RF power distribution, related temperature rise, and accumulated thermal dose during heating, in an adult male, an adult female, and a pregnant woman whole-body model due to power deposition from a 1.5 T, 3 T, and 7 T whole-body volume coil placed in four landmark positions (i.e., head, heart, trunk, and pelvis). The RF heating is computed using the new, validated mechanistic generic bioheat transfer model (GBHTM) and empirical, simplified Pennes bioheat transfer equation (BHTE). Results show that the temperatures, exceeding recommended safe thermal thresholds of 1 ^{0}C, may be produced deep inside the body away from the skin and its thermal receptors with allowable whole-body average SAR values. Measuring rectal and skin temperature changes may not be sufficient for determining temperature changes in hot regions deep inside the body, and thus, in concluding a thermally safe MRI scan. Future studies employing the GBHTM to predict in vivo heating along with appropriate verification of the GBHTM results in humans may help significantly enhance our understanding of the RF safety in high and ultra-high field MRI and develop next generation of faster, safer, and more flexible SAR as well as temperature-controlled MR systems.

1.6. **Supplementary material: 3T coil field validation**

To validate the simulated field distribution, we tried to measure the SAR inside a standard ASTM phantom under the exposure of the 3T coil used in this study, the validation of other coils should follow the same method [22].

There are some frequently used to validate the EM field distribution, such as using a E probe to measure the E field directly, but such a method will have influence on the field distribution as the E probe and the connecting cables usually have relatively large dimension, and the probe needs to be carefully calibrated as the measurement results are strongly dependent on the surrounding materials. Another method used by many researchers is to load an ASTM standard phantom inside the coil, the high loss phantom gel will have the dominant influence on the field distribution, thus make the E field in the phantom stabler than it in an empty coil, especially when we put a measurement equipment into the coil. And in the loss gel, the E field can be measured using the induced temperature rise, which can be considered to be linear to the SAR within a wide range. However, the induced SAR in the empty gel is always at a low level, to measure the temperature more accurately, we put a 10 cm titanium rod at different locations of the coil to enhance the induced local SAR. Then we attached optical fiber-based temperature probes to each end of the rod to get the temperature rise and compare it with the temperature rise we directly get from the simulation using the same setup, this will give us a stable, accurate and easy-to-implement way to validate the simulated field distribution.

As shown in Fig. 1-6, we load an ASTM phantom coil to the center of the 3T coil used in this study and put a titanium rod at 6 different positions to measure the temperature rise and compare with the results from the simulation. The conductivity of the gel is 0.47S/m, the permittivity of the gel is 78. The ASTM standard phantom has the size shown in Fig. 1-7, and we filled 9 cm gel into the phantom, the rod is put at the center slice of the gel, which is 45 mm from the bottom and 45 mm from the surface of the gel. The temperature rise is measured after the power is turned on for 900s, and before the test, we waited 180s to let the background temperature to reach a stable status, the power is normalized so that the whole-body averaged SAR of the gel is 2W/kg.

The measured temperature rise results are compared with those from the simulation, as shown in Table 1-4. As we can see from these results, the measured temperature rises results have good agreement with those from the simulation for most locations, which validated our simulation field distribution.

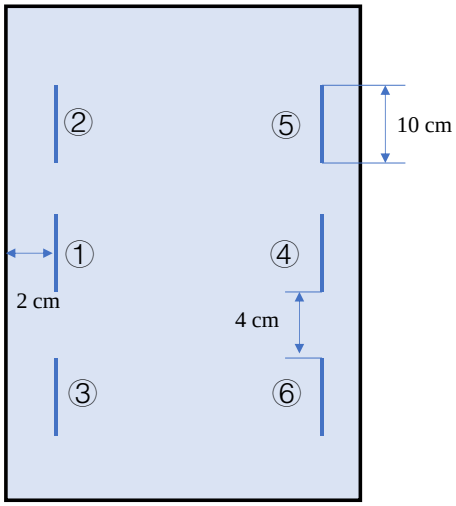

Figure 1-6. Positions of the rod used for the validation experiments.

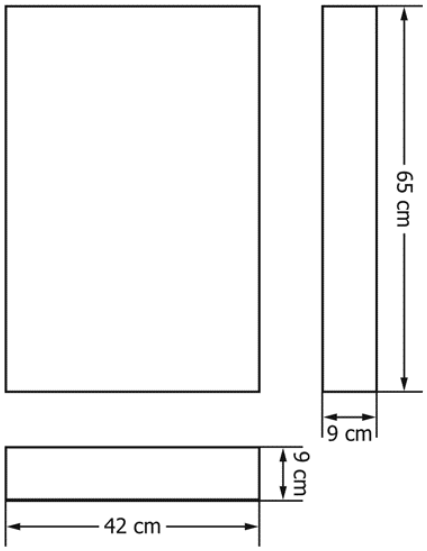

Figure 1-7. Size and structure of the ASTM 2182 standard phantom.

Table 1-IV. Rod Temperature rise results comparison

position	1	2	3	4	5	6
Simulated T rise (℃)	25.2	23.1	23.7	22.1	22.9	24.4
measured T rise (℃)	22.9	16.4	20.8	31.4	30.6	24.5
Percentage error (%)	10.04	40.85	13.94	29.62	19.88	6.88

Chapter 2. SAR MANAGEMENT OF HUMAN BODY IN A MULTI-CHANNEL MRI COIL BASED ON ARTIFICIAL NEURAL NETWORK

2.1. **Introduction**

Ultra-high field magnetic resonance imaging (MRI) has been a popular topic for its high signal-to-noise ratio (SNR), the increased sensitivity, spatial resolution gives it potential to be used in high quality neural imaging, brain disease diagnosis and many other clinical and research medic fields [23]-[25]. However, compared with traditional 1.5 T MRI, the higher frequency of 3 T and 7 T means shorter wavelength, and the field inhomogeneity in the human body will be more severe than it under 1.5 T and 3 T imaging, more localized field will always bring higher local induced special absorption rate (SAR), which can burn human body tissue and lead to the failure of implantable medical devices (IMDs) in human body.

Moreover, to compensate the B1+ field inhomogeneity which will lead to poor imaging quality, the RF-shimming method need to be applied, which will tune the input signal magnitude and phase of the many ports of the multi-channel coil. The resulted varied excitation combinations will make the hot spot, which is the location with the highest SAR, move around the human body and makes the SAR management hard to process. Therefore, optimization methods are necessary to be applied to estimate the induced SAR in the complicated incident field condition.

Over the past few decades, researchers have paid huge efforts on quick prediction of the SAR under RF-shimming condition for multi-channel coils. The most famous work is called virtual observation points (VOP) which is done with Siemens [26].

However, the generation of those virtual observation points will be highly model specified, and the overestimation of the SAR can be considerable. Another method which can reduce the complicity and cooperate with the VOP is called Q-matrix. By extracting the field information and getting rid of the excitation information, a matrix independent of the signal on the ports can be built and used to predict the SAR quickly.

Nowadays machine learning has shown its ability on solving nonlinear, multi-input problems [27]-[30]. In this chapter, we used an artificial neural network (ANN), designed to follow the path of human brain analyzes, to find the relationship between the input vector and the output hot spot location. And one important conclusion from former research is that only a few of points, not all the locations on human body, can be the hot spot of SAR. By storing the Q matrix for the possible hot spot locations only and predicting the hot spot under certain input vector among those values, we can greatly decrease the information needed and the computation time, thus gives a quick estimation of the induced peak SAR value [31]. In this chapter we will introduce two methods to predict the peak of human body under certain RF shimming set, the first one will use ANN to predict the SAR level directly, while the second method will use clustering algorithm to group the possible peak SAR locations to greatly reduce the number of Q matrix we need to consider.

2.2. **Methodology**

2.2.1. **Simulation setup**

To get the SAR value in experiments is nearly not possible to process, so the data used in this chapter is based on full-wave electro-magnetic (EM) simulations. The software we use is a commercial finite difference time domain (FDTD) EM simulation software Sim4life (ZMT, Zurich, Switzerland).

The coil used in this study is an 8-channel body transmit array, which has 8 independent excitation ports on each radiation element, the structure of the coil is shown in Fig. 2-1. Tunning elements are added on each element to tune the element to resonant at the desired frequency (200MHz), and S11 is under -6dB for the empty coil (for a loaded coil the lossy human body is loaded inside the S11 will be better than the empty coil), as shown in Fig. 2-2. The coil has the radius of 300 cm and the length of 504 cm, the radius of the shielding is 332 cm, and the length of the shielding is 1000 cm.

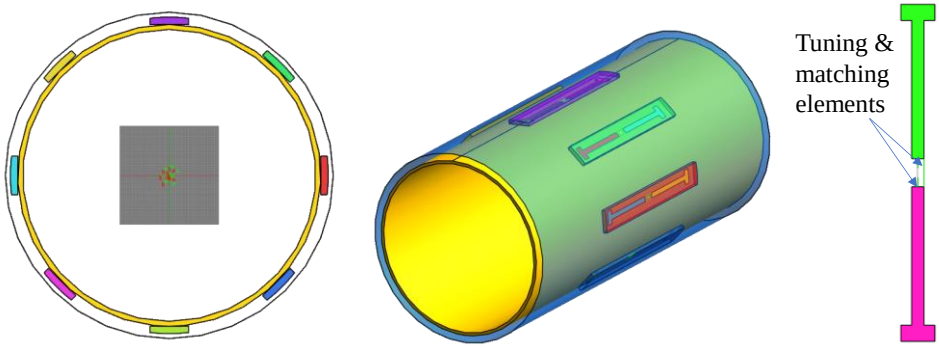

(a) (b) (c)

Figure 2-1. Structure of the coil used in this study. (a) is the top view of the coil with the shielding, (b) is the side view of the coil, (c) shows the single radiation element with the tuning and matching capacitors.

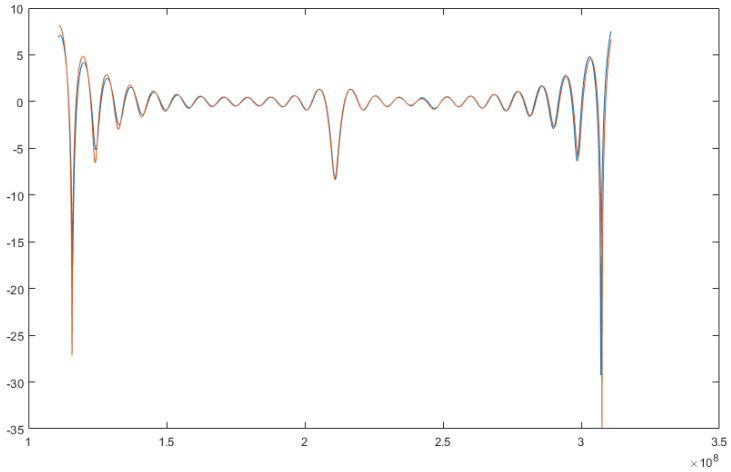

Figure 2-2. S11 around -10bB for the empty coil with the tuning and matching capacitors, x axis is the frequency, y axis is the S11 in db.

The induced electrical field *B1+* field are simulated for each element independently, and when a certain input vector composed of 8 complex input signals is applied, we will add up the field of each channel together with the complex input as the weighting factor by

$$E(r) = \mathbf{S}' \cdot \mathbf{E}(r), \tag{2-1}$$

where $\boldsymbol{S} = [S_1, S_2, \cdots S_8]'$ is a complex vector represents the magnitude and phase of the input on the single element. And $\boldsymbol{E}(r)$ is an 8×1 complex vector whose element $E_i(r)$ is the induced electrical field at the location expressed as *r*. In such a way, we can run 8 independent simulations only, and applied any input vector we need and get unlimited numbers of combined electrical field. And following the way method, we can also get the *B1+* field for the certain input vector.

2.2.2. **Virtual family human model**

The human model used in this study is the adult model Duke from the virtual population [32]. This model is a high-resolution whole-body virtual human model with

a height of 1.77 m and a weight of 70.3 kg. Fig. 2-3. shows the duke model. The EM properties of the human model is from the IT IS material database. In the human model simulation, all the coil elements have a maximum mesh step size of 5 mm; the human model is meshed with the maximum step size of 2.5 mm, the number of the total voxels for each simulation is from 60 M cells to 90 M cells.

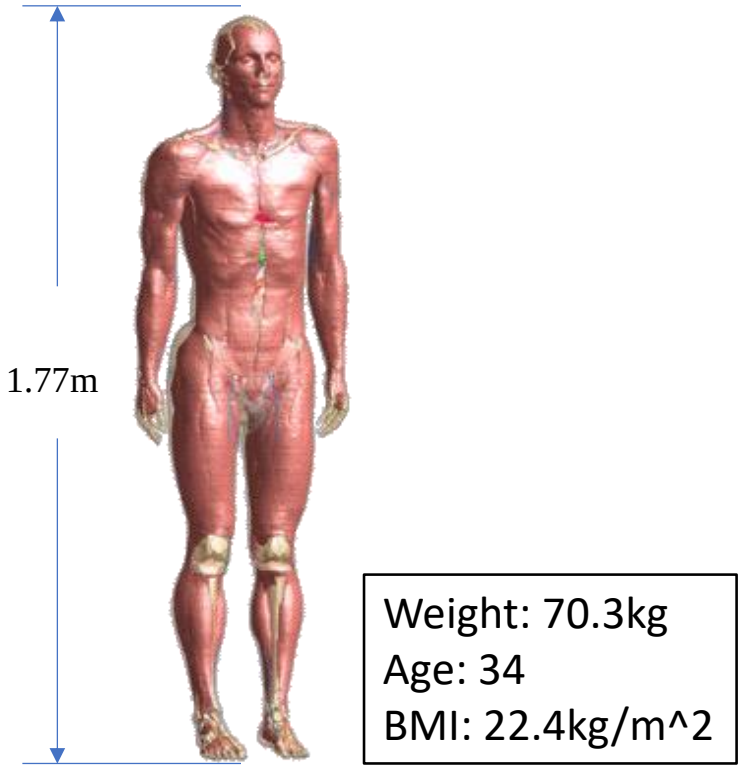

Figure 2-3. Duke model from the virtual population.

2.2.3. **Q matrix**

Based on equation (1) we can get the incident electrical field, but the for the induced SAR which consists of square of *E*, this will become a nonlinear problem and the *E* information will be coupled with the input vector information by

$$\mathrm{SAR} = \frac{1}{2}\frac{\sigma E^2}{\rho}. \qquad (2\text{-}2)$$

Local SAR can be strongly influenced by the mesh size and tissue properties, so to estimate the induced heating using SAR, the local SAR should be averaged over a certain mass, depending on the exposure conditions, the average local SAR over the volume of 1-g or 10-g mass are always used, here in the empty human body model, we use the 10-g averaged SAR by

$$\mathrm{SAR}_{\mathrm{mass}} = \frac{\int_{mass}^{volume\ interation}\left(\frac{1}{2}\sigma E^2\right)dV}{mass}. \tag{2-3}$$

Using the Q matrix method, we can extract the tissue properties and field distribution feature from the incident field by

$$\begin{aligned}\mathrm{SAR}_{\mathrm{wb}} &= \frac{\int_v \sigma(r)|E(r)|^2 dv}{\int_v \rho(r)dv} \\ &= \frac{\int_v \sigma(r)|\boldsymbol{S}' \cdot \boldsymbol{E}(r)|^2 dv}{\int_v \rho(r)dv} \\ &= \boldsymbol{S}' \cdot \frac{\int_v \sigma(r)(\boldsymbol{E}(r) \cdot \boldsymbol{E}(r)^{\dagger})^2 dv}{\int_v \rho(r)dv} \cdot \boldsymbol{S}^* \\ &= \boldsymbol{S}' \cdot \boldsymbol{Q}_{wb} \cdot \boldsymbol{S}^*\end{aligned} \tag{2-4}$$

where the $\boldsymbol{E}(r)$ is the incident electrical field, and $\sigma(r)$, $\rho(r)$ are the conductivity and density of human tissue. The vector $\boldsymbol{S}$ contains the input signal information and $\boldsymbol{Q}_{wb}$ contains the tissue and field distribution information, here wb means integral for the whole-body area, so the Q matrix here is for the calculation of whole-body averaged SAR (wbSAR), is we change the integral region to a certain location with 10-g tissue mass, the resulted Q matrix will be used for the calculation of the 10-g averaged SAR for that location.

By using such method, the Q matrix can be pre-calculated, and it will be independent of the input vector, now if we know the peak SAR location, we can store

the 8x8 matrix for the peak location only, and get the SAR with one-step calculation, which has almost no computation resource and time cost. Such a feature makes the Q matrix extremely useful for multi-channel coil SAR calculation.

2.2.4. **Artificial neural network**

The artificial neural network we used in this study is a three-layer feed-forward network, it has two hidden layers, 15 sigmoid neurons each, and one output layer with a linear neuron, the architecture of the artificial neuron network is shown in Fig. 2-4.

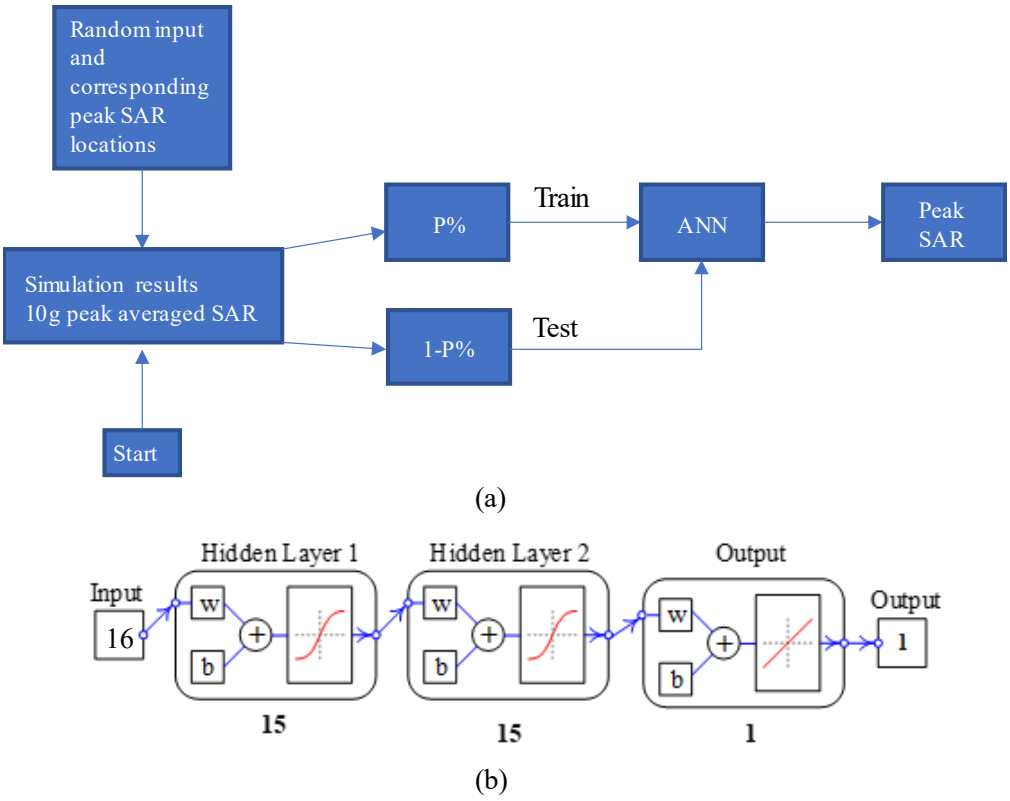

Figure 2-4. Architecture of the artificial neural network, (a) shows the flowchart of the SAR prediction, (b) shows the structure of the layers in the artificial neural network.

The ANN is trained to generalize the nonlinear relationship between the input vector and the peak SAR level. The two hidden layers are added to make the unknow function smoother, thus make the prediction more accurate. Using the given Q matrix

method and the 8-channel independent simulation results, we generated 10000 random excitation vector, and then we divide the human model into 5 regions, which are the head, the trunk, the legs, the left and right arm region, then we find the peak SAR locations for each region of each excitation vectors, so we got 50000 groups of random input-output peak SAR locations, to show the network performance, we used first start with using 1600 RF shimming sets of the data are used to train the network within a limited shimming set range (magnitude ratio of channel varies from 1 to 2, phase variation compared with circular polarized mode from -30 to 30 degree), and other 400 RF shimming sets are used to validate the network, and then we started to train the network at wider range (magnitude ratio of channel varies from 1 to 2, phase variation compared with circular polarized mode from -30 to 30 degree) with 250 RF shimming sets, and add training sets each time to check the data needed to get converged. We repeated the same training process for the duke model at three different areas the human head, trunk, and extremities under the exposure of the 8-channel transmit array.

2.3. **Results**

The ANN is trained with 1600 sets of the data, the training and validation results are shown in Fig. 2-5. The trained ANN is used to predict the SAR levels with random input vectors, then the resulted ‘predicted peak SAR’ is compared with the ‘simulated peak SAR’, which is got from the simulation directly, during which process we calculate the induced SAR for the whole human body, and then get the 10-g averaged

for each pixel of the simulation, and then find the maximum value. The comparison results are shown in Fig. 2-6.

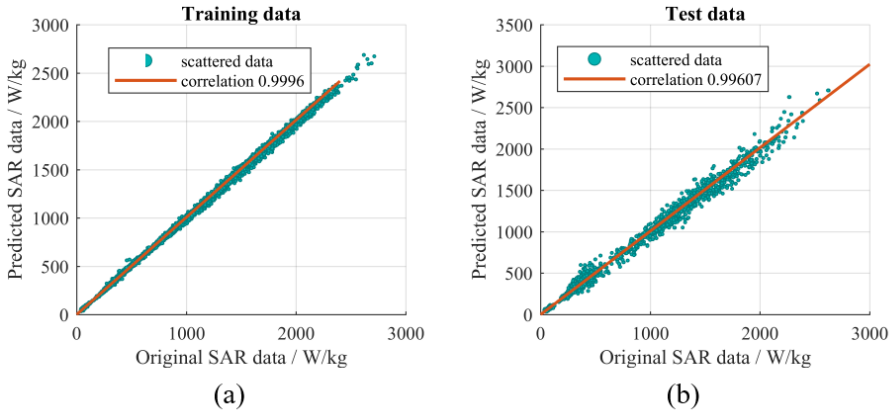

Figure 2-5. Training of the ANN. (a) shows the regression and scatter data for training and (b) for testing.

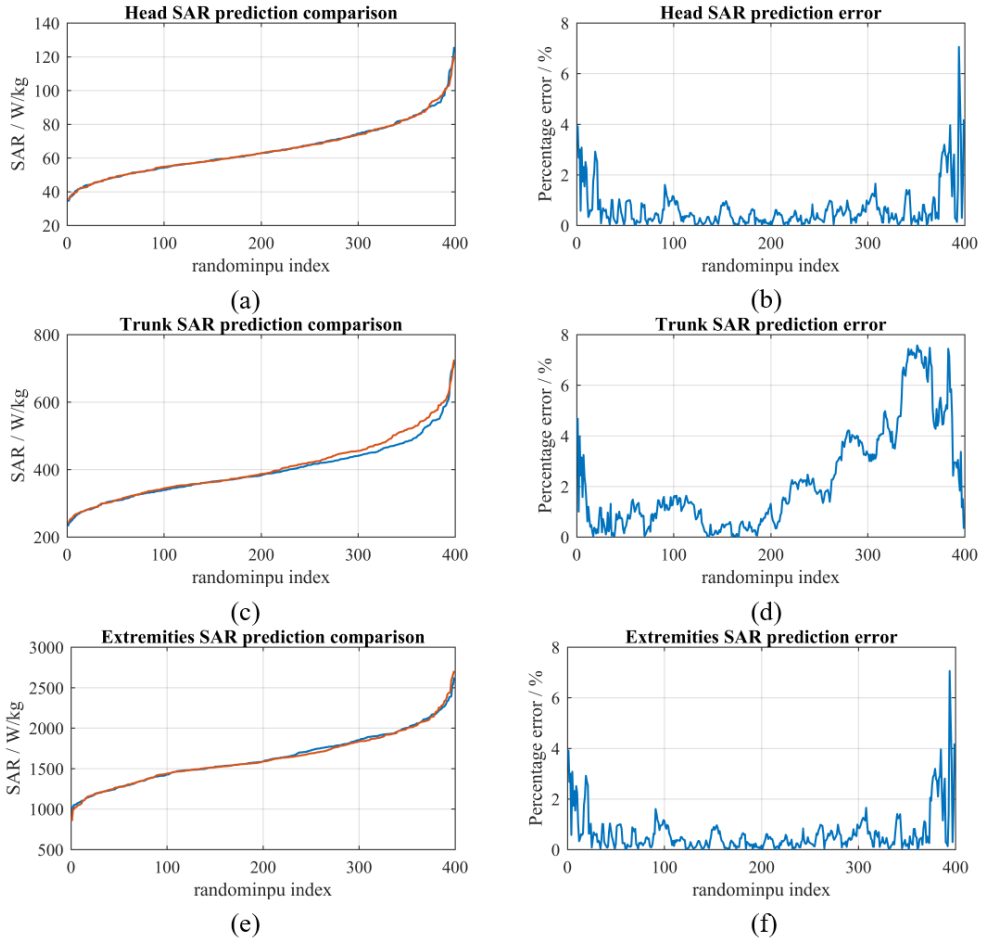

Figure 2-6. ANN predicted SAR comparison and percentage error for (a)(b) head peak SAR, (c)(d) trunk peak SAR and (e)(f) extremities peak SAR, orange line indicates the original data, blue line indicates the predicted SAR level.

Then to test the data amount needed to train the network with wider shimming sets

range, we gradually added the training data amount and the tested mean error and maximum error for the head, trunk, and extremities are shown in Fig. 2-7.

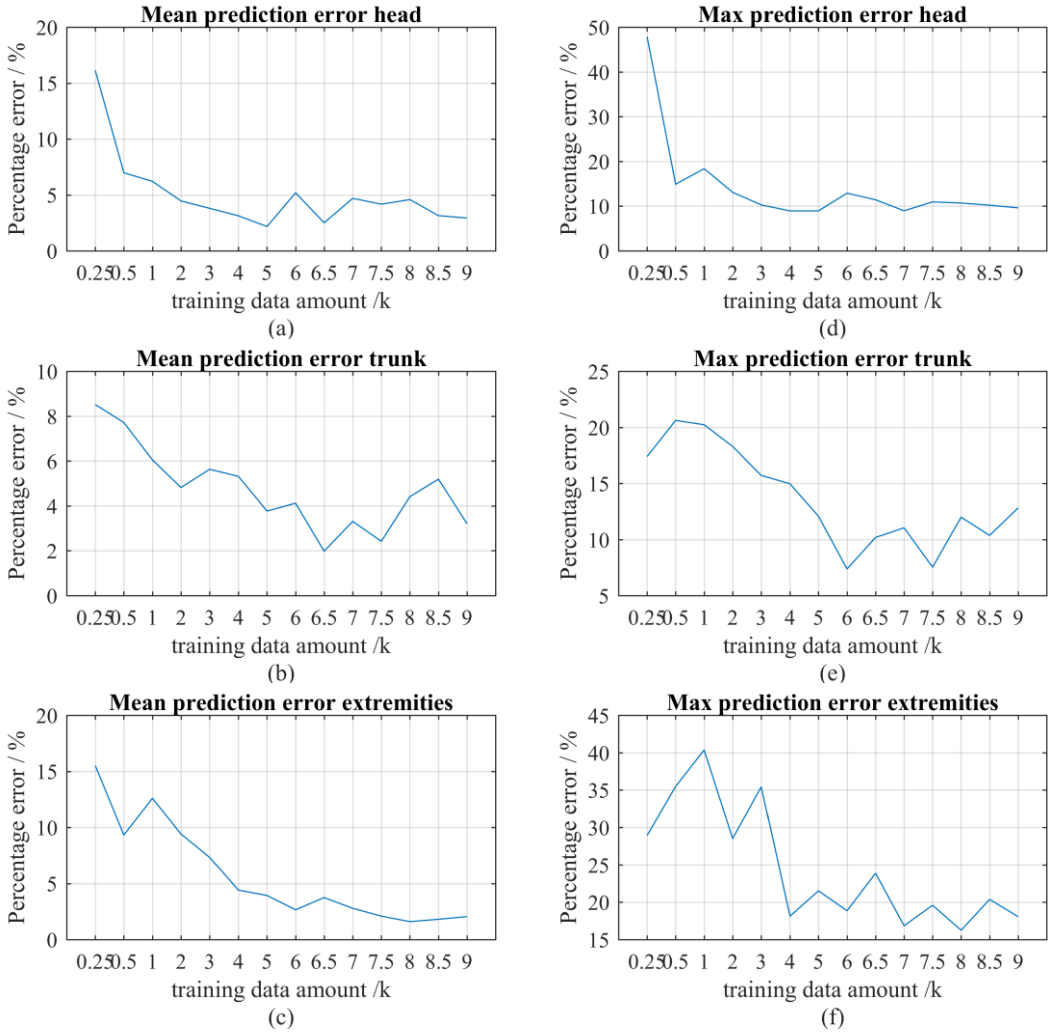

Figure 2-7. Data amount used for the training and the resulted testing errors.

As mentioned in 2.1, peak SAR locations will only be observed at certain locations, so another method to predict the SAR level at given RF shimming sets quickly is to use randomly generated RF shimming sets to find enough possible peak SAR locations, then we use clustering algorithm to group them into fewer cluster and when we evaluate the SAR level, we only consider those locations, this will greatly reduce the amount of the Q matrix we need to consider, and 2000 training sets and 100 testing sets are used to show the results of this method, the results are shown in Fig. 2-8 for landmark head, the

full locations means we store the Q matrix for all the possible peak SAR locations we found directly, while 100, 50 and 10 locations means we used clustering algorithm to group them into 100, 50 and 10 clusters in each region. Fig. 2-9 and Fig. 2-10 show the results for landmark trunk and ankle.

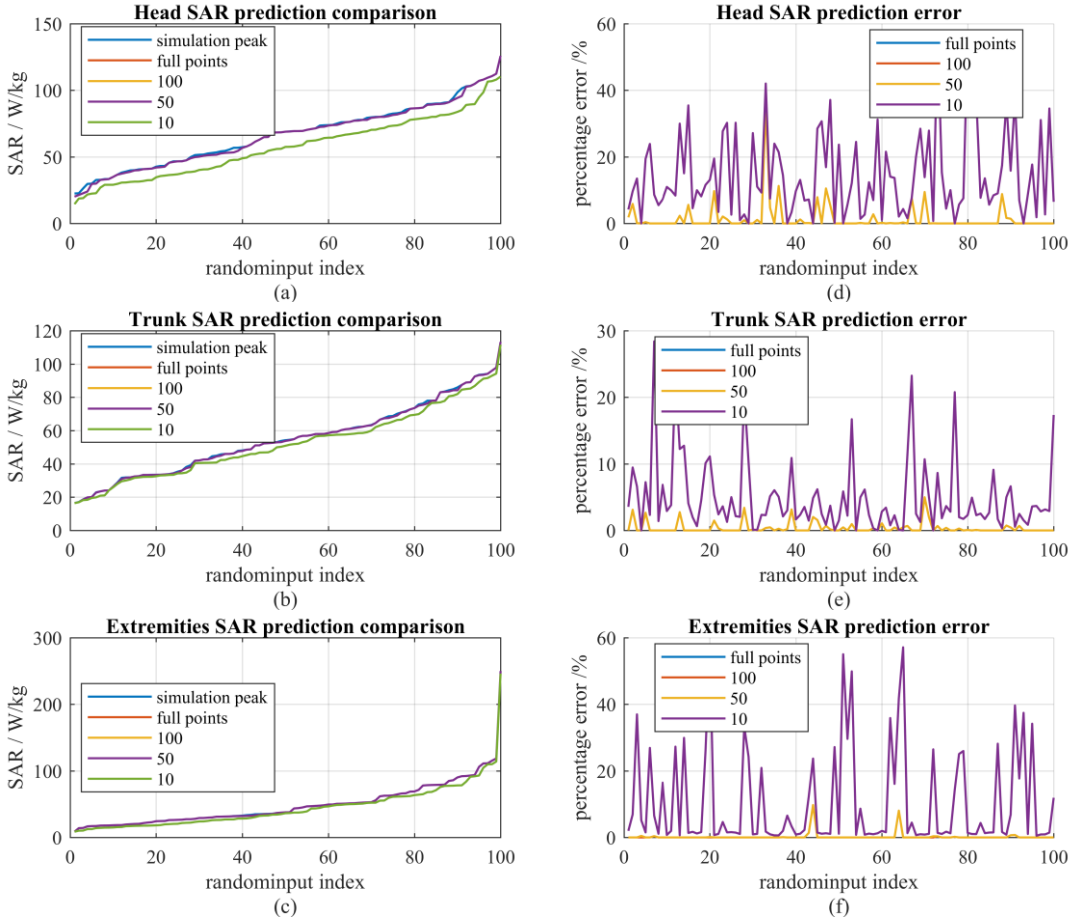

Figure 2-8. Prediction results of the clustering algorithm for duke head landmark.

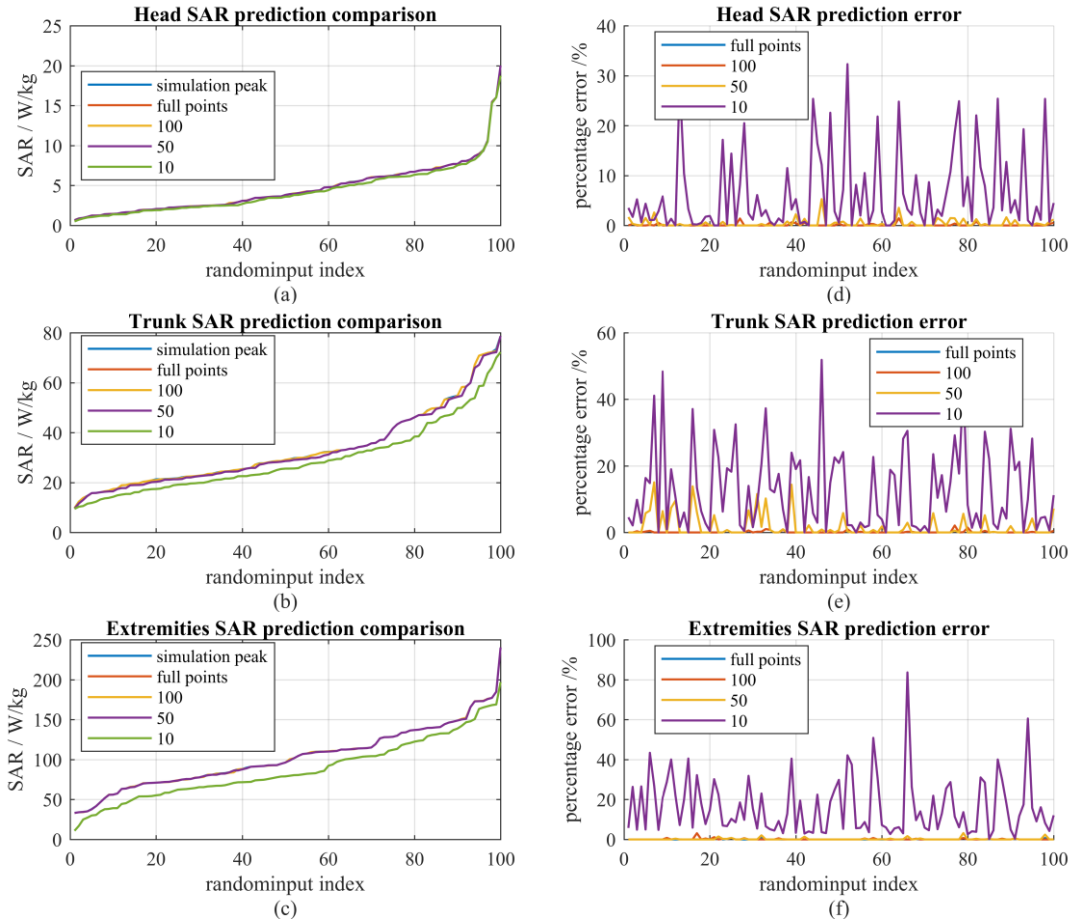

Figure 2-9. Prediction results of the clustering algorithm for duke trunk landmark.

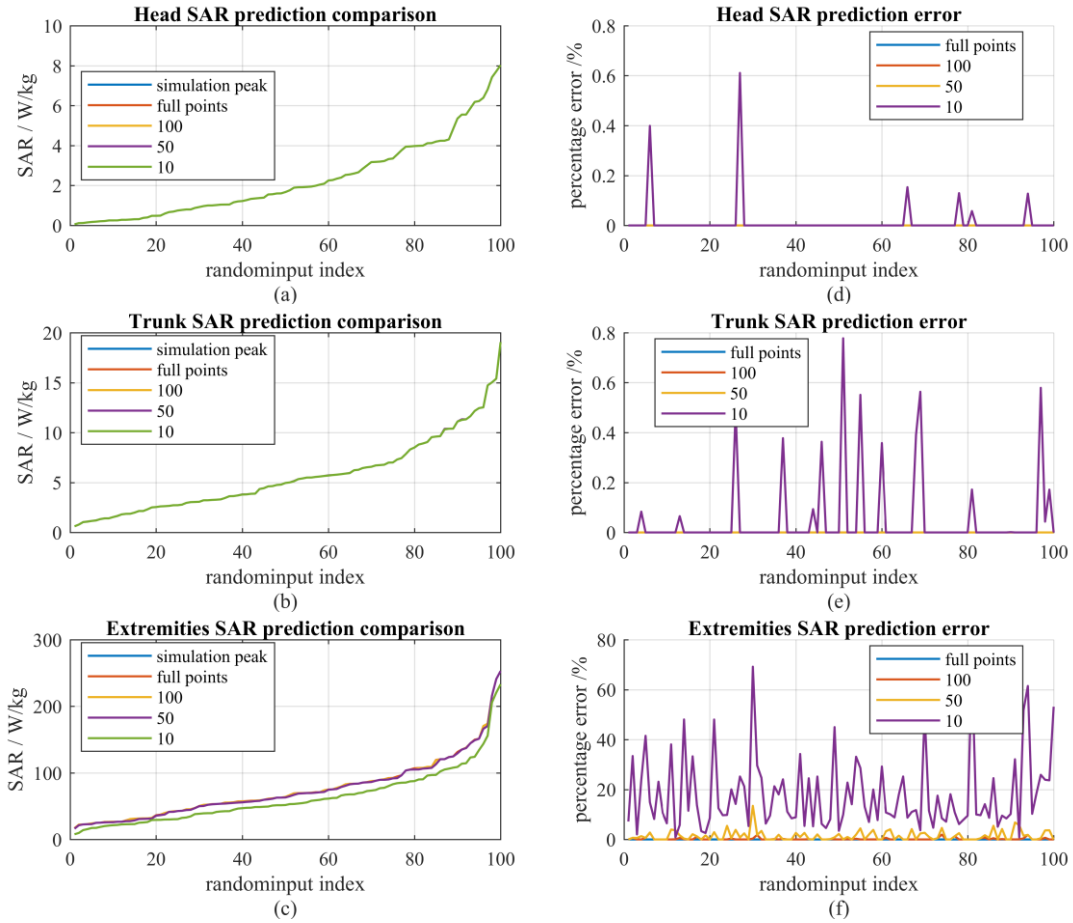

Figure 2-10. Prediction results of the clustering algorithm for duke ankle landmark.

2.4. **Discussion**

As shown in Fig. 2-5, the correlation coefficient for both training and testing data is larger than 99%, showing good network training results. As there are different requirements for SAR in head, trunk, and extremities region, here we also divide the body into three regions and predict the SAR separately (there are actually five physical regions, as the two arms and legs are separated physically, but as the SAR limitation is the same, we grouped these three regions to one). As shown in Fig. 2-6, the predicted SAR and the original SAR from the simulation have quite good agreement for all the three regions, the maximum error for all the cases is under 8%. When we increase the RF shimming range, the results are shown in Fig. 2-7, we can see we will need more

data to train the ANN, when then training data amount reaches 6000, the error will become stable, it means to get good performance we need at least 6000 training sets. AS shown in Fig. 2-8, Fig. 2-9 and Fig. 2-10, the clustering methods provides another way to predict the SAR level, given enough clustering groups number, this method provides even better results, but for too small clustering amount, the error will be too large as shown in the error for 10 locations in each region. Another important conclusion is that when a part of human body is moved out of the coil, the needed clusters for the SAR prediction will be much less compared with the exposure condition that such part is inside the coil.

One simple guess of why peak SAR will be only observed at some locations is that human body will have some tissues with quite different conductivity and permittivity, so we take the duke-trunk case and plotted the found possible peak SAR locations at the centre slice, the colour represents the human body tissue type while the red circles mark the possible peak SAR locations, as shown in Fig. 2-11, we can see that the possible peak SAR locations are limited at these interfaces between different tissues, or between human body and the air. And the further reason is when two different types of tissues are adjacent to each other, the vertical D field will be continuous and the dominant D component in MRI is the vertical part, as shown in Fig. 2-12, we simulated two inhomogeneous phantom with 3 section, with the permittivity of 10, 50 and 80 in case 1 and the conductivity of 0, 0.2 and 0.47 in case 2, as shown in the figure, the SAR will be higher at the interface of these sections.

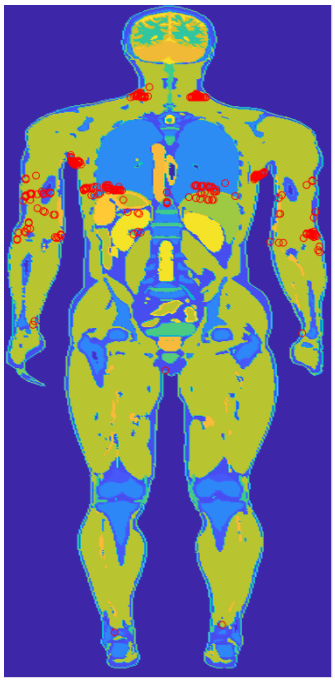

Figure 2-11. Possible peak SAR locations of human body.

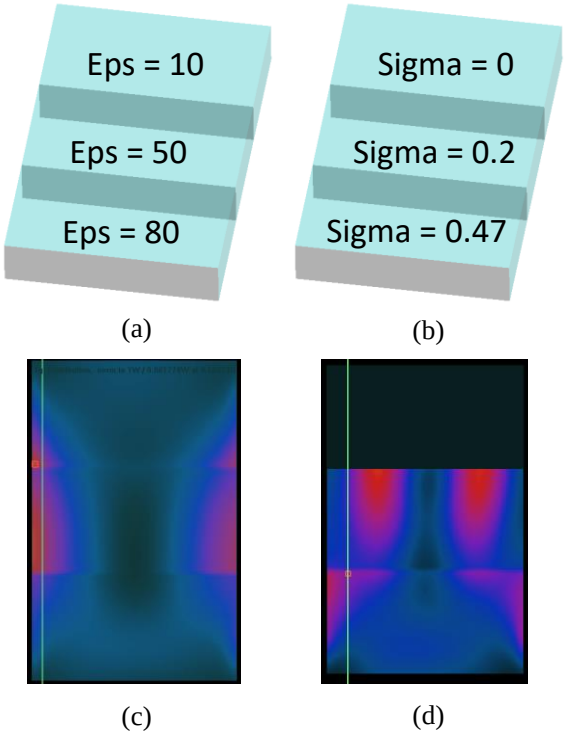

Figure 2-12. SAR distribution of inhomogeneous phantoms. (a) and (b) show the permittivity and conductivity distribution of case 1 and 2, while (c) and (d) show the SAR distribution of case 1 and 2.

2.5. **Conclusion**

In this paper, we proposed two method to combine Q matrix and clustering algorithm, also using ANN to predict the induced peak 10-g averaged SAR in human body under ultra-high field multi-channel MRI coil scanning, the predicted SAR from the method shows acceptable error compared with those from direct calculation of the whole-body region, and greatly reduced the computation resources and time needed, thus can be potentially used as a fast estimation method for the multi-input nonlinear SAR problem for ultra-high field MRI.

2.6. **Supplementary material: SAR star**

According to the IEC 62704 standard, the 10-g averaged SAR calculation should follow the certain standard, which divide the voxels into three groups, valid, used and unused, and for each group the 10-g averaged SAR follows different rules, as shown in Fig. 2-13.

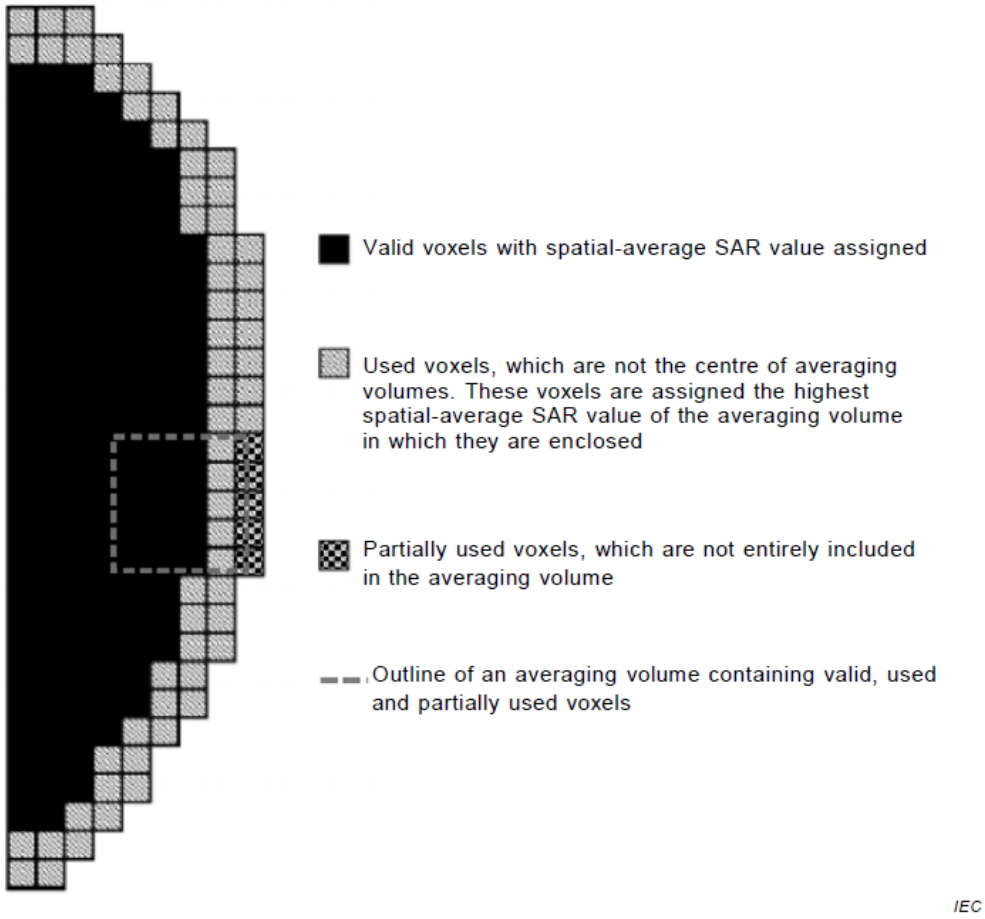

Figure 2-13. definition of the valid, used and unused voxels.

The whole process includes searching the 20-g region, confirming the status of the voxels and assigning the 10-g averaged SAR. The standard requires a 10-g average region to contain up to 10% of non-tissue volume to be valid, and those voxels which are not valid but included in the calculation of 10-g averaged SAR for a valid voxel to be ‘used’, and those neither valid nor used will be flagged as ‘unused’. For the valid voxels, the 10-g averaged SAR should be directly averaged in that region, for the used voxels, they will be assigned with the maximum 10-g averaged SAR value among those voxels for which they are included during the 10-averaged SAR calculation, and for the remaining unused voxels, the 10-g averaged will be one towards 6 directions

separately, and the assign the maximum value of these six to be the 10-g averaged SAR value of the unused value.

The flowchart of the averaged SAR calculation is shown as Fig. 2-14.

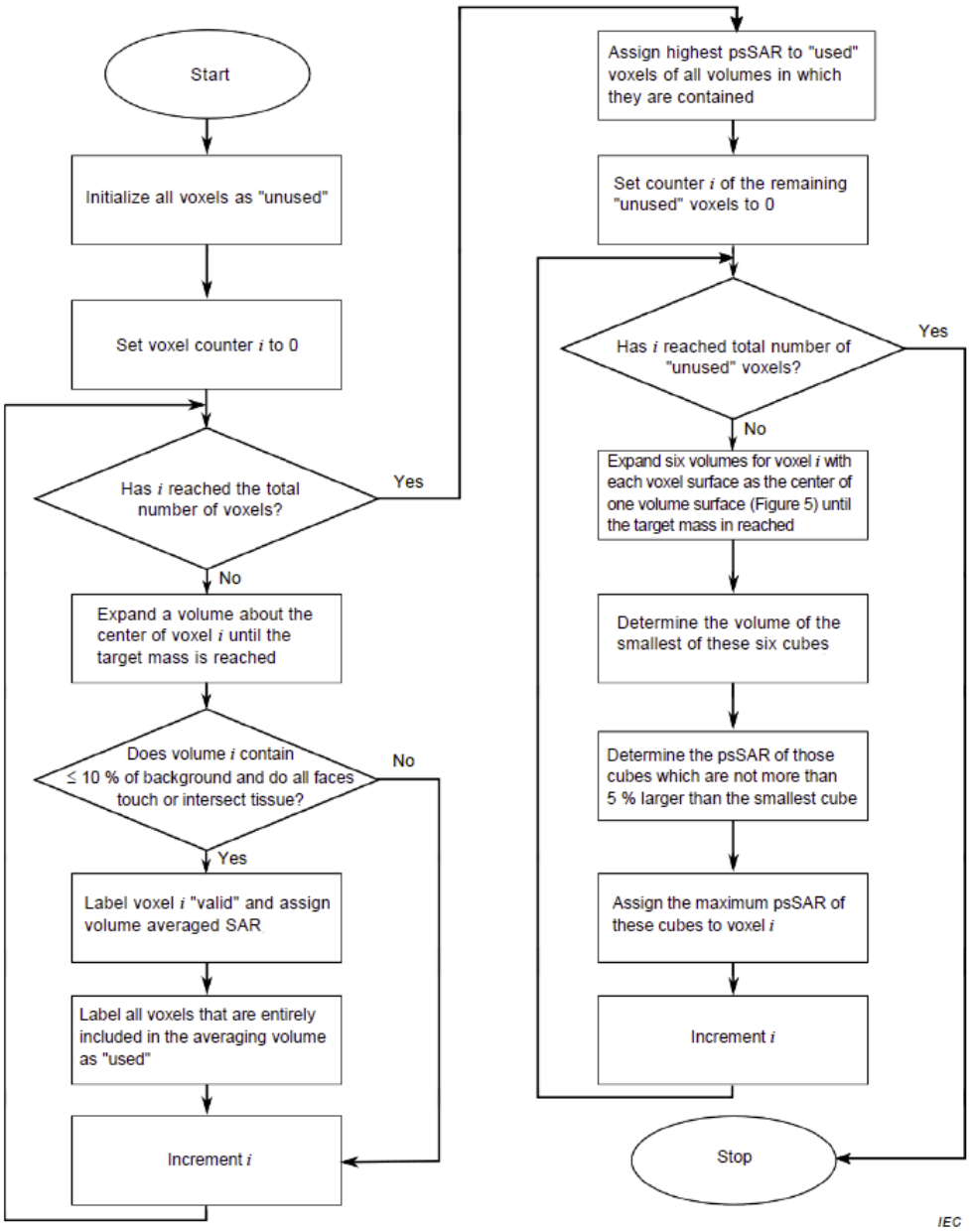

Figure 2-14. Flowchart of the SAR averaging algorithm from the IEC 62704 standard.

We followed the flowchart from the standard to calculate the SAR of the 'SAR star', as shown in Fig. 2-15, and comparison between the standard provided results and our results are shown in Fig. 2-16 and Fig. 2-17. As shown in the figures, the calculated

10-g and 1-g average SAR are in good agreement with the results provided by the standard. For the peak SAR value, the error is 3.72% for the 10-g averaged SAR and 3.68% for the 1-g averaged SAR, the mean error for each case is under 0.5%.

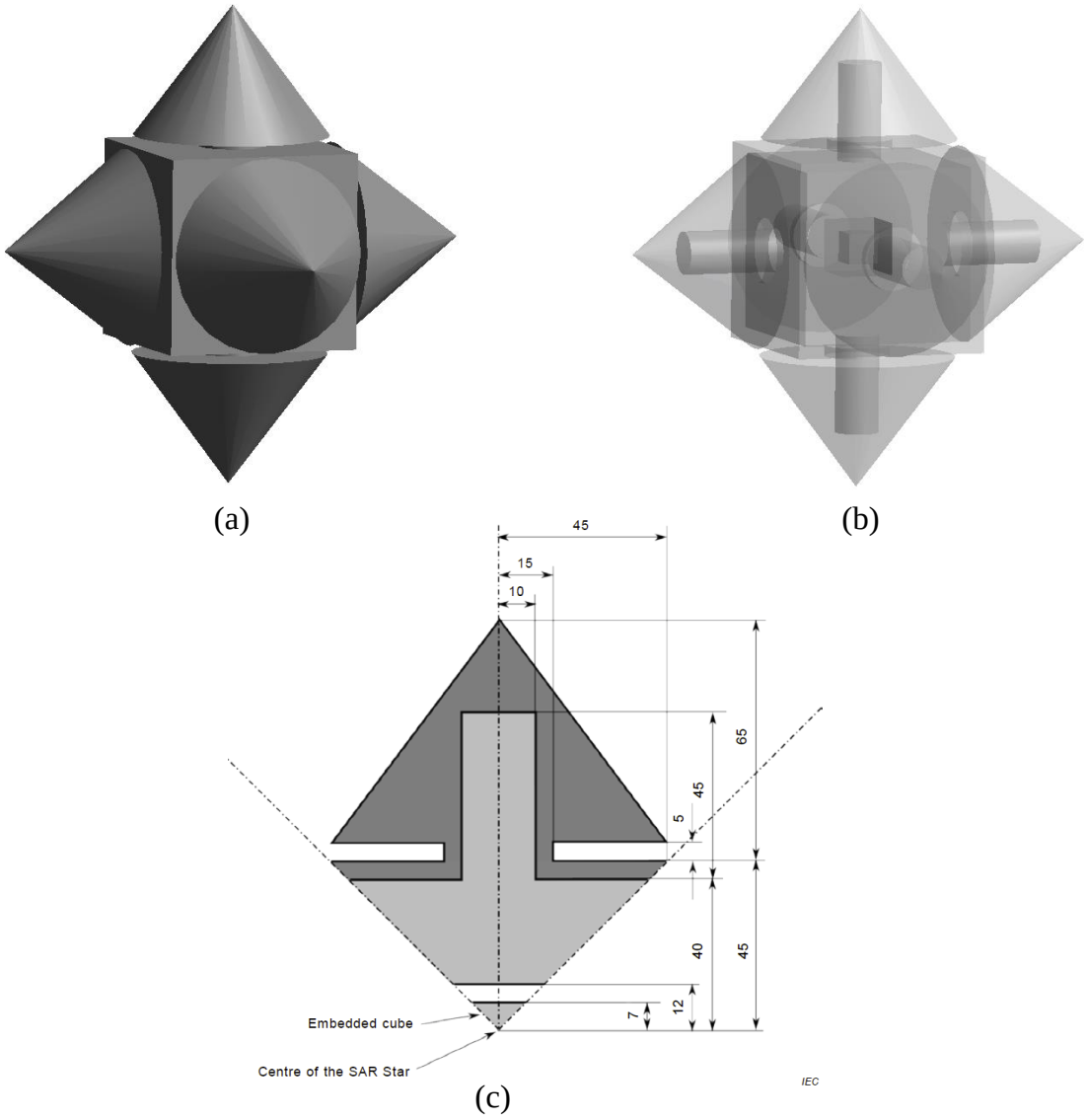

Figure 2-15. SAR star from the IEC 62704 standard. (a) is the outmost layer of the structure, and (b) is the transparent view of the star to show the inner structure. (c) shows the detailed dimension of the core, cube, and the outer layer of the star.

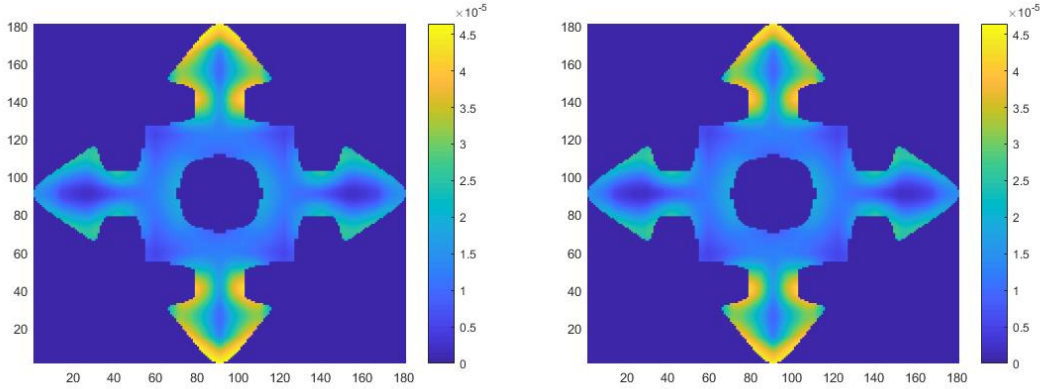

(a) (b)

Figure 2-16. 10-g averaged SAR on the center slice of (a) from generated code used for the SAR evaluation and (b) from the IEC 62704 standard.

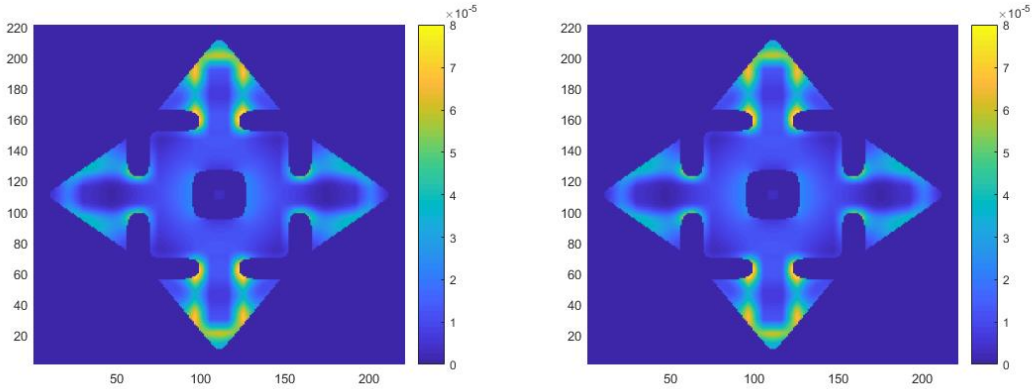

(a) (b)

Figure 2-17. 1-g averaged SAR on the center slice of (a) from generated code used for the SAR evaluation and (b) from the IEC 62704 standard.

Chapter 3. NOVEL RADIATOR DESIGN FOR MRI SAFETY ASSESSMENT OF IMPLANTABLE MEDICAL DEVICES

3.1. **Introduction**

Magnetic resonance imaging (MRI) is a widely used imaging method due to its non-invasive nature and high image quality. During the MRI procedure, radio frequency (RF) signals penetrate the human body and interact with the tissues [33],[34]. For patients with electrically conductive implantable medical devices (IMDs), the conductive parts will interact strongly with the electromagnetic (EM) fields and lead to localized RF energy deposition in tissues near the IMDs. There are numerous reports about patient burn incidents and influences on IMDs function caused by such highly concentrated power deposition [35]-[39]. Although direct in-vivo MRI RF-induced heating measurement methods can potentially be used for safety assessment [40],[41], in-vitro investigation of RF-induced heating and design optimization are still needed before the IMDs can be implanted as an MR Conditional device. Such MR Conditional devices allow the patient to safely undergo an MRI scan under very specific conditions. In many cases, the in-vitro measured heating data are directly used to label an IMD MR Conditional [42],[43].

Currently, performing RF-induced heating tests based on the ASTM standard requires a large sized RF coil for each frequency to be studied and a high-power supply system together with a large, shielded room. Such RF coils are available as part of MRI systems or equivalent test systems based on birdcage coils or TEM coils [44],[45]. Due to potential differences in coil types and coil sizes, local incident field calibration is

required [46]. Additionally, the linear variation of the E-field along the radial direction inside the ASTM phantom in a typical RF birdcage coil will limit the test region to achieve a high signal to noise ratio. The limited test region also requires accurate IMDs positioning systems to reduce experimental uncertainty [47].

Due to these limitations and with "*new knowledge about RF-induced heating related to the presence of an implant in a patient undergoing an MRI examination*", the new American Society of Testing and Materials (ASTM) *F2182-19e²* focusing on local exposure was developed [46]. The new *19e²* standard is "*focusing the analysis on local exposure, rather than whole-phantom calorimetry*" [48]-[51]. The in-vitro test is aimed to characterize the heating behaviour of the IMD family "*under the well-characterized incident field*", find the possible worst-case conditions, and then reasonably infer, or numerically predict, the RF-induced heating in actual in-vivo scenarios when an IMD is implanted inside a human body [46]. Furthermore, "*The phantom geometry has been further simplified and provided only as a possible example, allowing other geometries as well*" [46]. All these indicates that if one can develop a test system with well-characterized local exposure, it can also be used to assess the RF-induced heating for IMDs.

Since the test locations recommended in the ASTM standard suggests that the E-fields generated by the RF coil is mainly aligned with the bore direction, typically indicated as *z*-direction, the quantitative heating measurements essentially capture the interaction of the IMD with E-fields in this direction [52]-[55]. Therefore, efficient

in-vitro assessment of RF-induced heating requires a strong local E-field and a well-characterized background heating.

Various types of field generating equipment has been developed for, e.g., (i) electromagnetic compatibility (EMC) tests for active IMDs, (ii) open area test of electrically powered medical devices, and (iii) immunity testing of medical devices using wireless communications. A transmission line system (TLS) is recommended in the *ISO 11451-2* standard [56]. This TLS uses terminated transmission line elements to generate EM fields between the conductors and the shielded structures. However, the system requires a large chamber; additionally, the radiated fields have the risk of coupling with the chamber enclosure [57]. Another TLS based design has been proposed by McLean [58] to generate high-intensity EM fields over a wide frequency range, but the strength of the generated field changes dramatically in the test region. Groh et al. [59] reviewed other transmission line-based designs and suggested that open Transverse Electromagnetic (TEM) lines, like parallel plate guides, are faced with problems of radiation and coupling with the shielded room, while enclosed TEM lines, which have a closed structure and inside radiating elements, will make the experiments complex. The gigahertz TEM cell is also widely used in EMC tests, however, the variation of the field strength will be too large to perform stable heating measurements for IMDs [60]. For medical devices, the *ISO-10974* standard proposes a trough line resonator design. This device is designed to generate ultra-high fields for testing electrically short IMDs. However, the enclosed resonator structure requires a fixed length at the desired frequency, making it not suitable for a multi-frequency capable

system. Other antenna-based designs, including Bilog antennas, are able to generate a strong uniform field, but have the disadvantage of low power efficiency and require large chambers for operation [61].

In this paper we design, built, calibrate, test, and compare to the ASTM F2182 test method, a novel dual-frequency uniform E-field generator for 64MHz and 128MHz. For practical considerations, a high strength uniform E-field constrained to the inside of a rectangular box is desirable. The EM field in such a resonance structure can be characterized by transverse electric (TE) modes based on the cavity model [62].

In the proposed design, mixed TE modes of the rectangular resonator are used to generate a uniform E-field at 64 MHz and 128 MHz The dimensions of the E-field generator are chosen as a trade-off between (i) field homogeneity for dual-frequency capability, (ii) power efficiency, and (iii) sufficient space to test typical IMDs. The dual-frequency-in-one design requires lumped elements circuits to match the resonator at varying frequencies. Compared to the ASTM standard test system, using the ASTM phantom driven by an RF coil, the new design has the advantage of low cost, less sensitivity to IMD positioning error, ease of fabrication and operation, and most importantly, integration of both 1.5T and 3T RF-induced heating tests into one single system.

The remainder of the paper is organized as follows: Section II presents the design and development of the novel E-field generator, including (i) numerical simulations, (ii) experimental validation, and (iii) system calibration at 64MHz and 128MHz. Section III provides numerical simulation results of the RF-induced heating for two

IMD families and positioning error analysis on a selection of IMDs. RF-induced heating measurements on a selection of IMDs were performed in the E-field generator and the ASTM phantom and compared to each other in Section IV. Section V provides the discussion and section VI presents the conclusions.

3.2. **Multi-frequency E-field generator**

3.2.1. **Design of the Multi-frequency E-field generator**

There are several key requirements that need to be met to accomplish reliable and efficient measurements. 1) to meet the ASTM RF-induced heating test requirements, the E-field generator needs to generate a sufficiently high E-field along the longitudinal direction of the transverse plane (z-direction) similar to that at the test location inside the ASTM phantom; 2) generate a uniform E-field to minimize the positioning error, 3) be accessible from the top so that the test devices can be accurately positioned and inspected, and 4) be large enough to accommodate IMDs of typical sizes used in clinical settings.

A rectangular shaped box, shown in Fig. 3-1, was developed for this study. The central region of this box is then filled with gelled saline. As prescribed in the ASTM standard, the gelled saline should have a relative permittivity of 78 and an electrical conductivity of 0.47 S/m. The corresponding wavelengths for 1.5 T and 3T systems are around 45 cm and 22 cm, respectively. By attaching copper-clad, flexible circuit boards with excitations to the sidewalls of the box, a cavity can be formed if appropriate cavity modes treat the top/bottom surfaces as perfect magnetic conductors. The top side of the

gel box is open. To generate a uniform E-field along one direction of the transverse plane (*x*-*z* plane), the TE_{10} mode is utilized for 64 MHz the dimension of 300 mm by 300 mm is chosen along the *x*- and *z*-directions so that the resonance frequency of the TE_{10} mode is around 64 MHz and there will be enough space to place typical IMDs. As the frequency of the 3 T MRI increases to 128 MHz, high order modes, such as the TE_{20} and TE_{12} modes will have noticeable strength.

To minimize the influence of these high order modes, several methods are used. First, the dimensions of 300 mm by 300 mm are chosen to suppress the higher modes, and second, a special 4-way feeding network is developed. Four gaps are cut on the left and right walls near the four corners of the box. SMA connectors are connected to the gaps to form even and differential excitations between the front (+*z*) and back (-*z*) box walls, as shown in Fig 3-1. Two gaps on the cavity's front and back walls are cut for decoupling the left (-*x*) and right (+*x*) channels. Such a feeding network ensures that only modes with major E-field components along the *z*-direction can be excited and the E-field of those modes will be symmetric with respect to both the *x*-axis and *z*-axis.

Fig. 3-1 (b) illustrates the schematic of the system. The signal from a signal generator is amplified using a power amplifier (ZHL-100W-52-S+ from Mini-Circuits) supplied with a direct current (DC) power source. The RF signal travels through the power divider into a lumped element matching circuit ('L' type). The output signals of a four-way power divider (H4S-0.252WWP from Meca Electronics) with the same magnitude and phase are connected to SMA connectors attached on the wall using coaxial cables. A special four-way feeding network is acquired by exciting the front

(+z) and back (-z) walls differentially as shown in Fig. 3-1 (b). The front (+z) copper plates are connected to the outer conductor of the SMA connector, while the copper plates on the back (-z) wall are connected to the inner conductor of the SMA connector.

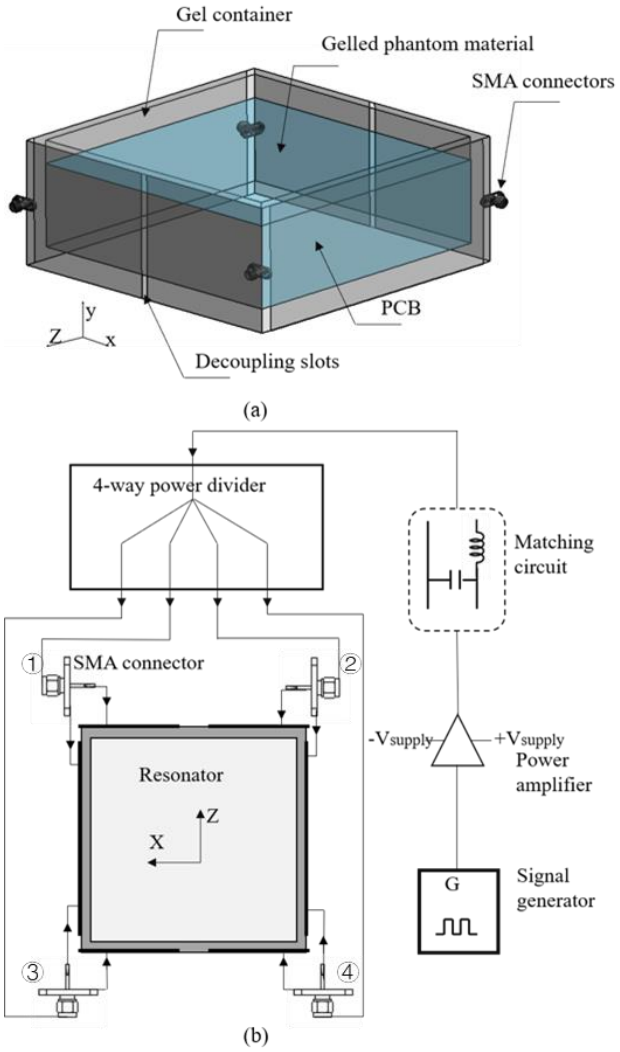

Figure 3-1. (a): E-field generator design, (b): system illustration.

Full-wave numerical simulations are performed to assistant the design. Such electromagnetic simulations were performed using the commercial FDTD software SEMCAD X (ZMT, Zurich, Switzerland). Copper plates on the acrylic box are modelled as perfect electric conductor (PEC) on a dielectric box with a relative permittivity of 2.25 and an electrical conductivity of 0 S/m). The copper plates are modelled as ideal PEC with no thickness, the wall of the acrylic box is 12.5 mm thick,

and the box outer dimensions are 300 mm by 300 mm by 120 mm. The SMA excitations are modelled as lumped sources, the gelled saline is modelled as a lossy dielectric material (relative permittivity = 78, electrical conductivity = 0.47 S/m), the height of the gel is 90 mm, and the grid resolution of the simulation is 2.0 mm.

The matching circuit is modelled as lumped elements in series with the sources. Broadband simulations were performed to match the resonator at 64 MHz and 128 MHz for the 1.5 T and 3 T MRI systems. As shown in Fig 3-2, we observed that the S_{11} values were below -10 dB, and the S_{21} values were below -15 dB. The numbering of the ports is shown in Fig 3-1. The reflection and coupling of other ports are not shown since the structure is symmetric.

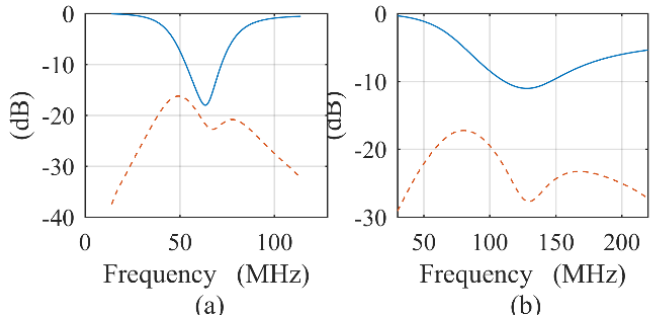

Figure 3-2. S parameters of the E-field generator for (a) 1.5 T (64 M Hz) and (b) 3 T (128 MHz). Blue solid line for S11, red dotted line for S21.

Based on the designed structure, electromagnetic simulations were performed for the two frequencies and the E-field distributions are shown in Fig. 3-3. The input power in the simulations is normalized to 32.52 W at 64 MHz and 13.77 W at 128 MHz respectively, so that the induced E-field in the generator will be equivalent to the E-field at the test in a standard ASTM phantom location (around111 V/m (64 MHz) and 91 V/m (128 MHz)) when the whole-body averaged phantom SAR is normalized to 2 W/kg.

As shown in Fig. 3-3, for 1.5 T (64 MHz), the E-field distribution is similar to that of a TE_{10} mode, whereas for 3 T (128 MHz), the E-field distribution is similar to a combination of a TE_{10} and a TE_{21} modes. However, in both cases relatively uniform E-field distribution can be achieved in the centre on the E-field generator.

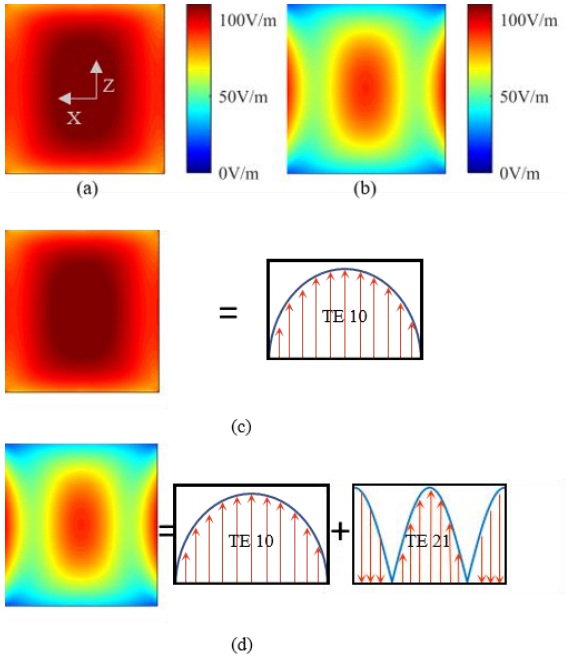

Figure 3-3. Electric field distribution at the center slice of gel based on numerical simulation. (a) The electric field along the z-direction solved using the numerical method for 64 MHz, and (b) for 128 MHz, (c) single mode at 64 MHz (d) hybrid modes of 3 T.

The Q factor is assessed based on the stored energy and the consumed energy per period, the comparisons of the results and those from the analytical calculation are shown in Table 1. The main loss of the system is due to the power dissipation in the gel, the major contribution of the Q factor is from conductivity loss by

$$Q_d = \frac{1}{\tan\delta} \tag{3-1}$$

and

$$\tan\delta \approx \frac{\sigma}{\omega * \varepsilon_0 \varepsilon_r}, \tag{3-2}$$

where σ is the electrical conductivity of phantom material ($\sigma = 0.47\mathrm{S/m}$), ω is the angular frequency ($\omega = 2 * \pi * 64\ \mathrm{MHz}$ for 1.5T; $\omega = 2 * \pi * 128\ \mathrm{MHz}$ for 3T), ε_0 is the vacuum permittivity, ε_r is the permittivity of the gel ($\varepsilon_r = 78$).

The Q factor (Q_s) can be obtained by

$$Q_s = \frac{\omega_0' U}{P_d^{ave}}, \tag{3-3}$$

where U is the stored energy, P_d^{ave} is the averaged power dissipated, and ω_0' is the real angular frequency.

Table 3-I. Q factors comparison

	Dielectric loss/W	Frequency/MHz	Stored energy/J	$Q_{simulation}$	$Q_{theoretical}$
64MHz	32.34	64	5.41e-8	0.67	0.61
128MHz	13.64	128	2.24e-8	1.32	1.17

3.2.2. **Experimental validation of the design**

To experimentally validate the E-field distributions inside the generator an E-field probe (Easy4MRI, ZMT, Zurich, Switzerland) was placed inside the generator at 49 locations (at the vertical center slice of the gel) as shown in Fig 3-4. These 49 positions were chosen with a step size of 25 mm along the *x* and *z*-direction. The E-field generator was filled with 90 mm gel and the E-field probe was placed 45 mm under the gel surface.

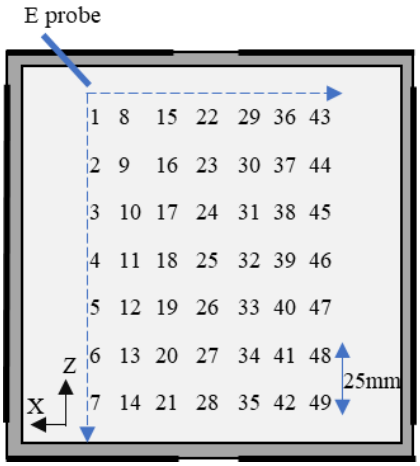

Figure 3-4. Experimental validation of the E-field distribution using an E-field probe at different locations of the generator.

Comparisons of the E-fields obtained by direct measurement and simulation are shown in Fig. 3-5. All results shown here are for a net input power of 32.5 W for 64 MHz and 13.8 W for 128 MHz. Using this power levels, the E-field at the centre of the generator will be similar to those at the ASTM recommended device testing location when a whole-body averaged phantom SAR of 2 W/kg is used. In the simulation the input power is calculated using the S parameter from the source sensors; the measurements are calibrated using the calorimetry method as suggested in [46],[48]. As clearly shown in Fig. 3-4, the results obtained by experimental measurements were in good agreement with those from simulations for both the 1.5 T (Fig. 3-3 (a)) and 3 T (Fig. 3-3 (b)) systems. Such results validated our design.

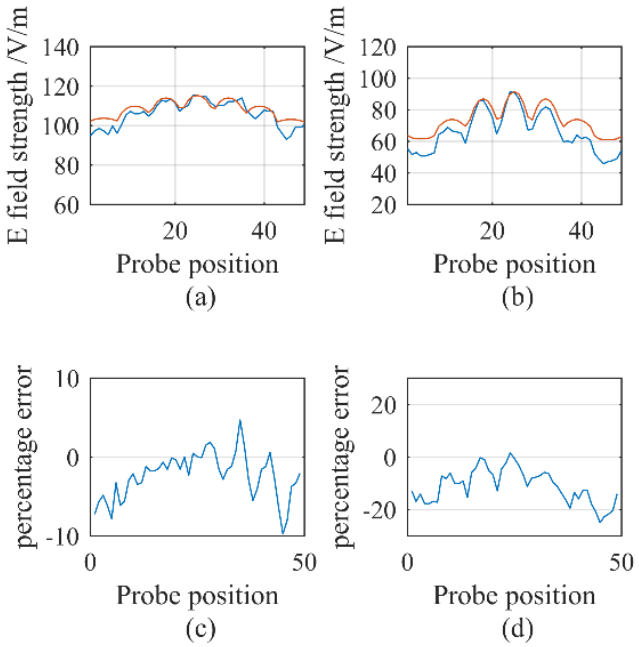

Figure 3-5. Comparison of measured and calculated E-field inside the generator at 49 locations. (a) E-field at 64 MHz, (b) E-field at 128 MHz, the blue lines in (a) and (b) are the simulation and the red lines are the experimental results, (c) and (d) show the relative errors for 64 MHz and 128 MHz field.

3.2.3. **Calibrations of the dual-frequency E-field generator**

Two calibration procedures should be used to ensure the local E-field in the generator will be similar to those in the ASTM phantom. The first calibration procedure is referred to as the input power calibration which follows the calorimetry procedure described in [46],[48]. The second calibration procedure follows the procedure of local exposure estimation based on [46].

For the input power calibration, we performed the following steps:

1. Fill the E-field generator with 90mm saline (not gelled) with a relative permittivity of 78, an electrical conductivity of 0.47 S/m, and a weight of 6.85 kg.
2. Cover the E-field generator with a thermal insulation lid to avoid evaporation and cooling of the saline which can produce a measurement error; leave the lid on the top of the E-field generator.
3. Measure the temperature at the centre of the saline using a fibre probe until the temperature is stable (variation less than ±0.5°C).
4. Cover the entire system with thermal insulation material and apply the power for 900s.
5. Stop the power input, quickly stir the saline, measure the saline temperature rise with fibre probe.
6. Calculate the total deposited power in the saline by

$$P = c * m * \frac{\Delta T}{\Delta t}, \tag{3-4}$$

where c is the specific heating capacity of the saline, c = 4150 J/kg/K, m is the mass of the saline, which is 6.85 kg, ΔT is the temperature rise of the saline, Δt is the heating time which is 900 s.

Based on the procedure described above, one can generate the required power following the calibration curve as shown in Fig. 3-6. As shown in the figure, the target deposition power inside the phantom should have corresponding temperature rises around 1.03 °C at 64MHz and 0.45 °C at 128 MHz to generate an incident E-field of 111 V/m at 64 MHz and 91 V/m at 128 MHz.

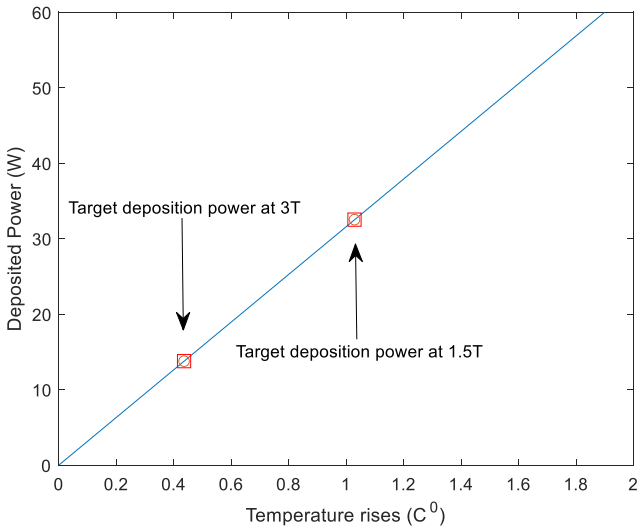

Figure 3-6. Calibration curve to estimate the input power based on calorimetry method.

In addition, a local exposure calibration should also be performed per [46] using a 3.2 mm x 10 cm titanium-alloy rod. Due to potential signal source drift and power amplifier variation between each experiment, the incident E-field at the centre location of the generator can have slight variation. These variations should be captured through local exposure measurements. Therefore, before each device measurement, a five-step local energy calibration procedure as described in [46] should be performed. In the test, the gelled saline should be used to fill the E-field generator to 90mm. Temperature rises

for 6 minutes are measured near both ends of the titanium-alloy rod. The local SAR estimations (in terms of W/kg) should be estimated by $\Delta T_{360}/1.3$ at 64 MHz and $\Delta T_{360}/1.45$ at 128 MHz.

3.3. **Numerical Studies of RF-Induced Heating for IMDs**

To show the equivalency of the RF-induced heating measurement between the E-field generator and the ASTM standard test system, two sets of IMDs were placed inside the E-field generator and the ASTM phantom (driven by an MRI RF coil). For the purpose of comparison, the 1g averaged specific absorption rate (SAR) was assessed [63]. During the RF-induced heating measurements in the E-field generator, the IMDs were placed at the center of the E-field generator, with the long axis of all devices aligned with the *z* direction.

The two device families used in this investigation are shown in Fig. 3-7. The first IMD family consists of fully threaded compression screws of different lengths and diameters. The second IMD family consists of plates and screws from a typical trauma product. Nine plates with different dimensions were loaded with different numbers of screws.

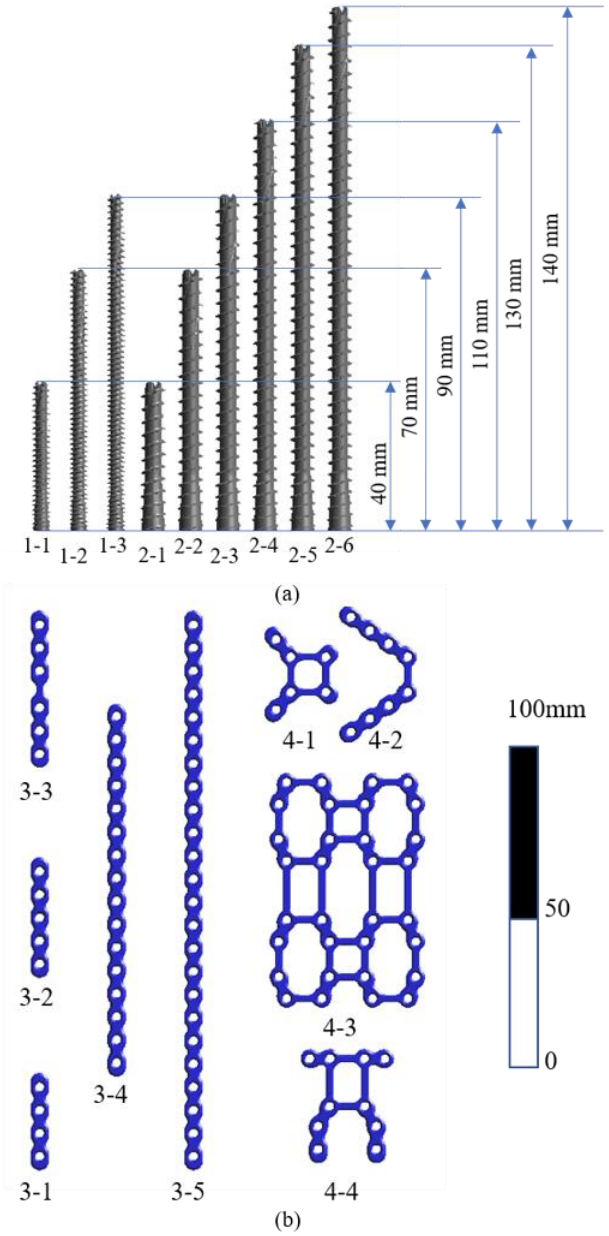

Figure 3-7. Simulation models of (a) standalone screws and (b) plate system family.

We studied the RF-induced heating of these devices when they were placed inside the E-field generator and the ASTM phantom. Both the E-field generator and the ASTM phantom were filled with 90 mm of gelled saline. During the RF-induced heating in the E-field generator, the devices were placed at the center of the E-field generator. In all studies using the ASTM phantom, the devices were placed at the center of *y*- and *z*-axis and 20 mm from the left (-*x*) edge of the ASTM phantom where a high

electric field strength can be found [47]. In all the simulations, the IMDs are modeled as PECs, with a grid resolution of 0.5 mm.

In the RF-induced heating measurements using the ASTM phantom and an RF coil, the MRI RF coils were the MITS 1.5 T system (ZMT, Zurich, Switzerland) and a standard commercial 3 T RF coil. The dimensions of these coils are given in Table 3-II. In addition, two generic coil models were also used in the simulations. The simplified generic coils models were referred to as H8 coils [64]. They have hard current excitations on the legs of the coils. By varying the phase of those sources, the circular polarized (CP) mode can be generated. The dimensions of all physical and generic coils are shown in Table 3-II.

Table 3-II. Dimensions of the Coils Used in the Simulation

	1.5 T Physical	3 T Physical	1.5 T Generic	3 T Generic
Coil radius (mm)	350	305	315	315
Coil length (mm)	650	550	650	650
Shielding length (mm)	425	320	N/A	N/A
Shielding length (mm)	850	1450	N/A	N/A
Number of legs	16	16	8	8
Excitation type	IQ	IQ	H8	H8

An illustration of those coils is shown in Fig. 3-8 (a) and (b). The comparisons of simulation results for RF-induced energy near the devices is shown in Fig. 3-9, and all the SAR values shown in the tables and figures were spatially averaged over a mass of one gram (1 g). The input power of the ASTM system is normalized to a whole-body averaged SAR of 2 W/kg. Results obtained from the E-field generator were calibrated to the incident E-field at the device test location inside the ASTM phantom. As clearly

shown in Fig. 3-9, the E-field generator can produce similar energy deposition near the devices as those produced in the standard ASTM phantom.

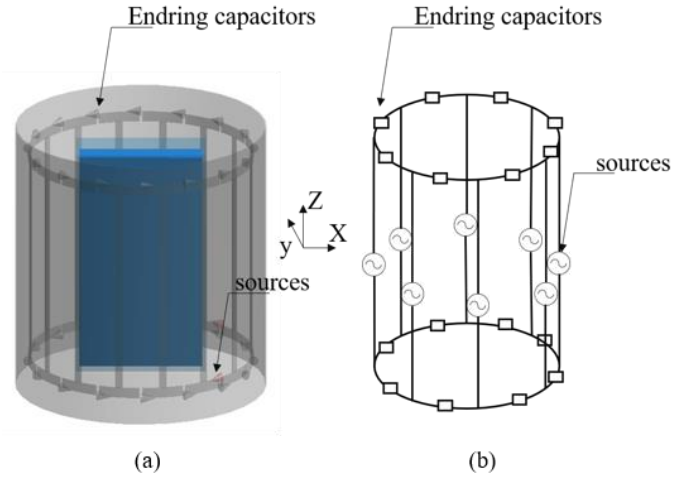

Figure 3-8. (a) Typical bird cage coil used for MRI scanning (b) simplified generic coil H8 (hybrid 8-port generic coil).

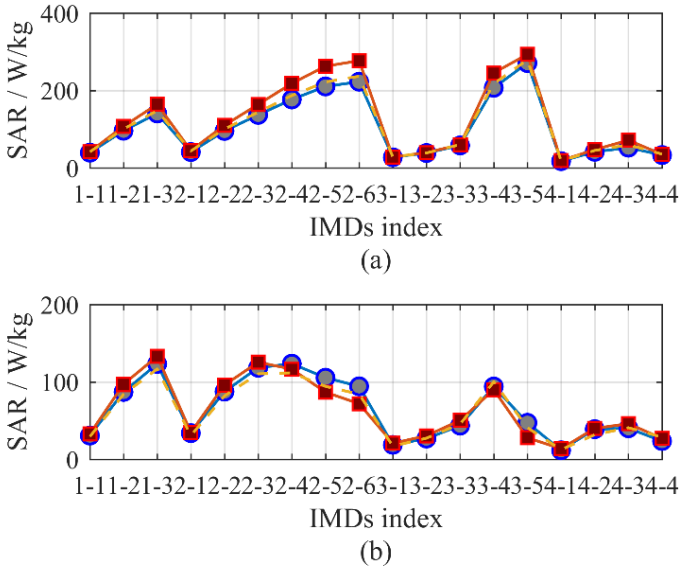

Figure 3-9. Comparison of 1g averaged SAR values in simulation for (a) screw and plate for the 1.5 T MRI, (b) screw and plate for the 3 T MRI, the blue line is for the ASTM standard test, red solid line is for the E-field generator, and the dashed is for the ASTM standard test.

A sensitivity analysis was then performed to understand the impact the device positioning error has on the energy deposition near the IMDs for both the ASTM method and the E-field generator. For the worst-case heating IMDs from each family, the IMDs are moved away from the centre -10 mm, -5 mm, 5 mm and +10 mm along

the *x*, *y*, and *z* axes. EM simulations were performed for the E-field generator and the ASTM phantom. Fig. 3-10 shows the results for screw 2-6 at 64 MHz and screw 1-3 at 128 MHz. Fig. 3-11 shows the results for plate 3-5 at 64 MHz and plate 3-4 at 128 MHz. As we can clearly see from these data, the newly designed E-field generator has similar sensitivity of the device positioning error along the *z*-direction as the ASTM phantom. However, the device positioning errors in the E-field generator along the *x*- and *y*-directions are much smaller than in the ASTM phantom. Overall, the E-field generator clearly outperforms the ASTM phantom in measurement uncertainty, power consumption, simplicity, size, and price.

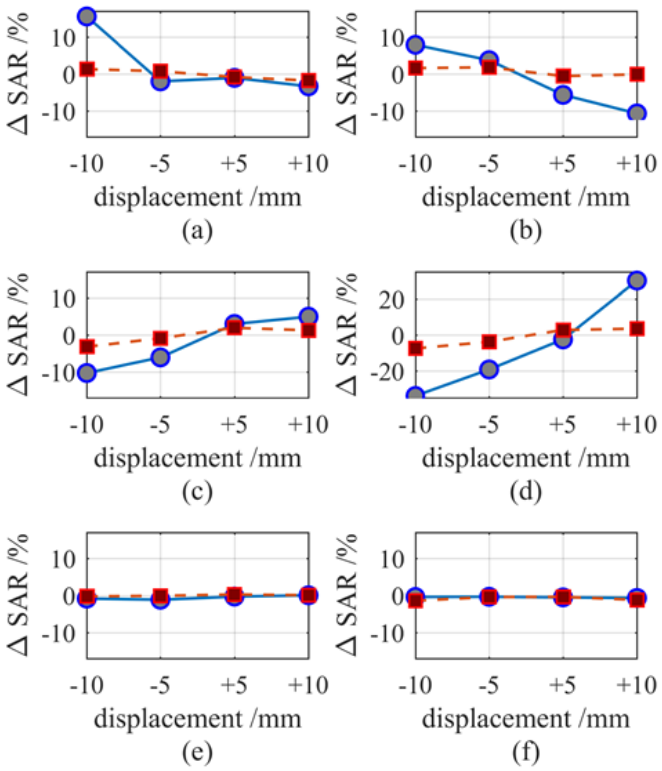

Figure 3-10. SAR sensitivity of the screw family with respect to positioning error along (a)(b) the x-direction at 64 MHZ and 128 MHz, (c)(d) for y-direction, (e)(f) for z-direction. The solid blue line indicates data in the ASTM phantom, while the dashed red line indicates data for the E-field generator.

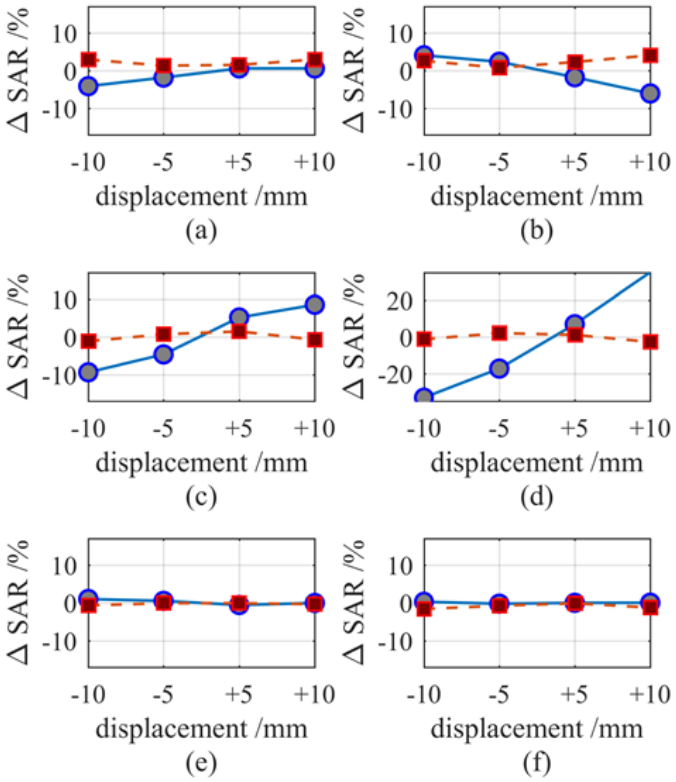

Figure 3-11. SAR sensitivity of the plates system with respect to positioning error along (a)(b) the x-direction at 64 MHZ and 128 MHz, (c)(d) for y-direction, (e)(f) for z-direction. The solid blue line indicates data in the ASTM phantom, while the dashed red line indicates data for the E-field generator.

3.4. **Experimental Validation of Temperature rises**

Based on the design presented above, a prototype of the E-field generator was developed as shown in Fig. 3-12. IMDs were placed inside this test generator and the RF-induced heating was measured. In all measurements, the temperature probes were placed at the maximum heating location based on the modelling results. For comparison, thermal simulations were also obtained using Pennes' bioheat based thermal solver in SEMCAD X. In both modelling and measurement, the RF power was turned on for 15 minutes. Temperature rises in both modelling and measurements are shown in Table 3-III. All results are normalized a whole-body averaged SAR of 2 W/kg

for the ASTM phantom. For the E-field generator, the input power is chosen to generate an equivalent E-field. In both settings, the incident E-field at the device test location was 111 V/m 64MHz and 91 V/m at 128MHz.

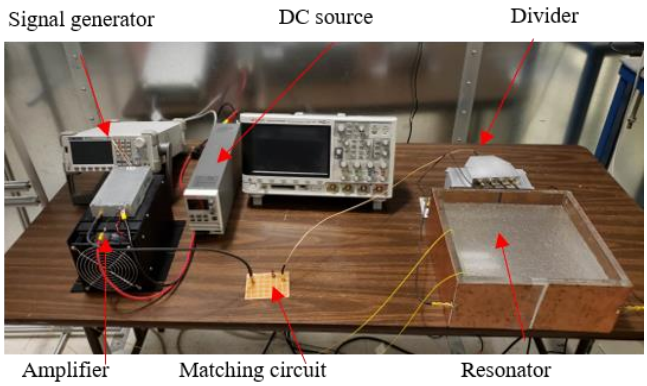

Figure 3-12. Experimental setup for the E-field generator validation.

Table 3-III. Comparison of Measured and Simulated Temperature Rises for both 1.5 T and 3 T.

1.5 T (64 MHz)	E-field generator			ASTM phantom		
Part Number	Modeling ΔT/°C	Measured ΔT/°C	Difference /%	Modeling ΔT/°C	Measured ΔT/°C	Difference /%
1-3	9.85	8.55	15.21	7.96	8.19	-2.76
2-4	11.96	11.13	7.48	9.38	9.34	0.48
2-6	15.36	15.22	0.91	11.8	10.79	9.37
3-4	14.08	13.01	8.23	11.8	10.10	16.86
3-5	16.68	15.24	9.41	15.3	12.60	21.42

3 T (128 MHz)	E-field generator			ASTM phantom		
Part Number	Modeling ΔT/°C	Measured ΔT/°C	Difference /%	Modeling ΔT/°C	Measured ΔT/°C	Difference /%
1-3	7.76	6.73	15.29	7.22	7.86	-8.14
2-4	6.33	5.58	13.38	6.58	6.55	0.48
2-6	4.05	3.27	23.88	4.66	3.95	18.03
3-4	5.21	4.59	13.43	5.43	6.98	-22.19
3-5	1.82	1.70	7.06	2.97	2.60	14.23

3.5. **Discussion**

From the results presented in Fig. 3-9 we can see that the induced SAR for most devices in the two IMD families at both 64 MHz and 128 MHz show a good agreement between the two different test systems. However, relatively large differences were observed for the longer devices 2-6, 3-4, and 3-5 at 64MHz as shown in the numerical simulations (Fig. 3-9) and the experimental experiments (Table 3-III). Such relatively large differences are due to the E-field variations along the *z*-direction, as well as the potential interaction between the IMD and the E-field generator. In the ASTM phantom the E-field along the *z*-direction has a better uniformity than in the E-field generator since the E-field generator uses higher order modes. To achieve better agreement between the E-field generator and the ASTM phantom, the *z*-direction of the E-field generator can be extended which will lead to a better E-field uniformity. Currently, the RF-induced heating of the 10 cm titanium rod is used to calibrate the local exposure. Using this calibration method, we find that for an IMD with a maximum length of less than 15 cm, the results obtained in the ASTM phantom and the E-field generator agree very well with each other. This agrees with the ASTM standard requirement that a 15 cm uniform incident E-field should be generated. Alternatively, one can develop better calibration parameters so that the averaged E-field along the *z*-direction is considered as a function of device length. Using this calibration, a better agreement can be achieved. However, this is beyond the current calibration procedure described in the ASTM standard.

From the results shown in Fig. 3-10 and 11, we can see that the IMD positioning error along the z-direction would lead to negligible RF-induced heating differences. However, such differences can be magnified for positioning errors along the *x*-and *y*-directions in the ASTM phantom. As clearly indicated in the figures, a positioning error of 5 mm along the *x*- or *y*-direction in the ASTM phantom, can change the induced SAR by 15%. Such variation can increase to 30% with a 10 mm positioning error along with these two directions. However, such a positioning error has almost no impact on the RF-induced heating when the E-field generator is used. The newly designed system can provide more consistent measurement results since the heating measurement is not very sensitive to the positioning error along all three directions. Based on these observations and a current side length of 30 cm, we observe that when the IMD overall length is less than ½ of the incident field wavelength, all results from measurement and modelling inside the ASTM phantom and the E-field generator agree well with each other.

Apart from the advantage of the measurement stability, the novel uniform E-field generator integrates both 1.5 T and 3 T testing into a single system without the need of an RF coil. In addition, using clinical, or clinically equivalent, MRI RF coils would require a large shielding room, a high-power amplifier, and a large footprint for the equipment. The novel uniform E-field generator has much smaller dimensions and requires less than 100W input power. This allows the E-field generator to become a desktop test system and an extremely useful alternative for IMDs MRI RF-induced heating measurements.

A basic description of AIMD induced heating and voltage estimation is introduced in this chapter.

3.6. **Conclusion**

In this paper we present a novel design of a uniform E-field generator. The design was guided by the cavity model and validated using numerical methods. Experimental validations of the design were performed by measuring the E-field distribution within the generator and compare it to simulation results. Two sets of IMD families were placed inside the E-field generator and the ASTM phantom for both modelling and measurement studies. From these studies, we observed highly correlated results for both frequencies 64 MHz and 128 MHz. In addition, the measured RF-induced heating is less sensitive to device positioning errors in the E-field generator. Compared to the conventional ASTM method using an RF coil and the ASTM phantom for testing, this novel E-field generator has a significant advantage in terms of low cost, low operation power, ease of operation, and most importantly, integration of 1.5 T and 3 T RF heating tests into a single desk-top system. This provides us with a better alternative to evaluate the RF-induced heating of IMDs under MRI exposure. It is observed that when the device length is less than ½ of the incident field wavelength, all results from measurement and modelling inside the ASTM phantom and the E-field generator agree within the combined uncertainty of 25%.

A basic description of AIMD induced heating and voltage estimation is introduced in this chapter.

3.7. **Extended field generator design**

From the results presented in part 3 and 4, we can see there are still at least two ways to improve the design of the uniform field generator. First, the field homogeneity can be future improved, which helps to increase the test area, and improve the stability as the field variation can be improved. Secondly, once the field homogeneity can be improved, we can further increase the size of the field generator, so that it can accommodate devices like lung pacers, deep brain stimulators with longer leads, and lager passive devices like artificial knees, spinal stents. As well known in EM theory, the field distribution in a cavity is the superposition of many resonant modes, and the larger the cavity is, the more modes will be supported inside, generally. And to design the cavity so that we can get only the modes we need, there are two things we can do, increase the number of excitations and adjust the excitation positions.

For the current design presented in part 2, there are 2 pairs of differential excitations, so in each pair of the differential excitations, the two ports from the power divider actually serve the same function, if we move the excitations to the center of the bottom, we can actually double the excitation number, like shown in Fig. 3-13.

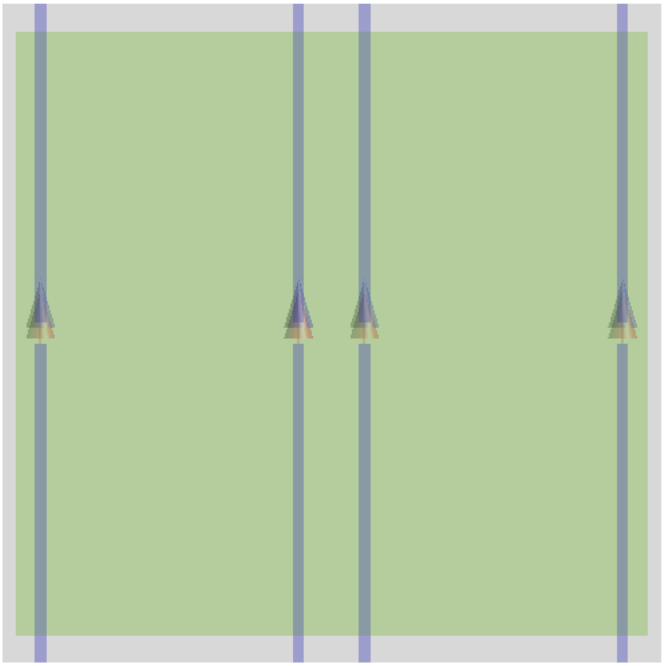

Figure 3-13. Four feedings on the bottom side.

In the new design, the same powering and delivering system can be used as in the former design, so the cost of the system will not increase (to double the excitation number, we can simply replace the 4-way power divider with an 8-way power divider, but to achieve the same bandwidth and power handling level, the cost will be much higher).

Using the same simulation setup (as prescribed in the ASTM standard, the gelled saline should have a relative permittivity of 78 and an electrical conductivity of 0.47 S/m. The wall of the acrylic box is 12.5 mm thick, and the box outer dimensions are 300 mm by 300 mm by 120 mm, the height of the gel is 90mm.), we did the full-wave EM simulation in commercial EM software SEMCAD, and the field distribution in the phantom box is shown in Fig. 3-14.

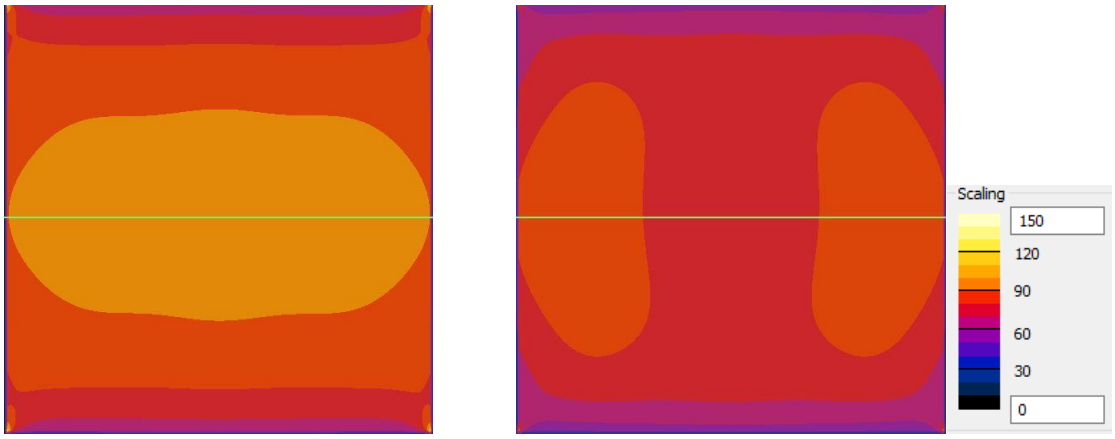

(a) (b)

Figure 3-14. Field distribution in the new phantom box for (a) 1.5 T and (b) 3 T.

To quantitively show the improvement in the generated electrical field homogeneity, we plotted the electrical field distribution on the center slice and extracted the field strength along x and z direction going through the center point, as shown in Fig. 3-15. As we can see from the figure, for the former design, the field variation compared with the center point reaches 20% within the distance of 30mm on x direction, and in the new design, this value is reduced to 4% at 1.5 T; for the former design, the field variation compared with the center point reaches 40% within the distance of 30mm on x direction, and in the new design, this value is reduced to 5% at 3 T. And instead of continuously dropping from the center, now the field strength varies periodically.

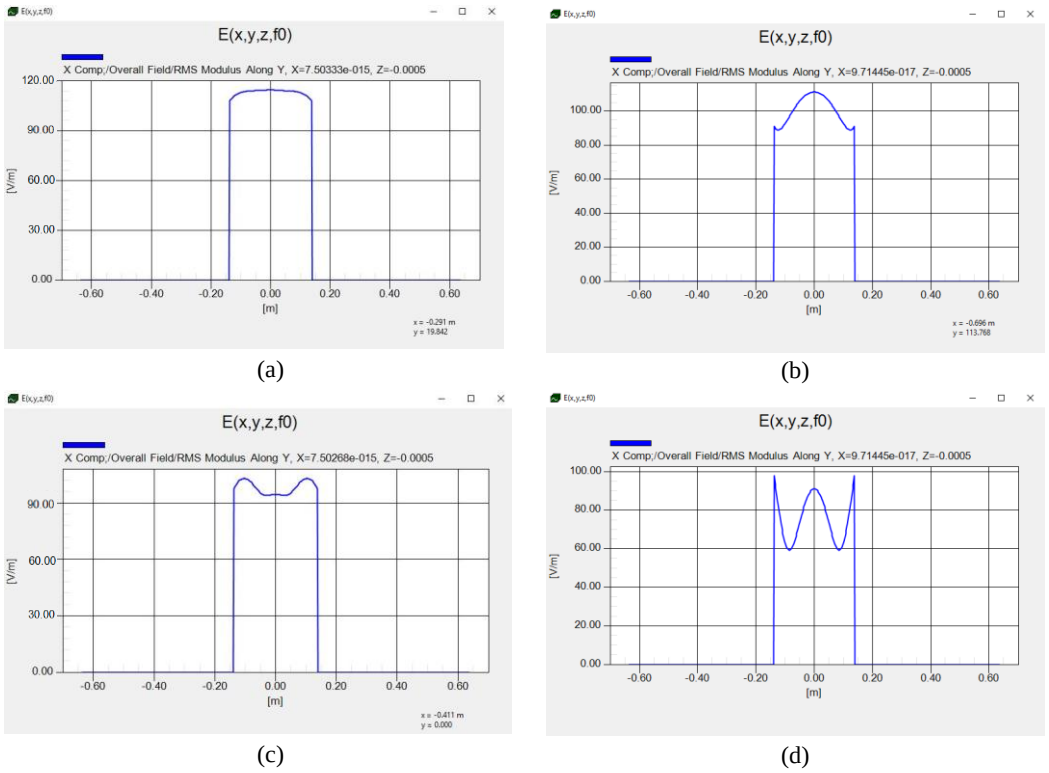

Figure 3-15. Field strength extraction along the x direction (blue line in Fig. 3-14), for (a) 1.5 T of the new design, (b) 1.5 T of the former design, and (c) 3 T for the new design, (d) 3 T for the former design.

By changing the way and position of excitation, we can see the generated electrical field homogeneity has been improved a lot, thus we can design a larger field generator for devices with larger dimension, as shown in Fig. 3-16, the dimension of the phantom box is doubled on the x direction. And we did the simulation for the new phantom box still using same setup, to make the fabrication of the new design easier, we shifted the long connecting copper striped of the same port a little bit away from each other, so that the SMA header can be mounted, as shown in Fig. 3-17, which is the built prototype of the 600mm x 300mm field generator. The positions of the excitations are adjusted to get better homogeneity of the electrical field distribution, as the simulation results are shown in Fig. 3-18. This design will have acceptable field homogeneity and will be able to be used to test devices with larger dimension.

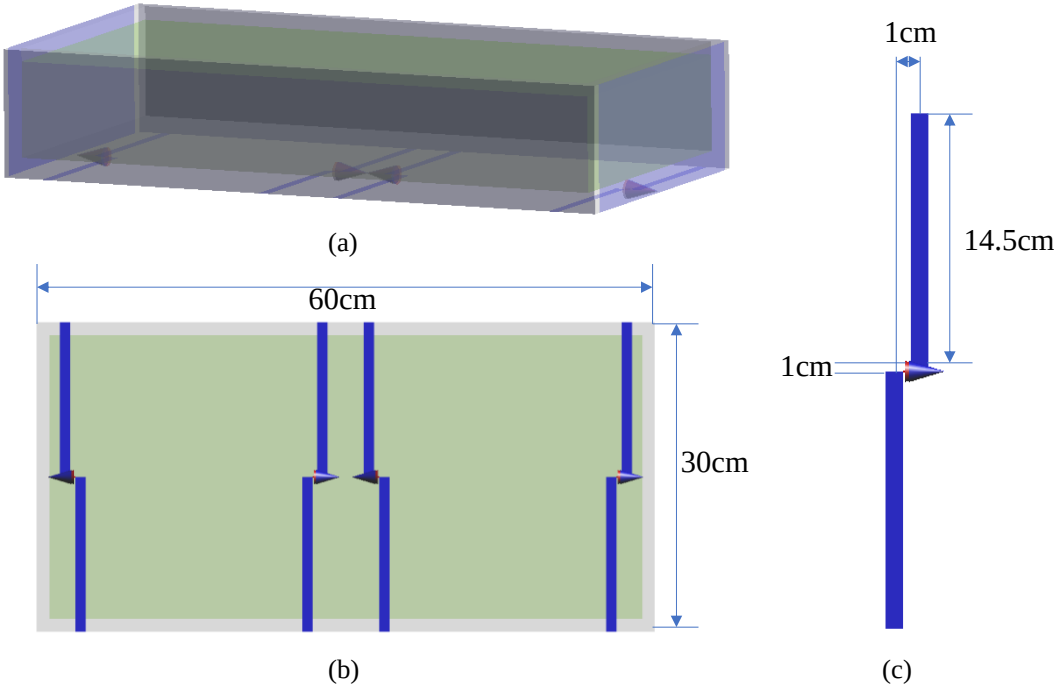

Figure 3-16. Dimension of the long box. (a) shows the structure of the long box. (b) bottom view of the excitation ports. (c) shows the detailed dimension of each excitation element.

Figure 3-17. Excitation port of the box in the prototype.

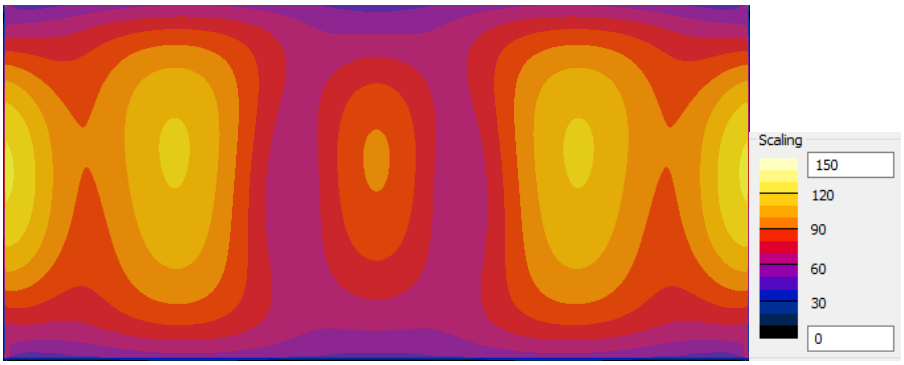

(a)

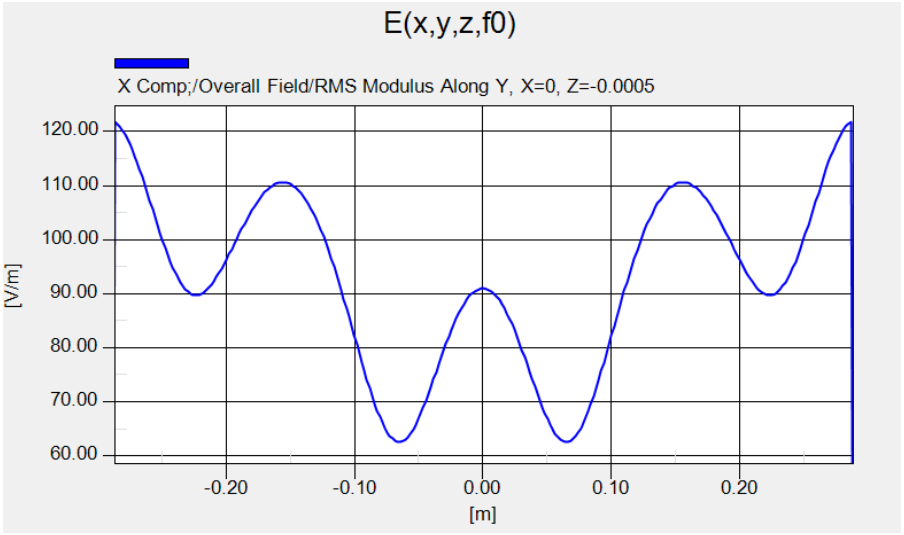

(b)

Figure 3-18. Field distribution of the long box at the center slice of the gel, (a) shows the linear scale results normalized to equivalent to 2 W/kg whole-body averaged SAR in ASTM phantom, (b) shows the electrical field strength along horizontal line.

To validate the electric field distributions inside the field generator experimentally, a 100 mm titanium rod was placed in 21 locations at the centre slice of the gel as shown in Fig. 3-19. These 21 positions were chosen with step size of 60 mm along the x-direction and step size of 60 mm along the z direction as shown in Fig.3-19 (a). The rod was placed 45 mm under the gel surface which was 90 mm above the bottom of the resonator. Temperature rises were recorded for 120 seconds at all these locations when continuous RF power was turned on at 3T. Numerical simulations were also performed based on the same experimental setups at different rod locations.

Comparisons of the 120 seconds temperature rises are shown in Fig. 3-19 (b) and (c). As clearly shown in the figure, in the results by experiment measurements were in good agreement those from simulations. The power is normalized so that the electrical field strength at the center will be equivalent to it of the ASTM phantom when the whole-body SAR is normalized to 1 W/kg (since in the measurement for now we do not have enough power supply, we use 1 W/kg instead of 2 W/kg, but basically the results can be considered linear to the input power).

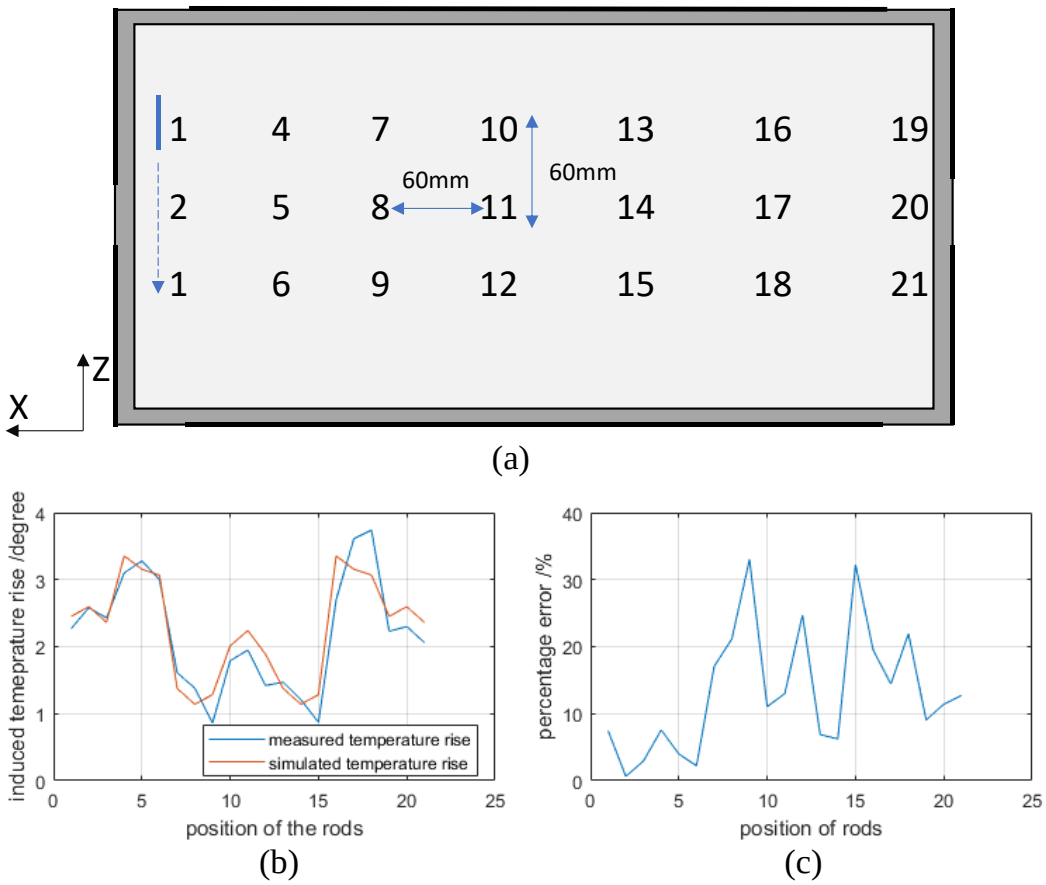

Figure 3-19. Experimental validation of the induced electrical field using rods. (a) shows the location of the rods, (b) shows the data for the measured and simulated temperature rise.

To further validate our design, two real 900-mm commercial AIMD lead was placed in the new designed phantom box with 7 different pathways, as shown in Fig. 3-20. The design of such pathways will be explained in later chapters.

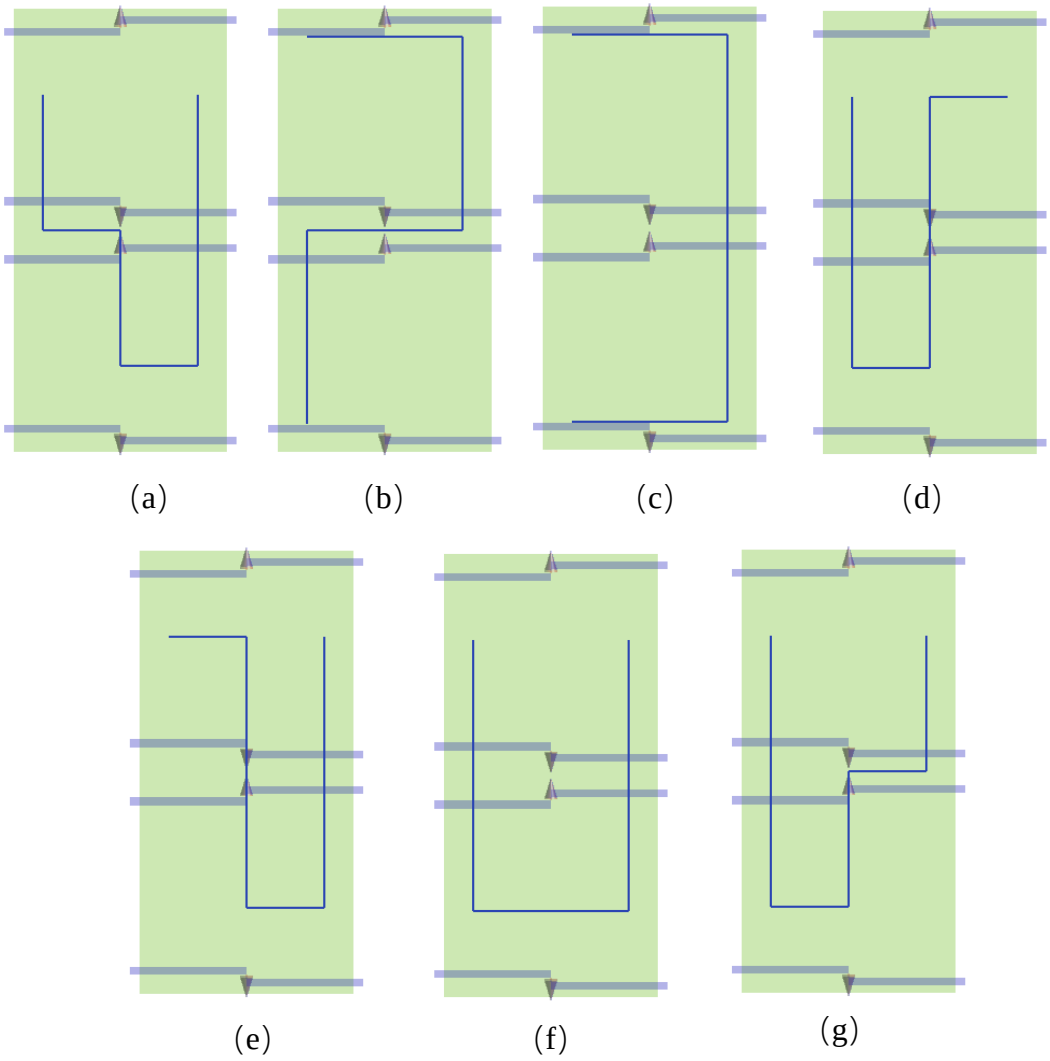

Figure 3-20. 7 pathways used for the validation of the long box.

The electrical field strength is normalized to same level as 2 W/kg whole-body averaged SAR in the ASTM standard test system. The transfer function of the lead is shown in Fig. 3-21, the field strength and phase are shown in Fig. 3-22, the induced temperature rises are calculated using transfer function method and compared with the experimental results, as shown in Fig. 3-23.

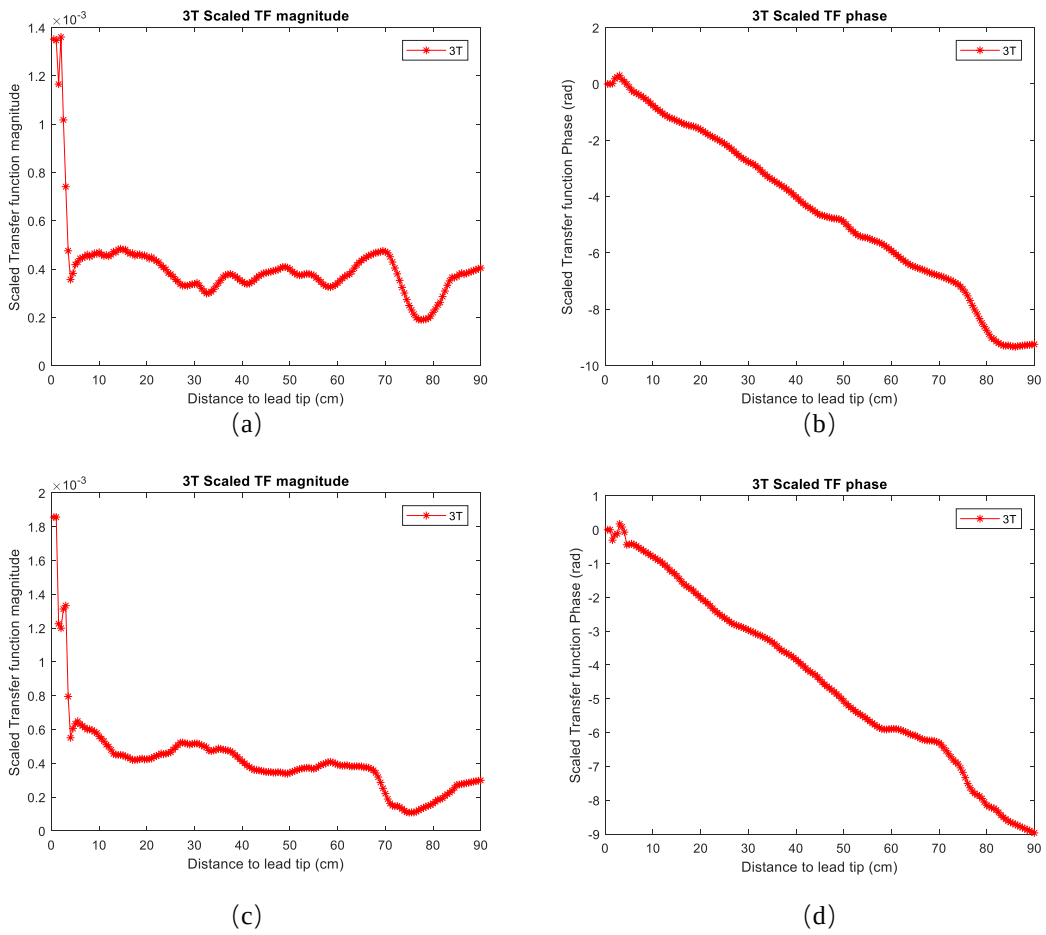

Figure 3-21. Transfer function of the used leads for the validation, (a)(b) show the transfer function magnitude and phase of the lead 1, (c)(d) shows the transfer function magnitude and phase of the lead 2. Both leads have the length of 900 mm, and the transfer functions are measured at 3T (128 MHz).

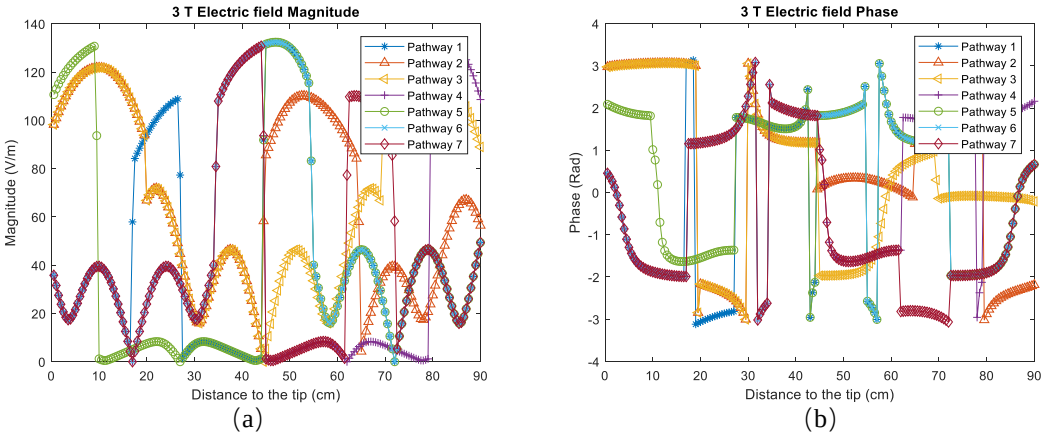

Figure 3-22. The incident electrical field on the pathways in the field generator. (a) shows the field magnitude and (b) show the phase. These pathways will have relatively high independency of the electrical field.

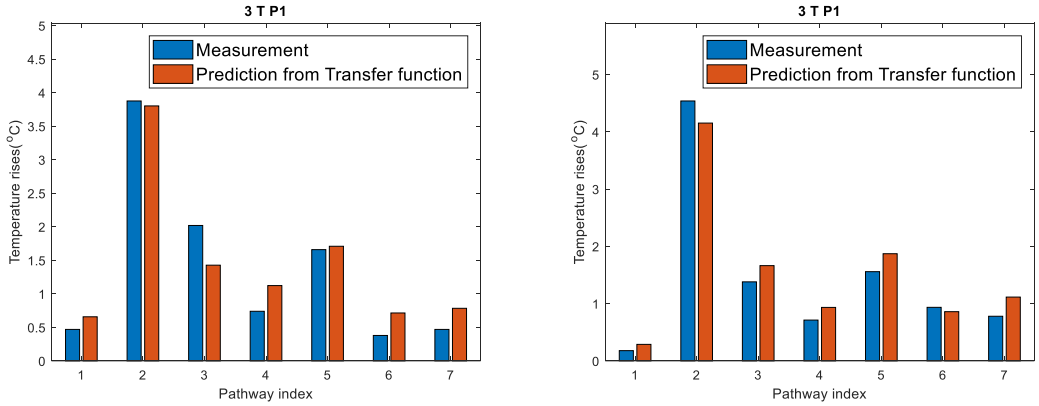

(a) (b)

Figure 3-23. Comparison of the temperature for measured results and predicted from transfer function, (a) shows the results for lead 1, (b) shows the results for lead 2.

As shown in Fig. 3-23, the theoretically calculated temperature rises results have good corelation with measured ones, except some points with low induced temperature rises.

Chapter 4. NOVEL RADIATOR APPLICATION FOR ACTIVE IMPLANTABLE MEDICAL DEVICES (AIMDS) MRI SAFETY ASSESSMENT

4.1. **Introduction**

Magnetic resonance imaging (MRI) is widely used in both clinical and research field for its excellent imaging quality of soft tissue and noninvasive, painless imaging procedure. Nowadays there are growing population of patients with active implantable medical devices (AIMDs) need to undergo MRI scanning. Typical AIMDs always have long wire structures, those long wires named leads will interact with the MRI scanner and induce localized high energy deposition. Such high power will cause high temperature to rise in human body tissue and induce high voltage on AIMDs, severe burnt and damage of AMIDs have been reported in many cases [65]–[67].

Given the varied surrounding tissues and trajectories of different kinds of AIMDs including deep brain stimulators (DBS), pacemakers (PM), and spinal cord stimulators (SCS), the exposure scenarios can be quite complicated. Also, the in-vivo temperature rise measurement in human body is not feasible. The transfer function method is proposed by SM Park. et al. to evaluate the induced hazards of AIMDs, and the transfer function, as a device model, should be validated in in-vitro experiment [68], [69]. The validation method recommended in ISO/TS requires large, expensive MRI scanner for each frequency and the pathways used for the validation are too complicated to achieve [70]. More importantly, the incident electric field in the scanner under such pathways is not independent enough to characterize a transfer

function, mathematically, this means the condition number of the incident field matrix is not adequate to solve the inverse problem of device model parameters to characterize a transfer function, the temperature rise can be quite similar with totally different transfer function.

In this paper, a novel validation system is proposed to solve such problems. The validation system consists of two parts, the first part is a test fixture which integrates the 1.5 T and 3 T test and generating uniform field under both frequencies. The second part is a sets of validation pathways based on Hadamard matrix, the incident field in the novel fixture under such pathways will be highly independent and the induced temperature rise in experiment will be much higher than the noise of background heating. This novel validation system is easy to operate, low-cost and requires smaller space and lower operating energy.

4.2. **Methodology and Material**

Validation of the transfer function is typically performed with measurement of induced temperature rise near the tip of the leads under different exposure field. The measured temperature rise will be compared with those from theoretical calculation based on transfer function theory by

$$\Delta T = \left|\int_L TF(l)E_{\tan}(l)dl\right|^2, \quad (4\text{-}1)$$

where *TF(l)* is the transfer function to be validated, *Etan (l)* is the incident field, ΔT is the induced temperature rise near the lead's tips. The incident field will be dependent

on two parts, the field distribution in the test fixture and the pathways used in the validation experiments.

4.2.1. **Test fixture design**

The test fixture design of the uniform electrical field generator is referred in the Chapter 3, Fig. 4-1. The basic design of 300 mm x 300 mm is used in this study.

4.2.2. **Pathway design**

To meet the requirement of the validation, the resulted incident field of the pathways should have two features:

(1): independent enough to characterize a transfer function.

(2): the induced temperature rise with the target transfer function should be significantly higher than the background heating of the phantom material.

(3): experimentally accessible for leads with different mechanical features.

The pathways developed in this paper is based on Hadamard matrix, such matrixes have entries of either +1 or -1, and are mutually orthogonal. The pathways used for the experimental validation are as suggested in unpublished research of Yu. et al [71]. Such pathways are simple and orthogonal. To guarantee the resulted temperature rise is high enough for accurate measurements, '-1' elements are replaced with '0'. The pathways are shown in Fig. 4-1. Leads segments going in same direction with the generated electric field are considered as '1' element in Hadamard matrix, segments going in orthogonal direction to the electric field are considered as '0'

elements. Some segments are reverted in 3 T for transfer function of these segments will have reversed phase with shorter wavelength, as shown in Fig. 4-1. (b).

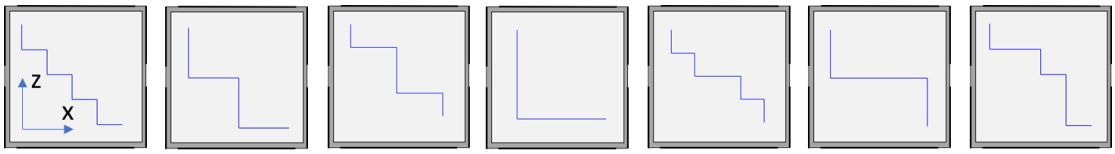

(a)

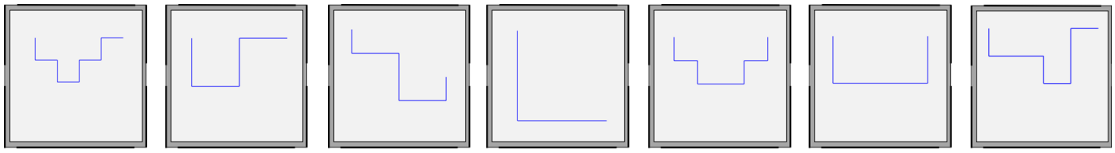

(b)

Figure 4-1. Pathways for (a) 1.5 T and (b) 3 T transfer function validation

4.3. **Experiments and Results**

Two generic AIMDs with different leads length are used to do the experimental validation. The transfer function of the AIMDs is shown in Fig. 4-2. Fig. 4-3. show the set up for the experiment and the generic AIMDs used in the validation experiments. Transfer function of the AIMDs is measured using VNA based on reciprocity.

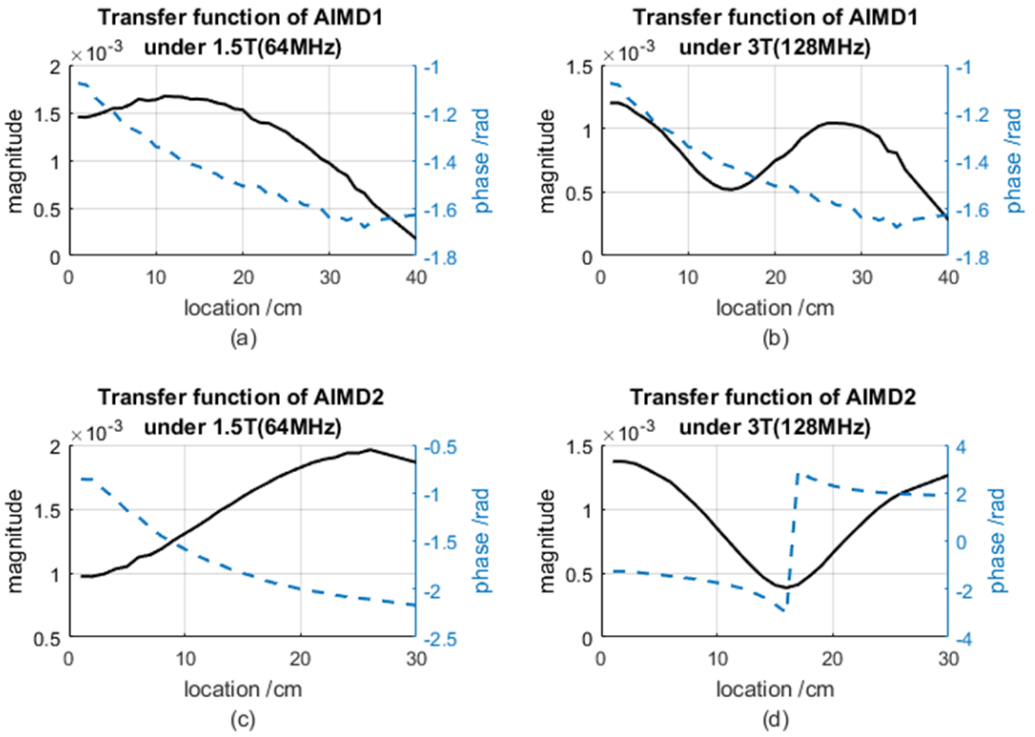

Figure 4-2. Transfer function of (a) generic AIMD1 under 1.5 T (64 MHz), (b) AIMD1 under 3 T (128 MHz), (c) AIMD2 under 1.5 T (64 MHz), (d) AIMD2 under 3 T (128 MHz), solid lines show the magnitude of the transfer function, dotted lines show the phase of the transfer function.

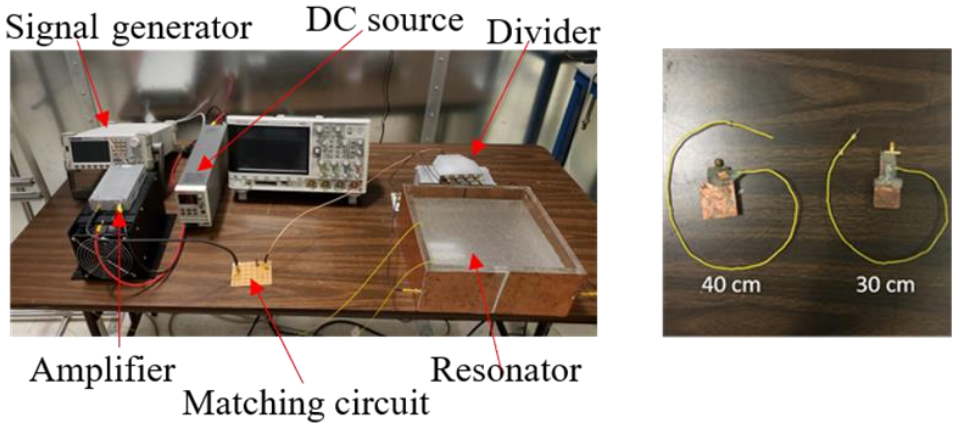

Figure 4-3. Experimental set up of (a) test system and (b) generic AIMDs

Validation experiments were performed for both AIMDs under 1.5 T and 3 T in the test fixture prototype shown in Fig. 4-3. (a). In all the experiments, the AIMDs with leads were placed at the centre slice of the gel, the gel used in the experiments has the permittivity of 78 and electrical conductivity of 0.47 S/m, electromagnetic field were

applied for 300 s, temperature rise near the tips of the leads were measured using optical fibre probe and compared with those from the transfer function theory calculation based on simulated electric field results. All the results are shown in Fig. 4-4, for all cases the results show good consistence with the theoretical calculation results.

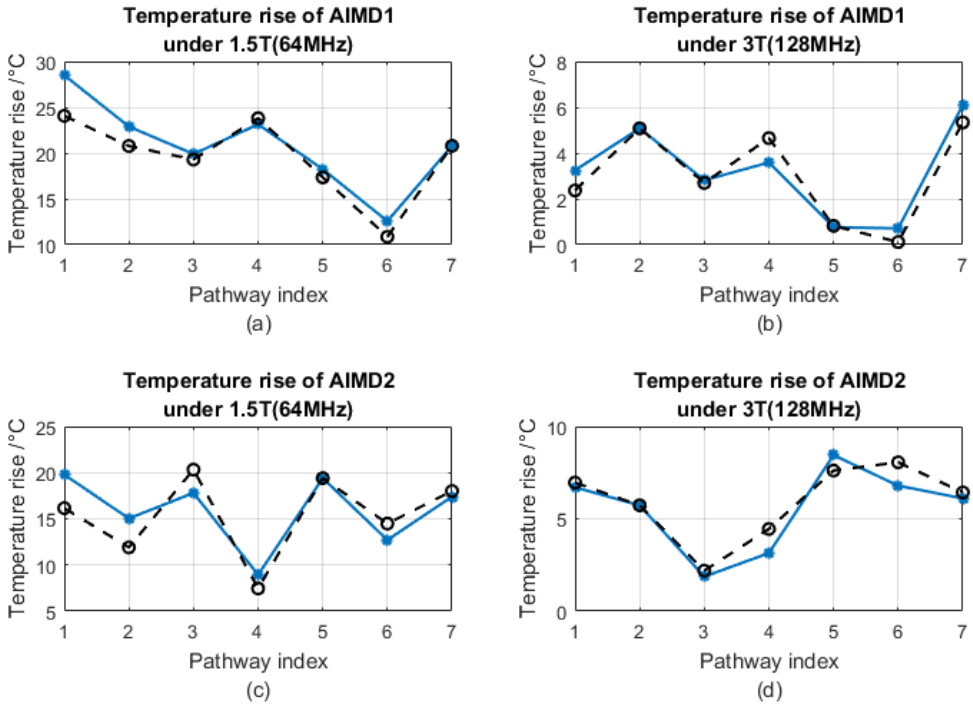

Figure 4-4. Temperature rise comparison of (a) AIMD1 under 1.5 T (64 MHz), (b) AIMD1 under 3 T (128 MHz), (c) AIMD2 under 1.5 T (64 MHz), (d) AIMD2 under 3 T (128 MHz).

4.4. **Conclusion**

In this paper, a novel device model validation system for 1.5 T and 3 T MRI safety assessment is proposed, experimental validations were performed with two generic AIMDs. The results show the novel device model validation system can integrate 1.5 T and 3 T transfer function validation in one test fixture, and the incident field in the test fixture under Hadamard matrix-based pathways can provide stable and

significant temperature rise, moreover, the novel test system has the advantage of small dimensions, low cost, and highly independent incident field.

References

[1] IEC. Medical electrical equipment – Part 2–33: Particular requirements for the basic safety and essential performance of magnetic resonance equipment for medical diagnosis. International Electrotechnical Commission 2010; 60601–2–33 ed. 3.0B (3rd Ed.3.0b).

[2] Pennes HH. Analysis of tissue and arterial blood temperatures in the resting human forearm. 1948. *J Appl Physiol* 1998; 85(1):5–34.

[3] Adair ER, Berglund LG. On the thermoregulatory consequences of NMR imaging. *Magn Reson Imaging* 1986; 4(4):321–333.

[4] Adair ER, Berglund LG. Predicted thermophysiological responses of humans to MRI fields. *Ann N Y Acad Sci* 1992; 649:188–200.

[5] ICNIRP. "Medical Magnetic Resonance (MR) Procedures: Protection of Patients," Health Physics 2004; 87(2):197–216.

[6] Shrivastava D, Vaughan JT. Radiofrequency Heating Models and Measurements. In: Vaughan JT, Griffiths J, editors. RF Coils for MRI. Chichester: John Wiley & Sons Ltd; 2012. p 425–436.

[7] Shrivastava D (Editor), Theory and Applications of Heat Transfer in Humans, 2018, John Wiley & Sons.

[8] Shrivastava D and Vaughan JT, 2009, "A Generic Bioheat Transfer Thermal Model for a Perfused Tissue," *ASME – Journal of Biomechanical Engineering*, Vol. 131, No. 7, pp. 074506.

[9] Shrivastava D, Utecht L, Tian J, Hughes J, and Vaughan JT, "In vivo radiofrequency heating in swine in 3T (123.2 MHz) birdcage whole body coil," *Magn Reson Med* 2014; 72(4):1141–50.

[10] Shrivastava D, Hanson T, Kulesa J, Tian J, Gregor A, and Vaughan JT, 2011, "Radiofrequency Heating in Porcine Models with a 'Large' 32 cm Internal Diameter, 7 T (296 MHz) Head Coil," *Magnetic Resonance in Medicine*, Vol. 66, No. 1, pp. 255–263.

[11] Sapareto SA, Dewey WC, "Thermal Dose Determination in Cancer Therapy," *Int. J. Radiation Oncology Biol. Phys*. 1984, Vol. 10, pp. 787–800.

[12] Henriques FC, Moritz AR, "Studies of Thermal Injury I. The Conduction of Heat to and through Skin and the Temperatures Attained Therein: A Theoretical and Experimental Investigation," *American Journal of Pathology*, vol. 23, (no. 4), pp. 531–549, 1947.

[13] Moritz AR, Henriques FC, "Studies in Thermal Injury II: The Relative Importance of Time and Surface Temperature in the Causation of Cutaneous Burns," *American Journal of Pathology*, vol. 23, (no. 5), pp. 695–720, 1947.

[14] Moritz AR, "Studies of Thermal Injury III. The Pathology and Pathogenesis of Cutaneous Burns: An Experimental Study," *American Journal of Pathology*, vol. 23, (no. 6), pp. 915–934, 1947.

[15] Shuman WP, Haynor DR, Guy AW, Wesbey GE, Schaefer DJ, Moss AA, "Superficial- and deep-tissue temperature increases in anesthetized dogs during

exposure to high specific absorption rates in a 1.5-T MR imager," *Radiology* 1988; 167(2):551–554.

[16] Barber BJ, Schaefer DJ, Gordon CJ, Zawieja DC, Hecker J, "Thermal effects of MR imaging: worst-case studies on sheep," *AJR Am J Roentgenol* 1990; 155(5):1105–1110.

[17] Kido D, Morris T, Erickson J, Plewes D, Simon J, "Physiologic changes during high field strength MR imaging," *AJR Am J Roentgenol* 1987; 148(6):1215–1218.

[18] Shellock F, Rothman B, Sarti D, "Heating of the scrotum by high-field-strength MR imaging," *AJR Am J Roentgenol* 1990; 154(6):1229–1232.

[19] Shellock FG, Schaefer DJ, Crues JV, "Alterations in body and skin temperatures caused by magnetic resonance imaging: is the recommended exposure for radiofrequency radiation too conservative?" *Br J Radiol* 1989; 62(742):904–909.

[20] Shellock FG, Schaefer DJ, Kanal E, "Physiologic responses to an MR imaging procedure performed at a specific absorption rate of 6.0 W/kg," *Radiology* 1994; 192(3):865–868.

[21] Boss A, Graf H, Berger A, Lauer UA, Wojtczyk H, Claussen CD, Schick F, "Tissue warming and regulatory responses induced by radio frequency energy deposition on a whole-body 3-Tesla magnetic resonance imager," *J Magn Reson Imaging* 2007; 26(5):1334–1339.

[22] ASTM F2182-19. Standard test method for measurement of radio frequency induced heating near passive implants during magnetic resonance imaging. ASTM Committee F04 on Medical and Surgical Materials and Devices, Subcommittee F04.15 on Material Test Methods. West Conshohocken, PA: ASTM International; 2019.

[23] J. T. Vaughan, M. Garwood, C. M. Collins, W. Liu, L. DelaBarre, G. Adriany, P. Andersen, H. Merkle, R. Goebel, M. B. Smith, and K. Ugurbil, "7T vs. 4T: RF power, homogeneity, and signal-to-noise comparison in head images," *Magn. Reson. Med.*, vol. 46, no. 1, pp.

[24] B. Wu, C. Wang, D. A. C. Kelly, D. Xu, D. B. Vigneron, S. J. Nelson, X. Zhang, "Shielded Microstrip Array for 7T Human MR Imaging," in *IEEE Transactions on Medical Imaging*, vol. 29, no. 1, pp. 179–184, Jan. 2010, doi: 10.1109/TMI.2009.2033597.

[25] Xiaoliang Zhang, K. Ugurbil, R. Sainati and Wei Chen, "An inverted-microstrip resonator for human head proton MR imaging at 7 tesla," in *IEEE Transactions on Biomedical Engineering*, vol. 52, no. 3, pp. 495–504, March 2005, doi: 10.1109/TBME.2004.842968.

[26] G. Eichfelder and M. Gebhardt, "Local specific absorption rate control for parallel transmission by virtual observation points," *Magn. Reson. Med.*, vol. 66, no. 5, pp. 1468–1476, 2011.

[27] E. D. Karnin, “A simple procedure for pruning back-propagation trained neural networks,” in *IEEE Transactions on Neural Networks*, vol. 1, no. 2, pp. 239–242, June 1990, doi: 10.1109/72.80236.

[28] S. Hashem, “Sensitivity analysis for feedforward artificial neural networks with differentiable activation functions,” *[Proceedings 1992] IJCNN International Joint Conference on Neural Networks*, Baltimore, MD, USA, 1992, pp. 419–424 vol.1, doi: 10.1109/IJCNN.1992.287175.

[29] A. K. Jain and J. Mao, “Artificial neural network for nonlinear projection of multivariate data,” *[Proceedings 1992] IJCNN International Joint Conference on Neural Networks*, Baltimore, MD, USA, 1992, pp. 335–340 vol.3, doi: 10.1109/IJCNN.1992.227152.

[30] D. C. Park, M. A. El-Sharkawi, R. J. Marks, L. E. Atlas and M. J. Damborg, “Electric load forecasting using an artificial neural network,” in *IEEE Transactions on Power Systems*, vol. 6, no. 2, pp. 442–449, May 1991, doi: 10.1109/59.76685.

[31] Y. Kim, S. S. Cheng, M. Diakite, R. P. Gullapalli, J. M. Simard and J. P. Desai, “Toward the Development of a Flexible Mesoscale MRI-Compatible Neurosurgical Continuum Robot,” in *IEEE Transactions on Robotics*, vol. 33, no. 6, pp. 1386–1397, Dec. 2017, doi: 10.1109/TRO.2017.2719035.

[32] A. Christ, W. Kainz, E. G. Hahn, K. Honegger, M. Zefferer, E. Neufeld, W. Rascher, R. Janka, W. Bautz, J. Chen, B. Kiefer, P. Schmitt, H.-P. Hollenbach, J. Shen, M. Oberle, D. Szczerba, A. Kam, J. W. Guag, and N. Kuster, “The

virtual family development of surface-based anatomical models of two adults and two children for dosimetric simulations," *Phys. Med. Biol.*, vol. 55, no. 2, pp. N23–N28, Jan. 2010.

[33] J. Tian, D. Shrivastava, "In vivo radiofrequency heating in a 3T scanner," Theory and application of heating transfer in humans, vol. 2, Hoboken, NJ, USA: Wiley, 2018, pp. 621–630.

[34] T. Kawamura, K. Saito, S. Kikuchi, M. Takahashi, and K. Ito, "Specific absorption rate measurement of birdcage coil for 3.0-T magnetic resonance imaging system employing thermographic method," *IEEE Trans. Microw. Theory Techn.*, vol. 57, no. 10, pp. 2508–2514, 2009.

[35] J. Liu, J. Zheng, Q. Wang, W. Kainz, and J. Chen, "A Transmission Line Model for the Evaluation of MRI RF-Induced Fields on Active Implantable Medical Devices," *IEEE Trans. Microw. Theory Techn.*, vol. 66, no. 9, pp. 4271–4281, 2018.

[36] S. Feng, R. Qiang, W. Kainz, and J. Chen, "A technique to evaluate MRI-induced electric fields at the ends of practical implanted lead," *IEEE Trans. Microw. Theory Techn.*, vol. 63, no. 1, pp. 305–313, 2015.

[37] J. A. Nyenhuis, S. M. Park, R. Kamondetdacha, A. Amjad, F. G. Shellock, and A. R. Rezai, "MRI and implanted medical devices: Basic interactions with an emphasis on heating," *IEEE Trans. Device Mater. Rel.*, vol. 5, no. 3, pp. 467–479, 2005.

[38] J. A. Erlebacher, P. T. Cahill, F. Pannizzo, and R. J. R. Knowles, “Effect of magnetic resonance imaging on DDD pacemakers,” *Am. J. Cardiol.*, vol. 57, no. 6, pp. 437–440, 1986.

[39] A. M. Sawyer-Glover and F. G. Shellock, “Pre-MRI procedure screening: Recommendations and safety considerations for biomedical implants and devices,” *J. Magn. Reson. Imaging*, vol. 12, no. 1, pp. 92–106, 2000.

[40] J. De Poorter, C. De Wagter, Y. De Deene, C. Thomsen, F. Ståhlberg, and E. Achten, “Noninvasive MRI thermometry with the proton resonance frequency (PRF) method: In vivo results in human muscle,” *Magn. Reson. Med.*, vol. 33, no. 1, pp. 74–81, Jan. 1995.

[41] P. Ehses, F. Fidler, P. Nordbeck, E. D. Prachat, M, Warmuth, P. M. Jakob, W. R. Bauer, “MRI thermometry: Fast mapping of RF-induced heating along conductive wires,” *Magn. Reson. Med.*, vol. 60, no. 2, pp. 457–461, 2008.

[42] https://www.stryker.com/us/en/portfolios/neurotechnology-spine/neurovascular/embolization/test.html

[43] https://www.jnjmedicaldevices.com/sites/default/files/user_uploaded_assets/pdf_assets/2019-09/MRI%20Safety%20Brochure.pdf

[44] C. M. Collins, W. Liu, J. Wang, R. Gruetter, J. T. Vaughan, K. Ugurbil, M. B. Smith, “Temperature and SAR Calculations for a Human Head Within Volume and Surface Coils at 64 and 300 MHz,” *J. Magn. Reson. Imaging*, vol. 19, no. 5, pp. 650–656, 2004.

[45] R. Yang, J. Zheng, W. Kainz, and J. Chen, “Numerical Investigations of MRI RF-Induced Heating for External Fixation Device in TEM and Birdcage Body Coils at 3 T,” *IEEE Trans. Electromagn. Compat*., vol. 60, no. 3, pp. 598–604, 2018.

[46] ASTM F2182-19e. “Standard test method for measurement of radio frequency induced heating on or near passive implants during magnetic resonance imaging,” 2019.

[47] D. Li, J. Zheng, Y. Liu, C. Pan, W. Kainz, F. Yang, W. Wu, J. Chen, “An Efficient Approach to Estimate MRI RF Field Induced in Vivo Heating for Small Medical Implants,” *IEEE Trans. Electromagn. Compat*., vol. 57, no. 4, pp. 643–650, 2015.

[48] ASTM F2182-11a. “Standard test method for measurement of radio frequency induced heating on or near passive implants during magnetic resonance imaging,” 2011.

[49] Y. Liu, J. Chen, F. G. Shellock, and W. Kainz, “Computational and experimental studies of an orthopedic implant: MRI-related heating at 1.5-T/64-MHz and 3-T/128-MHz,” *J. Magn. Reson. Imaging*, vol. 37, no. 2, pp. 491–497, 2013.

[50] S. McCabe and J. Scott, "A Novel Implant Electrode Design Safe in the RF Field of MRI Scanners," in *IEEE Transactions on Microwave Theory and Techniques*, vol. 65, no. 9, pp. 3541–3547, Sept. 2017, doi: 10.1109/TMTT.2017.2669977.

[51] S. M. Park, J. A. Nyenhuis, C. D. Smith, E. J. Lim, K. S. Foster, K. B. Baker, G. Hrdlicka, A.R. Rezai, P. Ruggieri, A. Sharan, F.G. Shellock, P.H. Stypulkowski, J. Tkach, "Gelled Versus Nongelled Phantom Material for Measurement of MRI-Induced Temperature Increases with Bioimplants," *IEEE Trans. Magn.*, vol. 39, no. 5 II, pp. 3367–3371, 2003.

[52] H. S. Ho, "Safety of metallic implants in magnetic resonance imaging," *J. Magn. Reson. Imaging*, vol. 14, no. 4, pp. 472–477, 2001.

[53] F. G. Shellock, "Magnetic resonance safety update 2002: Implants and devices," *J. Magn. Reson. Imaging*, vol. 16, no. 5, pp. 485–496, 2002.

[54] P. Nordbeck, I. Weiss, P. Ehses, O. Ritter, M. Warmuth, F. Fidler, V. Herold, P. M. Jakob, M.E. Ladd, H.H. Quick, W.R. Bauer, "Measuring RF-induced currents inside implants: Impact of device configuration on MRI safety of cardiac pacemaker leads," *Magn. Reson. Med.*, vol. 61, no. 3, pp. 570–578, 2009.

[55] P. Nordbeck, P. Nordbeck, F. Fidler, I. Weiss, M. Warmth, M.T. Friedrich, P. Ehses, W. Geistert, O. Ritter, P.M. Jakob, M.E. Ladd, H.H. Quick, W.R. Bauer, "Spatial distribution of RF-induced E-fields and implant heating in MRI," *Magn. Reson. Med.*, vol. 60, no. 2, pp. 312–319, 2008.

[56] Road vehicles - Vehicle test methods for electrical disturbances from narrowband radiated electromagnetic energy, ISO Std. 11451–2, 2005.

[57] V. Rodriguez, “Analysis of large E field generators in semi-anechoic chambers used for full vehicle immunity testing: Numerical and measured results,” *IEEE Int. Symp. Electromagn. Compat.*, vol. 2014-December, pp. 681–684, 2014.

[58] J. S. McLean, “Electric field generator incorporating a slow-wave structure,” U.S. Patent 7.656.167, issued Feb. 2, 2010.

[59] C. Groh, J. P. Kärst, M. Koch, and H. Garbe, “TEM waveguides for EMC measurements,” *IEEE Trans. Electromagn. Compat.*, vol. 41, no. 4 PART 2, pp. 440–445, 1999.

[60] ISO/TS 10974:2018, 2nd Edition, “Assessment of the safety of magnetic resonance imaging for patients with an active implantable medical device,” Apr. 2018.

[61] H. F. Chen and K. H. Lin, “A numerical analysis of antenna factor of bilog antennas for normalized site attenuation and EMC measurement,” *IEEE Int. Symp. Electromagn. Compat.*, vol. 2, pp. 817–821, 2003.

[62] D. M. Pozar, “Microstrip antenna coupled to a microstrip-line,” *Electron. Lett.*, vol. 21, no. 2, pp. 49–50, Jan. 1985.

[63] International Electrotechnical Commission (IEC), Medical electrical equipment - Part 2-33: Particular requirements for the basic safety and essential performance of magnetic resonance equipment for medical diagnosis (IEC-60601-2-33). IEC: Geneva, 2010.

[64] E. Lucano, M. Liberti, G.G. Mendoza, M.I. Lacono, F. Apollonio, S. Wedan, W. Kainz, L.M. Angelone, “Assessing the electromagnetic fields generated by a

radiofrequency MRI body coil at 64 MHz: Defeaturing versus accuracy," *IEEE Trans. Biomed. Eng.*, vol. 63, no. 8, pp. 1591–1601, 2016.

[65] J. G. Delfino, D. M. Krainak, S. A. Flesher, and D. L. Miller, "MRI -Related FDA Adverse Event Reports: A 10-Year Review," *Med. Phys.*, 2019.

[66] S. Achenbach, W. Moshage, B. Diem, T. Bieberle, V. Schibgilla, and K. Bachmann, "Effects of magnetic resonance imaging on cardiac pacemakers and electrodes," *Am. Heart J.*, vol. 134, no. 3, pp. 467–473, 1997.

[67] R. Yang, J. Zheng, Y. Wang, R. Guo, W. Kainz, and J. Chen, "An Absorbing Radio Frequency Shield to Reduce RF Heating Induced by Deep Brain Stimulator During 1.5-T MRI," *IEEE Trans. Electromagn. Compat.*, vol. PP, pp. 1–7, 2019.

[68] S. M. Park, R. Kamondetdacha, and J. A. Nyenhuis, "Calculation of MRI-induced heating of an implanted medical lead wire with an electric field transfer function," *J. Magn. Reson. Imaging*, vol. 26, no. 5, pp. 1278–1285, 2007.

[69] J. Liu, J. Zheng, Q. Wang, W. Kainz, and J. Chen, "A Transmission Line Model for the Evaluation of MRI RF-Induced Fields on Active Implantable Medical Devices," *IEEE Trans. Microw. Theory Tech.*, vol. 66, no. 9, pp. 4271–4281, 2018.

[70] Assessment of the Safety of Magnetic Resonance Imaging for Patients with an Active Implantable Medical Device, ISO/TS 10974:2012, 2012.

[71] Y. Wang, S. Song, J. Zheng, Q. Wang, W. Kainz and J. Chen, “A Novel Device Model Validation Strategy for 1.5- and 3-T MRI Heating Safety Assessment,” in *IEEE Transactions on Instrumentation and Measurement*, vol. 69, no. 9, pp. 6381–6389, Sept. 2020, doi: 10.1109/TIM.2020.2971292.

Appendix I. Uncertainty analysis of human body modeling

I.1. Introduction

This document provides the uncertainty assessment for the human modelling. The uncertainty process evaluation follows ISO/TS 10974 Ed. 1 Annex R. According to this document, the result of a simulation value y is a function of N parameters $x_1, x_2, \ldots, x_N$. The combined standard uncertainty $u_c(y)$ can be derived from individual uncertainty components $u(x_i)$. The total uncertainty can be calculated from root sum square of the uncertainty of the individual components

$$u_c(y) = \sqrt{\sum_{i=1}^{m} c_i^2 \cdot u^2(x_i)}, \qquad \text{(I-1)}$$

in this formula c_i is the sensitivity coefficient calculated by $\partial y / \partial x_i . u(x_i)$ is the standard deviation of each term and $u_c(y)$ is the combined uncertainty.

The uncertainty sources in our test case are listed as below:

1. Uncertainty of the loading position
2. Uncertainty of the tissue properties
3. Uncertainty of the grid resolution
4. Uncertainty of the coil input
5. Uncertainty of prediction

I.2. Individual uncertainty evaluation

The individual uncertainty can be evaluated in two steps:

A. the calculation of the sensitivity coefficient

B. The evaluation of the standard deviation of each individual term.

The sensitivity coefficients of the loading position, tissue properties including density, conductivity and permittivity, and grid resolution are estimated. And the result of the target value *y* is the SAR in our situation. Therefore, we have

$$y = \text{SAR}. \tag{I-2}$$

We assume the SAR of the human model simulation is a function of the loading position, tissue properties including density, conductivity and permittivity, and grid resolution. And it is a linear equation when the variation of these parameters is small. The sensitivity coefficient can be written as$\Delta y/\Delta x_i$. SAR includes Whole-body SAR (WBSAR), Partial-body SAR (PBSAR), Head SAR (HSAR) and 10g averaged SAR Local maximum (Local max) which should be limited in MRI scanning, WBSAR is measured from Q factor, other kinds of SAR are normalized to same WBSAR (1W/kg).

I.2.1. Loading position

To calculate the sensitivity coefficients regarding to the loading position, the loading position is moved ± 10 mm in the x, y, z direction from the standard position (eye lens at the middle of the coil in y, z direction and the human model lies on the bed in y direction, position of the bed is measured and provided by UIH, 420mm from the top of the coil).

The sensitivity coefficient is calculated for each direction. The relative percentage is obtained by dividing the sensitivity coefficient by the calculated SAR *y* when the human model is at the standard position.

Table I-I Sensitivity coefficient of loading position.

3 T		SAR variation (W/Kg)	Distance variation (mm)	Ratio of SAR/distance variation	$\Delta y / \Delta x / y_{standard}$ sensitivity coefficient (%)
PBSAR	X direction	0.102283	20	0.005114	0.152023
	Y direction	0.05529	20	0.002764	0.082176
	Z direction	0.203613	20	0.010181	0.302628
	Combination	--	--	--	0.348493
HSAR	X direction	0.330363	20	0.016518	0.37718
	Y direction	0.127741	20	0.006387	0.145844
	Z direction	0.412999	20	0.02065	0.471526
	Combination	--	--	--	0.621185
Local max	X direction	2.978355	20	0.148918	0.662929
	Y direction	4.47274	20	0.223637	0.995553
	Z direction	4.119315	20	0.205966	0.916887
	Combination	--	--	--	1.507078

I.2.2. Tissue properties

To calculate the sensitivity coefficient regarding to the tissue properties (density, conductivity, and permittivity), the deviation value of tissue density is from IT IS database [1], the value of conductivity and permittivity are set to be 20% from the original value separately. The relative percentage is obtained by dividing the sensitivity coefficient by the SAR calculated when the density, conductivity and permittivity are the original value.

Table I-II. Sensitivity coefficient of human tissue density, conductivity, and permittivity.

3 T		SAR variation (W/Kg)	Parameter of interests	Ratio of SAR/parameter variation	$\Delta y / \Delta x / y_{standard}$ sensitivity coefficient (%)
PBSAR	Density	0.00722432	7%	0.1032046	3.0678362
	Conductivity	0.002743362	20%	0.0137168	0.4077428
	Permittivity	-0.074978	20%	-0.37489	-11.1439
HSAR	Density	-0.04426901	7%	-0.6324146	-14.4406963
	Conductivity	0.116595248	20%	0.5829762	13.3118106
	Permittivity	-0.2593826	20%	-1.29691	-29.61401
Local max	Density	-1.11368062	7%	-15.9097233	-70.8244819
	Conductivity	0.675496571	20%	3.3774829	15.0353636
	Permittivity	-0.9347688	20%	-4.67384	-20.80631

Density of human body tissue is from ITIS.ETH database, different tissue will have different deviation, for the uncertainty analysis simulation, we use the maximum value measured.

I.2.3. Grid resolution

To calculate the sensitivity coefficient regarding to the grid resolution, the max step of the mesh is set to be 2.5 mm and 5 mm.

Table I-III. Sensitivity coefficient of the grid resolution.

3 T		SAR variation (W/Kg)	Grid size variation (mm)	Ratio of SAR/grid size variation	$\Delta y / \Delta x / y_{standard}$ sensitivity coefficient (%)
PBSAR	Grid resolution	0.005103122	2.5	0.002041249	0.060677707
HSAR	Grid resolution	-0.02250266	2.5	-0.009001066	-0.205532357
Local max	Grid resolution	-0.42408495	2.5	-0.169633983	-0.75515072

I.2.4. Coil input

Input of the coil has a phase error of ±10 degree and amplitude error of ±5%.

Table I-IV. Sensitivity coefficient of the coil input

Source of sensitivity coefficient		SAR variation (W/Kg)	Input source variation	Ratio of SAR/parameter variation	$\Delta y/\Delta x/y_{standard}$ sensitivity coefficient (%)
PBSAR	amplitude	0.002466	10%	0.02466	0.733043
	phase	0.280496	20	0.014025	0.416898
	amplitude	0.005081	10%	0.050805	1.160096
HSAR	phase	0.60104	20	0.030052	0.686214
Local	amplitude	0.881567	10%	8.815675	39.24428
max	phase	1.201046	20	0.060052	0.267332

Table I-V. Sensitivity coefficients of each individual term.

Source of sensitivity coefficient		
PBSAR	Loading position	0.348493
	Tissue density	3.0678362
	Tissue conductivity	0.4077428
	Tissue permittivity	-11.1439
	Grid resolution	0.060677707
	Input amplitude	0.733043
	Input phase	0.416898
HSAR	Loading position	0.621185
	Tissue density	-14.4406963
	Tissue conductivity	13.3118106
	Tissue permittivity	-29.61401
	Grid resolution	-0.205532357
	Input amplitude	1.160096
	Input phase	0.686214
Local max	Loading position	1.507078
	Tissue density	-70.8244819
	Tissue conductivity	15.0353636
	Tissue permittivity	-20.80631
	Grid resolution	-0.75515072
	Input amplitude	39.24428
	Input phase	0.267332

I.2.5. Prediction

We use the difference of the predicted SAR from the algrithom and the original simulated SAR divided by the original data as the uncertainty, as shown in the table 6 below, the uncertainty will be different for different landmark and mode.

Table I-VI. Uncertainty of prediction in %

Uncertainty of prediction		CP	EP1	EP2	EP3
PBSAR	head	3.95%	3.97%	3.96%	3.98%
	neck	5.28%	5.29%	5.34%	5.46%
	upper sternum	5.03%	5.01%	4.96%	4.91%
	heart	4.84%	4.82%	4.79%	4.71%
	liver	5.20%	5.17%	5.23%	5.27%
	abdomen	3.27%	3.24%	3.20%	3.17%
	pelvis	3.20%	3.21%	3.37%	3.79%
	groin	4.41%	4.48%	4.30%	4.08%
	knee	6.17%	6.02%	6.02%	5.78%
	ankle	4.63%	4.41%	5.01%	6.90%
HSAR	head	5.31%	5.36%	4.94%	4.53%
	neck	5.81%	5.79%	6.39%	7.15%
	upper sternum	7.68%	7.66%	7.97%	8.33%
	heart	46.40%	46.69%	56.51%	75.44%
	liver	17.65%	17.55%	17.89%	18.41%
	abdomen	26.60%	27.83%	24.89%	19.17%
	pelvis	16.91%	15.86%	19.29%	25.70%
	groin	21.18%	19.96%	33.07%	50.42%
	knee	100.80%	105.90%	108.03%	109.22%
	ankle	34.50%	36.82%	30.61%	25.61%
Local max	head	9.27%	8.63%	9.31%	5.37%
	neck	5.85%	5.85%	7.31%	3.87%
	upper sternum	6.69%	6.93%	5.58%	3.68%
	heart	11.36%	11.13%	11.95%	7.61%
	liver	4.85%	4.59%	5.27%	4.24%
	abdomen	2.52%	3.14%	2.36%	1.99%
	pelvis	4.09%	4.55%	3.38%	2.40%
	groin	8.91%	8.90%	9.59%	4.17%
	knee	2.06%	1.60%	3.03%	4.79%
	ankle	10.04%	10.56%	10.28%	11.95%

1. Based on the measurements, the estimated standard deviation of the loading position is 10 mm.

2. Based on the measurement of density from IT IS database [1], the standard deviation is 6.97065%.

3. The individual uncertainty components $u(x_i)$ is calculated regarding to the loading position, tissue density, conductivity and permittivity and grid resolution.

Biological tissues are inhomogeneous and show considerable variability in structure or composition and hence in dielectric properties. Such variations are natural and may be due to physiological processes or other functional requirements. The spread of values ranges from about ±5–10% above 100 MHz to ±15–25% at the lower end of the frequency scale [2], so the estimated individual standard deviation of the tissue dielectric properties is 10%.

4. The standard deviation of the grid resolution is estimated to be 1 mm

Table I-VII. Individual uncertainty component.

Source of uncertainty	Standard deviation
Loading position	10 mm
Tissue density	4.03%
Tissue conductivity	5.78%
Tissue permittivity	5.78%
Grid resolution	1 mm
Input amplitude	5%
Input phase	10 degrees

The combined uncertainty will be shown in the following table.

Table I-VIII. Uncertainty caused by each source.

Source of uncertainty		Uncertainty in %
PBSAR	Loading position	3.48493
	Tissue density	0.123633799
	Tissue conductivity	0.023567534
	Tissue permittivity	-0.64411742
	Grid resolution	0.060677707
	Input amplitude	0.03665215
	Input phase	4.16898
HSAR	Loading position	6.21185
	Tissue density	-0.581960061
	Tissue conductivity	0.769422653
	Tissue permittivity	-1.711689778
	Grid resolution	-0.205532357
	Input amplitude	0.0580048
	Input phase	6.86214
Local max	Loading position	15.07078
	Tissue density	-2.854226621
	Tissue conductivity	0.869044016
	Tissue permittivity	-1.202604718
	Grid resolution	-0.75515072
	Input amplitude	1.962214
	Input phase	2.67332

I.3. Combined uncertainty evaluation

Table I-IX. Uncertainty of numerical modeling.

Source of Uncertainty: liver		Uncertainty in %	Source of Numerical Value
PBSAR	Grid resolution	0.060677707	Numerical analysis performed by UH
	Tissue density, conductivity and permittivity	0.656298709	Numerical analysis performed by UH
	Loading position	3.48493	Numerical analysis performed by UH
	Coil input	4.169141113	Numerical analysis performed by UH
	Combined Std. Uncertainty	5.473653671	
HSAR	Grid resolution	-0.205532357	Numerical analysis performed by UH
	Tissue density, conductivity and permittivity	1.964833486	Numerical analysis performed by UH
	Loading position	6.21185	Numerical analysis performed by UH
	Coil input	6.862385149	Numerical analysis performed by UH
	Combined Std. Uncertainty	9.464788668	
Local max	Grid resolution	-0.75515072	Numerical analysis performed by UH
	Tissue density, conductivity and permittivity	3.216847092	Numerical analysis performed by UH
	Loading position	15.07078	Numerical analysis performed by UH
	Coil input	3.316160974	Numerical analysis performed by UH
	Combined Std. Uncertainty	15.78111819	Numerical analysis performed by UH

Take the uncertainty of prediction into account, the combined uncertainty is shown in the following table.

Table I-X. Combined Uncertainty in %.

Combined uncertainty		CP	EP1	EP2	EP3
PBSAR	head	6.75%	6.76%	6.76%	6.77%
	neck	7.60%	7.61%	7.64%	7.73%
	upper sternum	7.43%	7.42%	7.39%	7.35%
	heart	7.30%	7.29%	7.27%	7.22%
	liver	7.55%	7.53%	7.57%	7.60%
	abdomen	6.38%	6.36%	6.34%	6.33%
	pelvis	6.34%	6.35%	6.43%	6.66%
	groin	7.03%	7.08%	6.96%	6.83%
	knee	8.25%	8.13%	8.14%	7.96%
	ankle	7.17%	7.03%	7.42%	8.81%
HSAR	head	10.85%	10.88%	10.68%	10.49%
	neck	11.11%	11.10%	11.42%	11.86%
	upper sternum	12.19%	12.18%	12.37%	12.61%
	heart	47.36%	47.64%	57.29%	76.03%
	liver	20.02%	19.94%	20.24%	20.70%
	abdomen	28.24%	29.39%	26.63%	21.38%
	pelvis	19.38%	18.47%	21.49%	27.39%
	groin	23.20%	22.09%	34.40%	51.31%
	knee	101.24%	106.32%	108.44%	109.63%
	ankle	35.78%	38.01%	32.04%	27.30%
Local max	head	18.30%	17.99%	18.32%	16.67%
	neck	16.83%	16.83%	17.39%	16.25%
	upper sternum	17.14%	17.23%	16.74%	16.20%
	heart	19.44%	19.31%	19.79%	17.52%
	liver	16.51%	16.43%	16.64%	16.34%
	abdomen	15.98%	16.09%	15.96%	15.91%
	pelvis	16.30%	16.42%	16.14%	15.96%
	groin	18.12%	18.12%	18.47%	16.32%
	knee	15.92%	15.86%	16.07%	16.49%
	ankle	18.70%	18.99%	18.84%	19.79%

Appendix II. Uncertainty analysis of validation experiment

II.1. Introduction

This document provides the uncertainty assessment for validation experiment. The uncertainty process evaluation follows ISO/TS 10974 Ed. 1 Annex R. According to this document, the result of a simulation value y is a function of *N* parametersx_1,x_2, …, x_N. The combined standard uncertainty $u_c(y)$ can be derived from individual uncertainty components$u(x_i)$. The total uncertainty can be calculated from root sum square of the uncertainty of the individual components

$$u_c(y) = \sqrt{\sum_{i=1}^{m} c_i^2 \cdot u^2(x_i)}\ , \qquad \text{(II-1)}$$

in this formula c_i is the sensitivity coefficient calculated by$\partial y/\partial x_i$.$u(x_i)$is the standard deviation of each term and $u_c(y)$ is the combined uncertainty.

The uncertainty sources in our test case are listed as below:

1. Uncertainty of the phantom position
2. Uncertainty of the rod position
3. Uncertainty of the gel dielectric properties
4. Uncertainty of the grid resolution
5. Uncertainty of Electrical equipment readout

II.2. Individual uncertainty evaluation

The individual uncertainty can be evaluated in two steps:

A. the calculation of the sensitivity coefficient

B. The evaluation of the standard deviation of each individual term.

The sensitivity coefficients of the phantom position, rod position gel dielectric properties including conductivity and permittivity, and grid resolution are estimated. And the result of the target value y is the temperature rise in our situation. Therefore, we have

$$y = T\ rise, \tag{II-2}$$

we assume the T rise of the gel is a function of the phantom position, rod position gel dielectric properties including conductivity and permittivity, and grid resolution. And it is a linear equation when the variation of these parameters is small. The sensitivity coefficient can be written as $\Delta y/\Delta x_i$.

II.2.1. Loading position

To calculate the sensitivity coefficients regarding to the phantom position, the phantom position is moved ±5 mm in the x, y, z direction from the standard position (isocenter of the gel at the middle of the coil in x, z direction and the phantom are set on the bed in y direction, position of the bed is measured and provided by UIH, 420mm from the top of the coil).

The sensitivity coefficient is calculated for each direction. The relative percentage is obtained by dividing the sensitivity coefficient by the calculated temperature rise y when the phantom is at the standard position.

Table II-I. Sensitivity coefficient of phantom position.

3 T	Temperature rises variation (℃)	Distance variation (mm)	Ratio of T rise/distance variation	$\Delta y/\Delta x/y_{standard}$ sensitivity coefficient (%)
X direction	1	10	0.1	0.625
Y direction	0.7	10	0.07	0.4375
Z direction	0.2	10	0.02	0.125
Combination	--	--	--	0.773082

II.2.2. Rod position

To calculate the sensitivity coefficients regarding to the phantom position, the phantom position is moved ±5 mm in the x, y, z direction from the standard position (4.5 cm under the gel and 2 cm from the boundary of the gel, centre of z direction).

Table II-II. Sensitivity coefficient of phantom position.

3 T	Temperature rises variation (℃)	Distance variation (mm)	Ratio of T rise/distance variation	$\Delta y/\Delta x/y_{standard}$ sensitivity coefficient (%)
X direction	0.3	10	0.03	0.1875
Y direction	4.4	10	0.44	2.75
Z direction	0.2	10	0.02	0.125
Combination	--	--	--	2.759218

II.2.3. Phantom properties

To calculate the sensitivity coefficient regarding to the phantom properties (conductivity and permittivity), the value of conductivity and permittivity are set to be ±10% deviation from the original value separately. The relative percentage is obtained by dividing the sensitivity coefficient by the T rise measured when the conductivity and permittivity are the original value.

Table II-III. Sensitivity coefficient of medium conductivity and permittivity.

3 T	Temperature rises variation. (℃)	Parameter of interests	Ratio of T rise /parameter variation	$\Delta y/\Delta x/ y_{standard}$ sensitivity coefficient (%)
Conductivity	5.1	0.114	44.73684	279.6053
Permittivity	0.1	16.06	0.006227	0.038917

II.2.4. Grid resolution

To calculate the sensitivity coefficient regarding to the grid resolution, the max step of the mesh is set to be 0.5*0.5*1 mm and 0.25*0.25*0.5 mm.

Table II-IV. Sensitivity coefficient of the grid resolution.

3T	Temperature rises variation. (℃)	Grid size variation (mm)	Ratio of T rise /grid size variation	$\Delta y/\Delta x/ y_{standard}$ sensitivity coefficient (%)
Grid resolution	0.3	0.25	1.2	7.5

All the sensitivity coefficients will be combine as shown in the fowling table.

Table II-V. Sensitivity coefficients of each individual term.

Source of sensitivity coefficient	3 T (%)
Phantom position	0.773082
Rod position	2.759218
Gel conductivity	279.6053
Gel permittivity	0.038917
Grid resolution	7.5

1. Based on the measurements, the estimated standard deviation of the phantom position is 5 mm.

2. Based on the measurements, the estimated standard deviation of the rod position is 5 mm.

3. The relative permittivity of the water over the range of 0.1ºC to 99 ºC can be calculated using

$$\varepsilon = 87.740 - 0.4008t + 9.398(10^{-4})t^2 - 1.410(10^{-6})t^3, \qquad \text{(II-3)}$$

the measurement temperature usually ranges from 18 ºC to 45 ºC. The relative permittivity of the liquid gel under various temperature is estimated by the above equation.

Table II-VI. Relative permittivity of liquid gel under various temperature.

Temperature (ºC)	Permittivity	Temperature (ºC)	Permittivity	Temperature (ºC)	Permittivity	Temperature (ºC)	Permittivity
18	80.82	25	78.29	32	75.83	39	73.45
19	80.45	26	77.93	33	75.49	40	73.12
20	80.089	27	77.58	34	75.14	41	72.79
21	79.72	28	77.22	35	74.80	42	72.46
22	79.36	29	76.87	36	74.46	43	72.13
23	79.00	30	76.52	37	74.13	44	71.80
24	78.64	31	76.18	38	73.79	45	71.48

Hence the uncertainty of the permittivity is the standard deviation of 2.85.

The uncertainty of gel conductivity is assessed by mixing the gel according to document ASTM F-2182 10 times and using a conductivity meter to measure to liquid conductivity. The measured results are (0.47 0.48 0.52 0.50 0.42 0.41 0.48 0.46 0.45 0.50 S/m). The standard deviation of these observation is 0.033 S/m.

4. The uncertainty of the grid resolution is estimated to be 0.25 mm.

Table II-VII. Individual uncertainty component.

Source of uncertainty	Standard deviation
Phantom position	10mm
Rod position	10mm
Gel conductivity	0.033 S/m
Gel permittivity	2.85
Grid resolution	0.25mm

The uncertainties introduced by each source ($c_i u(x_i)$) are shown in the following table.

Table II-VIII. Uncertainty caused by each source.

Source of uncertainty	Uncertainty in %
Phantom position	7.73082
Rod position	27.59218
Gel conductivity	9.2269749
Gel permittivity	0.11091345
Grid resolution	1.875

II.3. Combined uncertainty evaluation

Table II-IX. Uncertainty of numerical modeling.

Source of Uncertainty	Uncertainty in %	Source of Numerical Value
Grid resolution	1.875	Numerical analysis performed by UH
Gel conductivity and permittivity	9.227641	Numerical analysis performed by UH
phantom position	7.73082	Numerical analysis performed by UH
Rod position	27.59218	Numerical analysis performed by UH
Combined Std. Uncertainty	30.16221	

The read out of the optical fiber also has an uncertainty.

Table II-X. Uncertainty of the readout.

Source of Uncertainty	Uncertainty in ℃	Source of Numerical Value
Readout Electronics	± 0.2	Optical Fiber probe

The combined uncertainty will be shown in the following table.

Table II-XI. Combined uncertainty.

Source of Uncertainty	Uncertainty in %
Numerical modeling	30.16221
Electrical equipment readout	2.5
Combined Std. Uncertainty	30.26564

Appendix III. Uncertainty analysis of E field generator

III.1. Introduction

This document provides the uncertainty assessment for validation experiment. The uncertainty process evaluation follows ISO/TS 10974 Ed. 1 Annex R. According to this document, the result of a simulation value y is a function of *N* parametersx_1,x_2, …, x_N. The combined standard uncertainty $u_c(y)$ can be derived from individual uncertainty components$u(x_i)$. The total uncertainty can be calculated from root sum square of the uncertainty of the individual components

$$u_c(y) = \sqrt{\sum_{i=1}^{m} c_i^2 \cdot u^2(x_i)}\ , \qquad \text{(III-1)}$$

in this formula c_i is the sensitivity coefficient calculated by$\partial y/\partial x_i$.$u(x_i)$is the standard deviation of each term and $u_c(y)$ is the combined uncertainty.

The uncertainty sources in this test can be categorized into two parts:

(1) The uncertainty from the transfer function model prediction, including the transfer function measurement.

(2) The uncertainty from the transfer function validation, including the numerical simulation and the temperature rise measurement.

The uncertainty of type B is derived from the measurement instruments' specification for the NI network analyser and temperature measurement system. To determine the uncertainty of type A, pairs of numerical simulations with only a single parameter variation have been executed. Two realistic values "V1", and "V2" are chosen for each variable. A linear dependence of the measurement values on the changing parameter is assumed. The sensitivity factors c_i for each parameter can be

determined. The standard deviation $u(x_i)$ is derived based on the measurements. The product of the sensitivity factor and the corresponding standard deviation is the uncertainty contribution of this parameter.

The uncertainty sources in our test case are listed as below:

1. Uncertainty of the loading position
2. Uncertainty of the box and gel dielectric properties
3. Uncertainty of the lead path
4. Uncertainty of the gel height
5. Uncertainty of the gel thermal properties
6. Uncertainty of the grid resolution

III.2. Individual uncertainty evaluation

The sensitivity coefficients of the gel dielectric properties, lead path, gel height, gel thermal properties, grid resolution, and box dielectric properties are estimated. And the result of the target value y is the temperature rise in our situation. Therefore, we have

$$y = T\ rise, \tag{III-2}$$

we assume the T rise of the gel is a function of the phantom position, rod position gel dielectric properties including conductivity and permittivity, and grid resolution. And it is a linear equation when the variation of these parameters is small. The sensitivity coefficient can be written as $\Delta y/\Delta x_i$.

III.2.1. Loading position

To calculate the uncertainty regarding to the loading position of the device under test (DUT), the loading position is moved ±5 mm in the x, y, z direction from the standard test position (isocenter of the gel).

The sensitivity coefficient is calculated for each direction. The relative percentage is obtained by dividing the sensitivity coefficient by the calculated temperature rise *y* when the phantom is at the standard position.

Table III-I. The uncertainty due to the shift of the pathways.

		Proposed system	
		1.5 T	3 T
Sensitivity coefficients (/mm)	X direction	0.09	0.11
	Y direction	0.39	1.36
	Z direction	0.06	0.19
	Combination	0.41	1.38
Standard deviation of pathway shift		10 mm	
Uncertainty in %		4.06	13.79

III.2.2. Box and gel properties

To calculate the uncertainty regarding to the electrical properties (conductivity and permittivity) of the box and gel, the value of conductivity and permittivity are set to be ±10% deviation from the original value separately. The relative percentage is obtained by dividing the sensitivity coefficient by the T rise measured when the conductivity and permittivity are the original value.

Table III-II. The details of uncertainty source (uncertainty type A) for simulation.

Uncertainty category	Parameters	Quantity	V1	V2	Standard deviation	1.5 T uncertainty in %	3 T uncertainty in %
Transfer function measurement	Gel conductivity	TF	0.47 S/m	0.517 S/m	0.033 S/m	1.41	0.19
	Gel permittivity	TF	80	88	2.85	0.29	0.54
Numerical simulation	Dielectric box relative permittivity	E_{incid}	2.25	3	0.75	0.61	4.71
	Gel conductivity	E_{incid}	0.47 S/m	0.517 S/m	0.033 S/m	7.56	11.38
	Gel permittivity	E_{incid}	80	88	2.85	0.85	0.33

III.2.3. Lead path

To calculate the uncertainty regarding to the lead pathway, the loading position is moved ±5 mm in the x, y, z direction from the standard position (desired pathway).

III.2.4. Gel height

To calculate the uncertainty regarding to the gel height, the height of the gel was introduced with an error of 5 mm.

III.2.5. Gel thermal properties

To calculate the uncertainty regarding to the gel thermal properties (conductivity and specific heat), the value of conductivity and specific heat are set to be 0.08W/(m ·k) and 47 J/(kg·k) deviation from the original value separately. The relative

percentage is obtained by dividing the sensitivity coefficient by the T rise measured when the conductivity and permittivity are the original value.

III.2.6. Grid resolution

To calculate the uncertainty regarding to the grid resolution was introduced with an error of 2 mm.

III.3. Combined uncertainty evaluation

The combined uncertainty using equation III-1 will be shown in the following table.

Table III-III. The details of uncertainty source (uncertainty type A) for experiment.

Uncertainty category	Parameters	Quantity	V1	V2	Standard deviation	1.5 T uncertainty in %	3 T uncertainty in %
Numerical simulation	Grid resolution	E_{incid}	2 mm	4 mm	2 mm	2.08	0.80
T rises measurement	Gel thermal conductivity	T	0.42 W/(m·k)	0.5 W/(m·k)	0.02 W/(m·k)	2.73	2.73
	Gel specific heat	T	4159 J/(kg·k)	4206 J/(kg·k)	160 J/(kg·k)	1.36	1.36
	Leads path	E_{incid}	0 mm	10 mm	10 mm	4.06	13.79
	Gel height	E_{incid}	9 cm	9.5 cm	0.2 cm	1.58	2.18

Table III-IV. Uncertainty specification.

1.5 T	Source of uncertainty	Uncertainty in %
Uncertainty for TF [a] model prediction	TF measurement	1.85
Uncertainty for TF model validation test	Temperature rise measurement	9.61± 1.0℃
	Numerical simulation	2.17
Combined Uncertainty	10.02± 1.0℃	
3 T	**Source of uncertainty**	**Uncertainty in %**
Uncertainty for TF model prediction	TF measurement	1.29
Uncertainty for TF model validation test	Temperature rise measurement	18.27± 1.0℃
	Numerical simulation	4.78
Combined uncertainty	18.92± 1.0℃	